Electric Stimulation Parameters for an Epi-Retinal Prosthesis

by

Andrew Eli Grumet

Submitted to the Department of Electrical Engineering and Computer Science
in partial fulfillment of the requirements for the degree of

Doctor of Philosophy

at the

MASSACHUSETTS INSTITUTE OF TECHNOLOGY

September 1999

Author .....
Department of Electrical Engineering and Computer Science
August 26, 1999

Certified by 8/26/99
John L. Wyatt, Jr.
Professor of Electrical Engineering
Thesis Supervisor

Accepted by .....
Arthur C. Smith
Chairman, Department Committee on Graduate Students

Electric Stimulation Parameters for an Epi-Retinal Prosthesis

by

Andrew Eli Grumet

Submitted to the Department of Electrical Engineering and Computer Science
on August 26, 1999, in partial fulfillment of the
requirements for the degree of
Doctor of Philosophy

Abstract

This work was undertaken to contribute to the development of an epi-retinal prosthesis which may someday restore vision to patients blinded by outer retinal degenerations like retinitis pigmentosa. By stimulating surviving cells in tens or hundreds of distinct regions across the retinal surface, the prosthesis might convey the visual scene in the same way that images are represented on a computer screen. The anatomical and functional arrangement of retinal neurons, however, poses a potential obstacle to the success of this approach. Stimulation of ganglion cell axons—which lie in the optic nerve fiber layer between stimulating electrodes and their intended targets, and which originate from a relatively diffuse peripheral region—would probably convey the perception of a peripheral blur, detracting from the usefulness of the imagery.

Inspired by related findings in brain and peripheral nerve stimulation, experiments were performed in the isolated rabbit retina to determine if excitation thresholds for ganglion cell axons could be raised by orienting the stimulating electric field perpendicularly to the axons' path. Using a custom-designed apparatus, axon (and possibly dendrite) thresholds were measured for stimulation through a micro-fabricated array of disk electrodes each having a diameter of ten microns. The electrodes were driven singly versus a distant return (monopolar stimulation) and in pairs (bipolar stimulation) oriented along fibers (longitudinal orientation) or across fibers (transverse orientation). Transverse thresholds were measured for a range of fiber displacements between the two poles of the bipolar electrode pair, and compared in each case with the monopolar threshold for the closer pole. Transverse/monopolar threshold ratios were near unity when one of the poles was directly over the fiber, but rose rapidly with improved centering of the bipolar pair. Longitudinal/monopolar threshold ratios were near unity over the same range of displacements.

As in previous work by others, thresholds were highest for perpendicular stimulating fields. Practical application of this result will require electrode designs which minimize longitudinal fringing fields.

Thesis Supervisor: John L. Wyatt, Jr.
Title: Professor of Electrical Engineering

Acknowledgments

I arrived at MIT in the summer of 1992 with decided interests in analog circuit design and neuroscience, but no funding. To get the ball rolling, I showed up early, sublet an apartment in Inman Square and started making phone calls. It wasn't long after my arrival that I walked into John Wyatt's office. He was easily the friendliest person I had met at MIT up to that point, and his retinal implant research sounded interesting. Within forty-eight hours of our first meeting, I had an office, a desk, a computer account, and a summer research project with no strings attached. What a welcome!

Ultimately the summer job evolved into a doctoral dissertation. Along the way John has been an advisor, a teacher, a colleague, and a friend. His thoughtfulness and optimism have been a continual inspiration, often keeping me going when progress was slow. Of course, it's hard to work closely with someone for seven years and agree on *everything*. But we've always managed to find a mutually acceptable way out when disagreements arose. I truly could not have hoped for a better graduate school experience. First off, then, I want to thank John for giving me absolutely nothing to complain about.

Dr. Joe Rizzo, a co-director with John of the larger project encompassing my work, has been a valued mentor and friend, and read an early version of this document.

Tom Weiss advised me against doing an experimental thesis from scratch, but—to my great benefit—still participated on my thesis committee even when I didn't take his advice. In addition, his clear and incisive presentations of technical material have served as a model which I have endeavored for many years to emulate in my own work.

Don Eddington, in addition to participating on my thesis committee, provided support and guidance at pivotal points along the way.

Dennis Freeman supported my work in many ways, most notably by letting me use all of the neat equipment in "the chemistry room".

Without the help of Markus Meister and Richard Masland, I would never have gotten the experimental setup working as quickly as I did. David Warland and Iman Brivanlou at the Meister lab were especially helpful.

Malini Narayanan, Sumiko Miller Goldbaum, Alan Gale, Tim Denison, Shawn Kelly, Brad Lichtenstein, and Erich Caulfield all worked in the same lab with me at various times, and as a result shared (whether they were in a loquacious mood or not) in many a good laugh and deep discussion.

Mohamed Shahin provided invaluable assistance with the experiments.

The Whitaker Foundation generously picked up the tab for roughly half of my tuition and stipend, and also provided some greatly appreciated discretionary funds for textbooks and travel.

Finally, I'd like to acknowledge my family and my wonderful wife, Lara Asmundson, for their moral support through high and low.

Contents

List of Figures

List of Tables

Chapter 1

Introduction

1.1 Background and motivation

1.1.1 Neural and retinal prostheses

The human body is composed of cells. Our sensory and motor capabilities arise from the properties of various types of nerve and muscle cells, from the complex networks which they form, and from additional supporting cells which maintain a suitable operating environment. Disruption of these cells and networks, caused by disease or injury, can result in paralysis or sensory loss.

Neural prostheses can sometimes compensate for lost function, usually by electrically stimulating viable neurons in pathways where natural connections have been disrupted. Among the most successful examples to date is the cochlear prosthesis, which provides auditory sensation to otherwise profoundly deaf patients. Deafness often results from loss of the hair cells of the inner ear, which transform the mechanical energy of sound into neural signals that can be transmitted to the brain. Cochlear prostheses electrically stimulate surviving neurons which are post-synaptic to the hair cells, effectively bypassing the initial parts of the natural auditory pathway. Prolonged use of cochlear implants can lead to dramatic improvements in both speech perception and speech production, and at present there are at least four different types of commercially available devices (Loizou, 1999).

The visual prosthesis field is less mature. While work on cortically based artificial vision dates back to the 1960's (Hambrecht, 1990), researchers have yet to produce a device ready for routine clinical use. The last decade has seen increasing interest in the development of a retina-based visual prosthesis (Chow and Chow, 1997; Eckmiller, 1997; Humayun et al., 1999; Rizzo and Wyatt, 1997; Zrenner et al., 1999). Unlike cortical prostheses, the success of this approach depends on the survival of at least a subpopulation of retinal neurons. Of critical importance is the survival of the retina's output neurons, the ganglion cells. The degenerative disease retinitis pigmentosa, which affects over a million worldwide (Berson, 1993), fits these criteria. Significant

populations of ganglion and bipolar cells are spared by this disease despite severe photoreceptor loss (Santos et al., 1997; Stone et al., 1992). The primary advantages of a retina-based prosthesis are the surgical accessibility of the ganglion cells and the topographic ordering of their receptive fields. Further consideration of the relative merits of the retinal and cortical approaches is provided elsewhere (Normann et al., 1999; Rizzo and Wyatt, 1997).

This work was undertaken to contribute to the development of a retinal prosthesis which may someday provide useful artificial vision to patients blinded by diseases like retinitis pigmentosa. The prosthesis will function by electrically stimulating healthy inner retinal neurons through a micro-electrode array residing on the retina's exposed surface. The design of such a prosthesis entails many lines of inquiry, including selection of electric stimulation parameters, selection of biocompatible device materials, development of surgical methods for implantation and fixation of the device, electronic design of intra- and extra-ocular components, and design of schemes for transmission of power and signal to the intra-ocular electronics. This thesis is concerned with selection of electric stimulation parameters for the prosthesis.

1.1.2 Electric stimulation parameters

There are a number of free parameters to consider when designing an electric stimulation method, including the shape and size of the stimulating electrodes, the arrangement of the stimulating electrodes on the retina, the wave shape and duration of the stimulation current, and the amplitude of the stimulation current. The plausible parameter space is substantial. While retinal stimulation studies have often used one of a relatively few conventional electrode shapes (e.g. flat circular, flat annular, ball end, sharp point), characteristic dimensions can range from microns to hundreds of microns. In addition, modern micro-fabrication techniques make it possible to pattern flat stimulating electrodes in any desired shape and configuration with micron resolution. Furthermore, a broad range of current waveforms, durations, and amplitudes has been successfully used to stimulate the retina. Current waveforms might range from microseconds to milliseconds in duration and from hundreds of nanoamperes to milliamperes in amplitude.

Coupling between different stimulation variables reduces the useful parameter space to some degree. Over a range of durations, for example, the minimum amplitude capable of eliciting neuronal and perceptual responses will decrease with increasing stimulus duration (i.e. classic strength-duration behavior). On the other hand, the minimum effective amplitude for a particular duration may vary with the shape of the stimulating electrode. Hence many combinations of stimulation parameters will fail to produce retinal responses and, once identified, can be ruled out for use in a prosthesis.

Any candidate set of stimulation parameters must be further judged for its ability to evoke detailed visual sensations, its potential to cause further harm to the retina,

and its total power consumption. The task of the retinal prosthesis designer is to locate optimal regions of the parameter space which maximize performance on the first of these criteria and minimize the latter two.

1.1.3 Objective

The present work aims to elucidate the relationship between the stimulating electrode geometry and the pattern of evoked neuronal responses. The specific objective is motivated by considerations of the interface between the prosthesis and retina, and the types of percepts which might be achievable through such an interface.

The topographic arrangement of receptive fields across the retinal surface lends itself to a simple model of visual perception. Light arriving from a restricted area within the visual scene will activate neurons in a corresponding restricted area on the retinal surface. Conversely, electric stimulation of a small area of retina is expected to result in a focal visual percept. Electrically evoked visual perceptions, or phosphenes, have in fact been demonstrated in numerous experiments (see Section 1.2) with various stimulation methods and degrees of focality. Today's retinal prosthesis designs would employ electrode arrays to gain access to a large number of individually addressable phosphene elements, conveying the visual scene much in the same way that images are represented on a computer screen.

A major concern is that axons in the nerve fiber layer, lying between an epiretinal microelectrode and the target neurons (see Figure 1.1), will be stimulated. Stimulation of axons emanating from ganglion cells far removed from the point of stimulation would probably convey the perception of a peripheral blur, detracting from the usefulness of the imagery. Hence it would be desirable to bypass the axons while selectively stimulating other parts of the ganglion cells and/or other types of surviving cells such as bipolar cells.

Some advantage may be gained from the finding in brain and peripheral nerve experiments that axon thresholds were highest when the stimulating field was oriented perpendicular to the axon's path (Ranck, 1975; Rushton, 1927). This finding is also predicted by theoretical models (Grumet, 1994; Plonsey and Altman, 1988). Thus, a stimulating electrode geometry which limits field components along axon paths might permit selective stimulation of more distant retinal elements. The objective of the present work is to explore this possibility experimentally using an *in vitro* retina preparation.

1.2 Related work

There is a substantial and diverse literature devoted to electric stimulation of the retina. The most recent research was directed, as is this thesis, at retinal prosthesis development. Prior to the 1990's, researchers used electric stimulation either to study

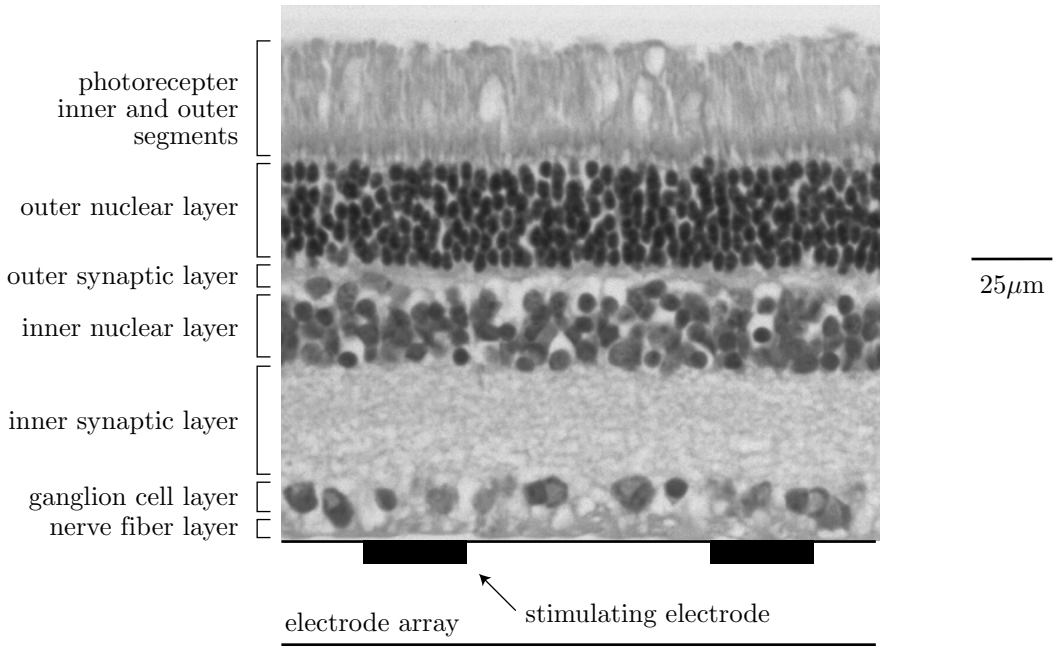

Figure 1.1: Cross-section of rabbit retina with epi-retinal stimulating electrodes illustrated schematically. The section was taken from central retina, a few millimeters below the optic disk. This is the same region that was used for the experiments of Chapters 2 and 3. The retina was stained (with hematoxylin and eosin) and imaged under the direction of Dr. Charles Dangler, D.V.M., Ph.D of MIT's Division of Comparative Medicine.

retinal processing using a novel type of input or to elucidate the excitation mechanisms involved.

Of critical interest when considering this body of work are 1) a comparison of excitation thresholds for ganglion cell axons with thresholds for other retinal elements, and 2) an examination of how the thresholds for axons and other elements depended on the choice of stimulation parameters. This section will concentrate on the threshold comparisons; consideration will be given to absolute thresholds in Chapter 3.

1.2.1 Direct threshold comparisons

Jensen and colleagues (Jensen et al., 1996; Rizzo et al., 1997) and Greenberg (1999) systematically compared excitation thresholds for ganglion cell axons and somata. Using two different stimulating electrode types, monopolar and concentric bipolar, Jensen measured thresholds for producing single spikes in rabbit retinal ganglion cells. Spikes were recorded from each cell's axon at a location near the optic disk. Stimuli were applied in the vicinity of ganglion cell somata and at locations between the somata and recording electrode, along the axon paths. For both stimulating electrode types, median axon thresholds were approximately twice a large as median cell body thresholds. It was also true, however, that cell body and axon thresholds exhibited broad ranges and overlapped substantially.

In contrast with Jensen's experimental work, Greenberg used a computational model to simulate extracellular stimulation of a retinal ganglion cell with a monopolar electrode (Greenberg et al., 1999). In general agreement with Jensen's median threshold data, Greenberg found that thresholds were 20% to 73% higher for axons than for cell bodies.

The stimulation parameters in Jensen's experiments and Greenberg's simulations were similar. In both studies, 100μs cathodal stimulation pulses were applied through radially symmetric monopolar electrodes which were placed against the epi-retinal surface. In Jensen's experiments, the electrode had a cone-shaped tip with 5μm of exposed length, and the return was an Ag/AgCl sheet placed beneath the sclera. In Greenberg's simulations, the electrode was either a point source, a 50μm diameter disk, or a 100μm-diameter disk, with the return at infinity. Jensen also used a concentric bipolar stimulating electrode in some experiments. This electrode had a 25μm diameter, hemispherical tip and a recessed, annular return with an inner diameter of 200μm.

1.2.2 Indirect threshold comparisons

In 1977, Dawson and Radtke observed rather usefully that "one would expect most retinal cells to respond at some current level" (Dawson and Radtke, 1977). Hence electrically generated responses might initiate in one type or in many types of retinal neurons, depending on the current level. At current levels which are just sufficient

to produce a retinal output, however, only the element(s) with the lowest excitation thresholds will be directly stimulated. Let's call such elements *maximally sensitive*.

The set of maximally sensitive elements might be a function of the parameters used for stimulation. Also, it might comprise one or more cell types. As illustrated below, studies which identify these maximally sensitive elements permit indirect, semi-quantitative comparisons of thresholds for different retinal elements.

In Jensen's experiments (described above), ganglion cells and their axons were always stimulated directly, as verified from the short and stable response latencies and from the persistence of the responses in the presence of the synaptic blocker cadmium (Jensen, unpublished data). Because no trans-synaptic responses were observed, thresholds for other retinal elements such as bipolar cells and photoreceptors must have been comparatively high. A similar inference cannot be drawn from Greenberg's simulations (also described above), since only ganglion cells were included in the model.

Jensen (1996) also created maps of ganglion cells' electrical receptive fields, as did Greenberg in an experimental study of frog retina (Greenberg, 1998c). The maps were produced by measuring spike thresholds for a large number of stimulating electrode positions in the vicinity of the cell body. In general thresholds increased with distance from a concentrated region of low thresholds, but sometimes there were elongated low-threshold regions extending toward the optic disk. Stimuli were presumably acting on axons in these cases, indicating that axon thresholds were comparatively low.

The stimulation parameters used by Jensen were described in the previous Section. Greenberg (1998c) delivered 0.52ms stimuli to the frog epi-retinal surface through an array of 400μm diameter disk electrodes in a variety of monopolar and bipolar configurations. For monopolar stimulation, the return electrode was either placed on the same side of the retina as the stimulating array, several millimeters distant, or else on the opposite (extra-ocular) side of the sclera, directly beneath the stimulating array. Pairs of electrodes with 113μm edge-to-edge separation, oriented either in parallel with or perpendicular to the presumed axon path, were used for bipolar stimulation (see Section 1.2.5 for further discussion of these bipolar measurements).

In a number of other accounts, the lowest amplitude stimuli elicited responses whose properties were inconsistent with axon stimulation. Phosphenes elicited in alert human subjects, for example, were localized and corresponded well with electrode positions (Brindley, 1955; Humayun et al., 1996; Humayun et al., 1999). Another phosphene study demonstrated non-linear strength duration curves consistent with an hypothesized interaction of distinct ON and OFF processes (Howarth, 1954). These processes presumably arose within the retinal network. Two additional studies described complex responses which lasted up to two orders of magnitude longer than the originating stimuli (Crapper and Noell, 1963; Doty and Grimm, 1962). Such responses, like Howarth's, probably arose within the retinal network. Finally, a study of *in vitro* frog retina reported on a number of properties of threshold response latencies for ganglion cell spikes (Greenberg, 1998a). Latencies were high (9.8-12.2ms) in nor-

mal retinal and low (3.7ms) in the presence of the synaptic blocker cadmium. More interestingly, the latencies in normal retina fell with increasing current level until a discontinuous jump in latency occurred from 6-7ms to 3-4ms. The lower-threshold, higher-latency responses were consistent with stimulation of elements pre-synaptic to ganglion cells, whereas the higher-threshold, lower-latency responses arose in ganglion cells or their axons. Two of the other studies mentioned above (Crapper and Noell, 1963; Doty and Grimm, 1962) also described a similar duality of response types. Though not maximally sensitive in these studies, axons may have been stimulated at thresholds which were only slightly higher than the thresholds for other elements.

Stimulation parameters for these seven studies are summarized in Table 1.1.

1.2.3 The pulse duration hypothesis

Greenberg (1998b) argued that ganglion cell stimulation—at the axon or otherwise—can be avoided completely by using sufficiently long (>.5ms) stimulation pulses. Primary support for this claim came from a series of strength-duration curves for ganglion cell spikes in the frog retina. To isolate direct ganglion cell stimulation from stimulation of deeper cells, Greenberg measured some of the strength-duration curves in the presence of the synaptic blocker cadmium. The stimulating electrode type and placement, which were identical to those used in another study (Greenberg, 1998a), are listed in Table 1.1.

Addition of cadmium to the bathing medium raised the rheobase and lowered the chronaxie relative to normal retina. In addition, the strength duration curves for normal retina, which were measured under both light and in the dark conditions, intersected the cadmium curve such that thresholds under cadmium were relatively high for long stimulation pulses and relatively low for short pulses. Hence ganglion cells would be expected to be maximally sensitive at short pulse durations whereas other retinal elements would be maximally sensitive at longer pulse durations. Support for this hypothesis came from a phosphene experiment in which a 0.7mm disk was placed against a blind patient's retina and the pulse duration varied. Phosphenes were relatively focal for 1-8ms durations but became elongated when the pulse duration was lowered to 0.5ms.

Two alternative numerical substitutes for the boundary between "short" and "long" can be determined from the durations at which strength-duration curves for normal and cadmium conditions intersected. These were roughly 0.1ms for dark-adapted retina and 3ms for light-adapted retina. The 0.5ms boundary suggested by Greenberg falls between these intersection points, and comes apparently from the phosphene experiment. With one exception (Brindley, 1955), the studies in Table 1.1 are consistent the Greenberg's hypothesis since stimuli were 0.5ms or greater and axon thresholds were comparatively high.

Study	Response type (species)	Stimulus phase duration	Electrode type	Electrode placement
Brindley (1955)	Phosphenes (human)	a few μs – DC	Various monopolar and bipolar, several mm long	Against the conjunctiva; monopolar return in mouth
Crapper & Noell (1963)	GC spikes (rabbit)	0.5ms	Monopolar	Vitreous; return under the skin overlying the sacrum
Doty & Grimm (1962)	Cortical potentials (cat)	1ms	Bipolar, 1mm separation	Epi-retinal surface; various orientations relative to axons
Greenberg (1998a)	GC spikes (frog)	0.52ms	Monopolar, 1.5mm diameter	Scleral surface; return several mm distant on epi-retinal side
Howarth (1954)	Phosphenes (human)	7–100ms	Monopolar	Forehead; return in hand
Humayun (1996)	Phosphenes (human)	1–4ms	Various monopolar & bipolar, 50-200μm diameter	500μm above epi-retinal surface; monopolar return at a distant location
Humayun (1999)	Phosphenes (human)	$\leq$2ms	Arrays: 400μm disks; monopolar & bipolar	Epi-retinal surface; monopolar return on shoulder
			Wire electrodes: 25–125μm disks; monopolar & bipolar	500μm above epi-retinal surface; monopolar return on shoulder

Table 1.1: Summary of stimulation parameters for seven studies in which axons were not maximally sensitive. Excitation thresholds for a number of studies—one appearing in this table and several mentioned in the text—are listed in Table 3.4. *Abbreviations:* GC = ganglion cell.

1.2.4 Other studies

A number studies not described above are equivocal for the purpose of comparing thresholds for axons and other retinal elements. Several researchers, for example, recorded exclusively from retinal neurons which preceded ganglion cells in the visual pathway and would not have observed responses arising in axons, had they occurred (Miyachi et al., 1984; Murakami et al., 1982; Toyoda and Fujimoto, 1984; Trifonov and Byzov, 1977). Ogden and Brown, on the other hand, recorded antidromic ganglion cell spikes and several other types of responses at various retinal depths, but did not determine the thresholds for these (Ogden and Brown, 1964). In still other studies, recordings were made from or subsequent to ganglion cells, and stimulation thresholds determined as well, but initial excitation sites were not identified (Dawson and Radtke, 1977; Humayun et al., 1994). Finally, a number of researchers demonstrated complex responses *in vitro* which, like Howarth's, probably arose in the retinal network, but did not (or had no reason to) convincingly rule out the possibility that axons were stimulated directly as well (Gernandt and Granit, 1947; Granit, 1946; Granit, 1948; Knighton, 1975; Molotchnikoff, 1976; Molotchnikoff and Lachapelle, 1978; Potts and Inoue, 1970).

1.2.5 Discussion

In numerous experiments and in one computational study, excitation thresholds were generally higher for axons than for other retinal elements. However, in most of these studies the stimulating electrodes were not placed against the epi-retinal surface, as they would be in an eventual implant. As discussed further in Section 4.2, this realistic configuration is also particularly well-suited for axon stimulation. Where stimuli were applied to the epi-retinal surface and direct threshold comparisons for axons and other elements (specifically, ganglion cell bodies) were made, thresholds for the two groups showed broad overlap, with median thresholds for the former no more than twice as large as median thresholds for the latter.

The margin of axon thresholds above other elements' thresholds might be substantially raised using electrode designs which produce stimulating fields running perpendicularly to axons. This hypothesis has not been systematically tested in retina, though a few measurements suggestive of it were made by Greenberg (1998c) using bipolar electrodes at the epi-retinal surface in frogs. Consistent with the hypothesis, axon stimulation was never observed when the bipolar electrode pair was oriented perpendicular to the presumed axon path (N=2 cells). Furthermore, axon stimulation did occur in one of the two cases where the bipolar pair was oriented in parallel with the presumed axon path. However, the axon locations relative to the stimulating electrodes—which was found in the present work to strongly influence the dependence of axon thresholds on the orientation of the bipolar pair—were neither known nor estimated.

1.3 What's In This Thesis

In pursuit of the goal described above, I constructed a new experimental apparatus and conducted experiments on isolated rabbit retinas. The setup employed microfabricated electrode arrays, which allowed rapid switching between different electrode configurations without mechanical disruption of the tissue, and provided tremendous flexibility in patterning electrode shapes and arrangements. Axon (and possibly dendrite) excitation thresholds were measured using 10μm diameter disk stimulating electrodes, both singly versus a distant return (monopolar stimulation) and in pairs (bipolar stimulation). Bipolar electrode pairs were oriented across the fibers under study (transverse orientation) and along the fibers (longitudinal orientation). Thresholds for transverse bipolar stimulation were compared with those for monopolar and longitudinal bipolar stimulation at the same distance from the fiber. Transverse thresholds were greater than monopolar or longitudinal thresholds, provided that the target fiber was near the midpoint between the two electrodes used for transverse bipolar stimulation. The ratio of transverse to longitudinal thresholds was close to unity if one of the electrodes forming the bipolar pair was directly over the fiber, and rose rapidly as the fiber approached the midpoint. The largest measured ratio was about 3.5. These results are consistent with theory and previous experiments, since thresholds were highest when the stimulating field was most nearly perpendicular to fibers, but show that bipolar electrode pairs formed from 10μm diameter disks would not be optimal for use in a retinal prosthesis.

The remainder of the thesis is structured as follows:

Chapter 2 describes the method developed to stimulate and record from patches of isolated retina using a planar microelectrode array.

Chapter 3 describes measurements of thresholds for generating single spikes in fibers using monopolar and bipolar stimulating electrodes.

Chapter 4 considers the strengths and weaknesses of the new experimental methods, and comments on the implications of the thesis results for the design of an epiretinal prosthesis.

Chapter 5 puts forth some thoughts for future work.

Appendix A presents data from one set of measurements where thresholds were determined for an *in vitro* human retina.

Appendix B provides detail on the design of custom electronic instruments used in the experimental setup.

Appendix C summarizes efforts to reduce stimulus artifacts.

Chapter 2

Multi-Electrode Stimulation and Recording In the Isolated Retina

2.1 Introduction

This chapter describes the methods used to stimulate and record from neurons in isolated retinas using a planar, photo-lithographically patterned multi-electrode array. The methods are adapted primarily from two sources: Ames' *in vitro* rabbit retina preparation (Ames III and Nesbett, 1981), and the techniques of Meister, Pine, and Baylor for multi-electrode ganglion cell recording (Meister et al., 1994). These methods were used to conduct studies of ganglion cell axon (and possibly dendrite) excitation thresholds as a function of monopolar electrode position and bipolar electrode orientation, the results of which are described in Chapter 3.

The experimental methods were developed specifically for this thesis, in an effort to improve upon techniques used by a colleague, Ralph Jensen, for similar work (Jensen et al., 1996; Rizzo et al., 1997). Jensen measured thresholds for eliciting single ganglion cell spikes with a sharp-ended stimulating electrode placed at various points on and above the retinal surface, to provide a quantitative description of the spatial extent of electric stimulation. This technique offered a fairly limited choice of stimulating electrode geometries, typically a central point or disk, optionally surrounded by a concentric ring. Furthermore, it was necessary to raise and re-lower the stimulating electrode when changing the position of on-surface threshold measurements to reduce the likelihood of dragging the retina. Dragging was undesirable because it could introduce electrode placement imprecision or "loss" of a neuron which had been inadvertently moved away from the recording electrode. The possibility of dragging could not be completely eliminated, however, since the stimulating electrode had to be moved between threshold measurements.

Mechanical disruption of the retina may be avoided by using a multi-electrode array instead of a single electrode (Greenberg, 1998c; Kuras and Gutmanienė, 1997). Stimulus positions and geometries are controlled by the choice of stimulator con-

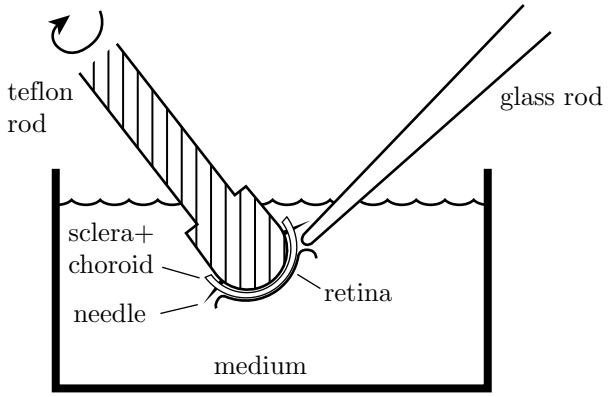

Figure 2.1: Method for isolating retina from the pigment epithelium.

nections to the array, allowing for rapid switching among a large number of configurations. Photolithographic techniques, which have been used in electrophysiology research since the 1970's (Pickard, 1979), make it possible to pattern these arrays with essentially arbitrary electrode geometries and distributions.

2.2 *In vitro* preparation

Retinas were prepared for study as follows. Female Dutch Belted rabbits, weighing 2-2.5kg, were sedated by intramuscular injection of ketamine (35mg/kg) and xylazine (5mg/kg). The rabbits were then sacrificed by an intravenous overdose of sodium pentobarbitol. Immediately following death, one of the eyes was removed and a small cut made near its equator using a sharp blade. The cut was advanced completely around the eyeball using miniature surgical scissors. The front portion of the eye and the vitreous were then gently pulled away with forceps as Ames' medium (Sigma Chemical Co., St. Louis, MO, USA) was poured into the eyecup. The Ames' medium was buffered with sodium bicarbonate (per manufacturer's instructions) and equilibrated with a gas mixture of 95% oxygen and 5% carbon dioxide, bringing the solution pH to 7.3-7.4. The interval between death and introduction of medium was five to seven minutes.

To facilitate separation of the retina from the pigment epithelium, the eyecup was turned inside-out and mounted under medium on a rounded Teflon rod as illustrated in Figure 2.1. A plane of cleavage was developed between the retina and pigment epithelium using a round-tipped glass rod, and the retina progressively separated from the pigment epithelium by advancing the cleavage plane toward the optic disk while rotating the Teflon rod about its central axis. When only the attachment at the optic disk remained, the sclera and choroid were cut from around the disk leaving

just the retina and small segment of optic nerve.

The retina was transferred to a shallow dish filled with medium, using the nerve stump as a handle. The stump was then cut away so that the retina could be laid flat against the bottom of the dish and a small trapezoid-shaped patch cut from the central portion, a few millimeters below the optic disk.

The patch and a small volume of medium were transferred to a fluid-tight chamber created by sealing a plastic frame to an electrode array which formed the floor. The patch was positioned at the center of the array with the ganglion cells facing the exposed electrodes, and oriented so that the cluster of stimulating electrodes was between the optic disk and the cluster of recording electrodes (see Figure 2.2). The optic disk was not actually contained within the patch area—rather, it's location in an intact retina could be deduced from the shape of the patch. Medium was then removed from the chamber to the fix the retina in place, and a castle-shaped brace lowered onto the retina to hold it against the array. The assembly consisting of brace, retina, frame, and array is illustrated in Figure 2.3a. The center of the brace was hollow and covered with dialysis membrane (Spectrum, Laguna Hills, CA, USA) so as to provide light force on the retina while allowing for exchange of Ames' medium. Spacers (approximately 100μm thick) were glued to the bottom of the brace to prevent excessive force on the retina. A detailed view of the brace is shown in Figure 2.3b. The chamber was immediately refilled with fluid once the brace was in place.

Medium was brought to one side of the chamber from a drip-bottle hanging above the preparation. A valve limited the inflow rate to approximately one milliliter per minute. Fluid was removed from the opposite end of the chamber by a peristaltic pump. The array rested on a metallic base which was warmed to 32-34 degrees Celsius using DC ohmic heaters. This slightly cool temperature was used because at higher temperatures the retina left behind sticky residues which reduced the lifetime of the arrays. Though some measurements were made at 37-38 degrees Celsius, these were too few in number to support any general statements about the possible effects of temperature on thresholds.

All manipulations and measurements were carried out in dim white light. Physiologic responses were studied under these conditions for a period of four to nine hours.

2.3 Electrode array design

The electrode arrays were formed by patterning a series of conducting and insulating layers on a rigid glass substrate measuring 0.8mm $\times$ 24.4mm $\times$ 40.9mm. Each electrode was a 10μm-diameter disk, and each could be used for either stimulation or recording. In most cases, half of the electrodes were used for stimulation and the other half for recording.

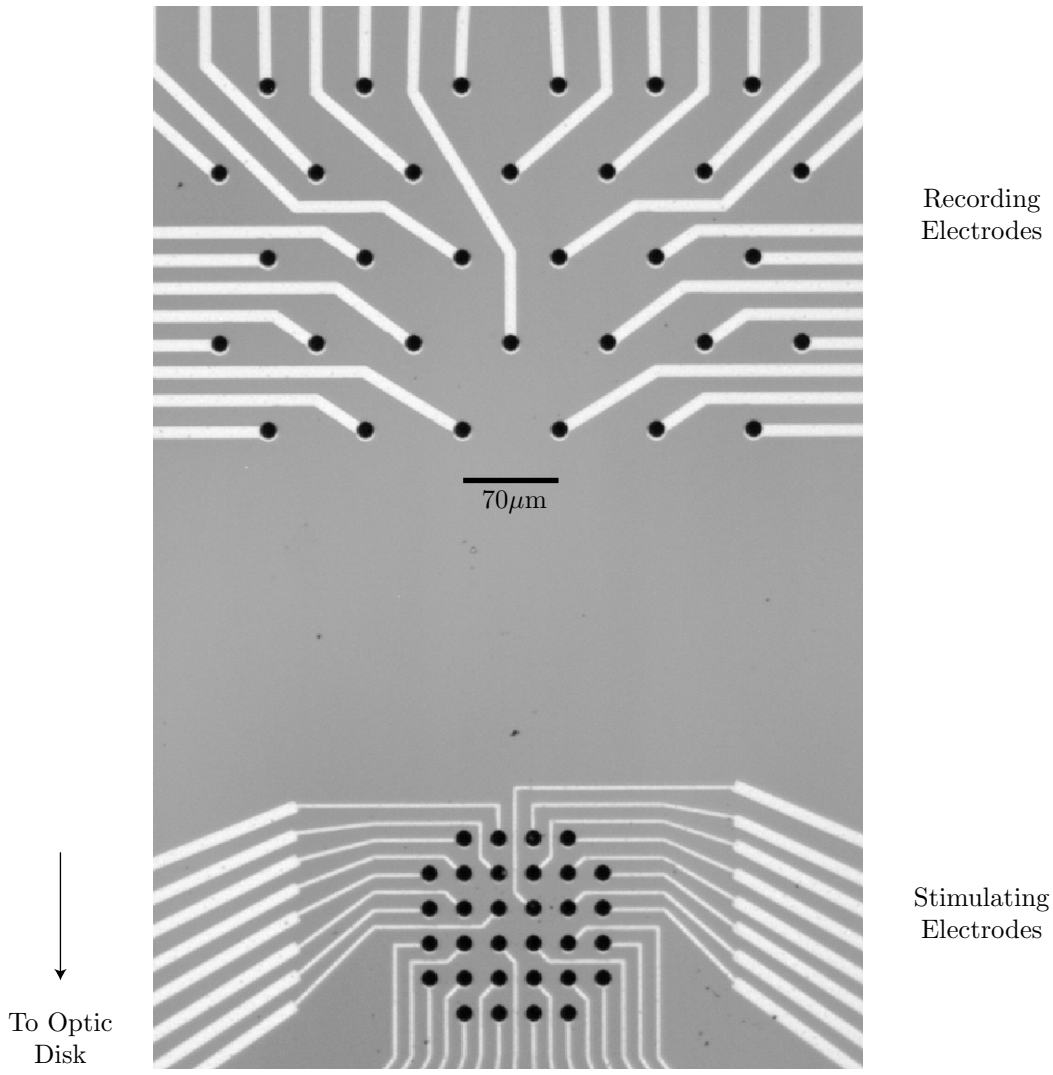

Figure 2.2: Head on view of the electrode array. During an experiment the retina patch was oriented so that in an intact retina the optic disk would be located below the stimulating electrodes.

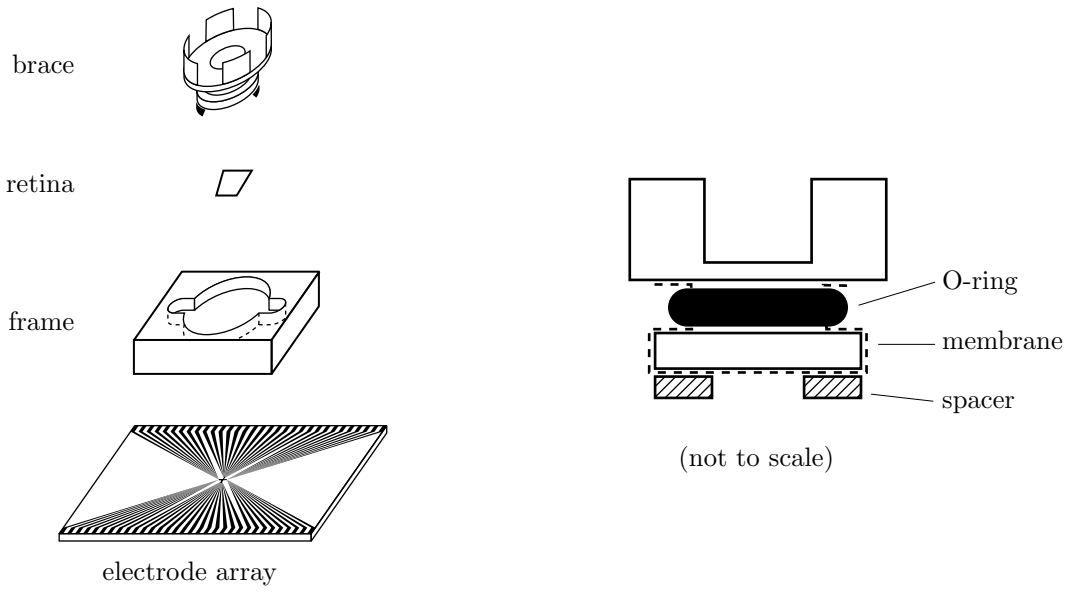

Figure 2.3: (a) Array assembly. During experiments the array, frame, retina and castle-shaped brace were vertically compacted. The frame was sealed to the array with RTV118 silicone (GE Silicones, Waterford, NY, USA) to provide a fluid-tight seal. The leaves at the top of the brace pressed tightly against the walls of the frame so that the bathing medium would not buoy it up off of the retina. (b) Detailed view of the brace.

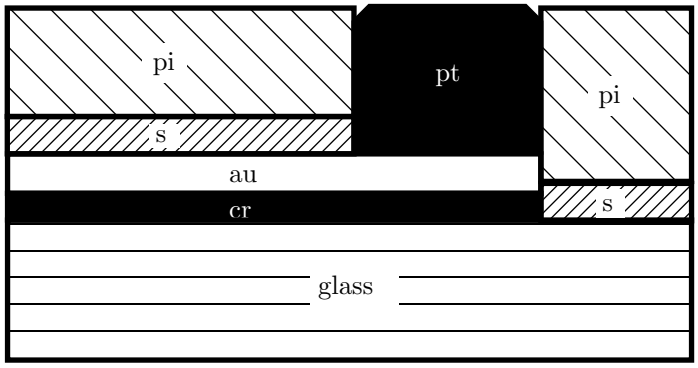

Figure 2.4: Cross-section view of the electrode array (not to scale). Abbreviations and layer thicknesses: cr=chrome, 650Å; au=gold, 5000Å; s=silicon nitride, 2000Å; pi=polyimide, 10μm; pt=platinum black, approximately 10μm.

2.3.1 Cross-section

A cross-section view of the electrode array is shown in Figure 2.4. The thin chrome layer acted as a glue between the gold and glass, which do not adhere well to one another. A combination of silicon nitride and polyimide were used as insulation. The silicon nitride provided an effective barrier to resistive current flow, while the thick polyimide layer reduced capacitance between the gold wires and solution. To reduce electrode impedances to approximately 100kΩ magnitude at 1kHz, the gold surfaces were coated with platinum black (Kovacs, 1994; Regehr et al., 1989). This was accomplished by immersing the electrodes in a dilute solution of chloroplatinic acid and lead acetate (YSI Inc., Yellow Springs, OH, USA) and driving -0.3μA through each 10μm-diameter electrode, using a platinum wire for the return, for approximately ten seconds. The same treatment was re-applied as needed if, for example, electrodes had a low signal-to-noise ratio when used for recording.

2.3.2 Electrode layout

The electrode array pattern used in this thesis is shown in Figure 2.2.The dark spots in the Figure are 10μm-diameter areas where the gold conductors were exposed and coated with platinum black. The polyimide and silicon nitride insulation layers, which are not visible in the image, cover the entire area except for the platinized electrodes.

The electrodes on the array were grouped into two clusters, one typically used for recording and the other for stimulation. The clusters were spaced several hundred microns apart to reduce stimulus artifacts, as discussed in Section 2.4.5. The electrodes in the recording cluster were arranged hexagonally on 70μm centers, as in other stud-

ies where similar recordings were made (Meister et al., 1994). The electrodes in the stimulating cluster were spaced more closely together, with 25μm center-to-center spacing, to allow for good resolution (i.e. on the order of the electrode diameter) when sampling thresholds versus position.

2.3.3 Electrical connections to instruments

The lighter lines in Figure 2.2 are chrome/gold wires which extended to the edges of the glass substrate and provided individual access to each electrode. Following preparation of the retina patch, the electrode access wires were brought into register with conducting traces on an adjacent printed circuit board. Voltages and currents were transmitted between the edges of the array and the printed circuit board through a Zebra Connector (Fujipoly America Corp., Kenilworth, NJ, USA). Conventional .025-inch square post connectors on the circuit board board provided access to the stimulator and nerve response amplifiers.

2.4 Data acquisition

The data acquisition system consisted of: (1) a voltage-controlled current source stimulator, with monitor amplifiers to measure the stimulus current and voltage; (2) an eight-channel nerve response amplifier, consisting of a pre-amplifier board located near the retina preparation and a rack-mounted high gain amplifier; (3) a Pentium computer with analog/digital interfaces; (4) a four-channel oscilloscope; (5) a speaker. The block-diagram in Figure 2.5 illustrates how these components were connected. The stimulator, monitor amplifiers and nerve response amplifiers were designed as part of the thesis. Circuit schematics and design considerations for these appear in Appendix B.

2.4.1 Multi-channel nerve response amplifier

The nerve response amplifier consisted of eight identical channels each with gain 10,000 and bandwidth 20-10,000Hz. The input to each amplifier was connected in parallel to eight electrodes through electro-mechanical relays, with only one relay in the closed position at a time. Channel inputs were selected using either pushbutton controls or software, allowing for easy monitoring of all sixty-four electrodes on the array during an experiment. Each channel measured the voltage of a single electrode relative to an earthed platinum wire at a distant location in the bathing medium. With the electrodes platinized and the retina patch mounted on the array, the noise floor for the amplifiers was typically 5-10μV rms.

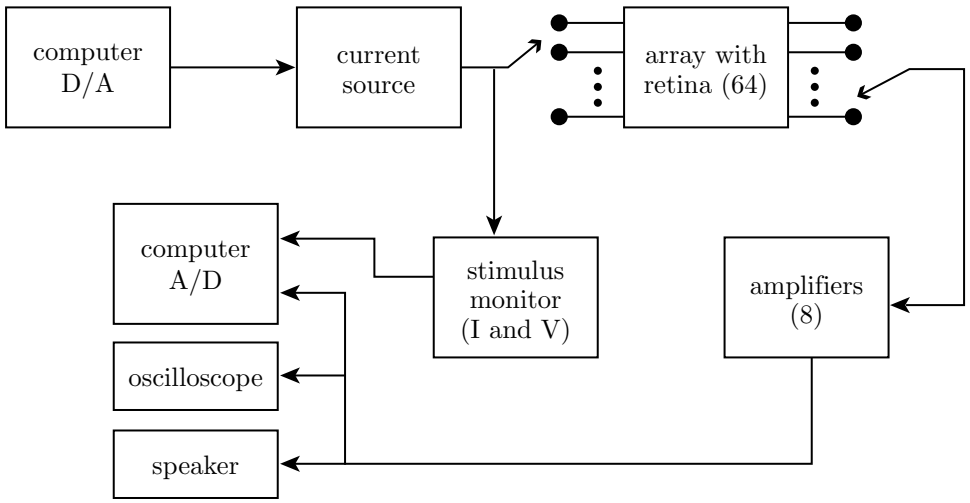

Figure 2.5: Block diagram of the data acquisition system.

2.4.2 Stimulator

The stimulator delivered a current proportional to its input voltage by 2μA/V. It was capable of delivering .01-20μA with .01μA minimum resolution, $\pm$3.5V compliance, and a 10-90% risetime of 10μs when driving electrodes. Monitor amplifiers, built on the same circuit board as the stimulator, measured the load current and voltage. The load current was determined by measuring the voltage across a 10kΩ resistor placed in series with the load.

After a number of experiments had been completed, a calibration test was performed wherein the stimulation current was measured by a second method independent of the current monitor circuit used in the experiments. With the same stimulator configuration used in the experiments, threshold-level stimulation pulses were delivered to a resistor load. The voltage across the resistor was then measured differentially using a Tektronix TAS475 oscilloscope, and the current calculated by dividing this voltage by the load resistance. The oscilloscope measurement matched that of the current monitor.

The stimulator and monitor amplifier circuits were optically isolated from earth potential, which was used as the reference voltage for amplifying nerve responses.

2.4.3 Computer interface

The computer interface was implemented on a Pentium computer running the Linux operating system. Analog and digital signals were accessed and controlled though

a PC-resident DAP3000a/212 input/output card (Microstar Laboratories, Bellevue, WA, USA). A 100kHz update rate was used for generating stimulus signals. For recording, 20kHz and 100kHz sampling rates were used for surveys of simultaneous activity at multiple sites and for threshold measurements at a single site, respectively.

A custom interface written in MATLAB was used to generate stimulation waveforms, display and analyze data, and control amplifier channel settings.

2.4.4 Oscilloscope and speakers

A four-channel oscilloscope and speaker provided additional means of monitoring nerve activity. The speaker was usually connected to a recording site with moderate spontaneous activity (see Section 2.5.1), which produced audible clicks above the baseline noise, and left on for the duration of an experiment. A steady stream of clicks over a period of hours was taken as a sign of good retinal health. The oscilloscope was used for measurements where the computer's re-plotting rate (approximately 1Hz using MATLAB's `plot()` command for eight 1000-point waveforms) was unacceptably slow. Examples included surveys of average discharge rates across the array and determinations of approximate excitation thresholds (see Section 2.5.2).

2.4.5 Reducing stimulus artifacts

A substantial effort, described further in Appendix C, was devoted to reducing stimulus artifacts. Two measures taken toward this end were particularly effective. These had the common aim of reducing coupling between the stimulating and recording instruments. First, the quality of the electrode insulation was improved by increasing the thickness of the polyimide layer from 1μm (used in early designs) to 10μm and by adding a silicon nitride layer (not present in early designs). These changes were motivated by the finding that stimulus artifacts were due in part to parasitic leakage between access wires for stimulating and recording electrodes. Compared with initial designs, the new arrays had less leakage between wires and smaller stimulus artifacts*. Second, the layout of the electrodes was modified from the original all-hexagonal arrangement (Meister et al., 1994; Regehr et al., 1989). To reduce coupling through tissue and parasitic current pathways, the electrodes were divided among two clusters spaced several hundred microns apart, with their access wires running to opposite edges of the array.

A number of conventional techniques were either found not to reduce the artifacts or were not fully exploited. A sample-and-hold circuit, for example, was placed between the preamplifier and high gain stage in all eight of the nerve response am-

*It has been suggested that the reductions in leakage and artifacts were due primarily to the addition of the silicon nitride layer, since polyimide may support ionic current flow (J. Pine – personal communication). An attempt has not been made to distinguish between contributions of thickening the polyimide and adding the silicon nitride.

plifiers, to prevent saturation and transients in high-pass filters. This circuit offered no consistent improvement. The preamplifiers did not typically saturate either, as verified by direct examination of their outputs. Hence the dominant artifact source was present at pre-amplifier inputs.

In addition, current sources and stimulus monitors were all optically isolated from the recording ground. The isolation was compromised, however, when making monopolar threshold measurements. For these measurements the negative terminal of the current source was connected to the recording ground, which served as the distant return. Stimulus artifacts in such cases were larger than for the bipolar stimulation configurations used in Chapter 3, but were still acceptable for a useful range of low-amplitude stimuli.

2.5 Physiologic recordings

2.5.1 Spontaneous and light-evoked activity

Varying amounts of nerve activity were discernible in the voltage signals at the response amplifier outputs, with spontaneous activity present on most recording sites. Spontaneously active sites produced signals consisting of a time series of discrete discharges, ranging in frequency from below one discharge/sec up to several tens of discharges/sec, superimposed on the baseline noise.

The discharges were judged to be single unit action potentials from ganglion cells (or possibly displaced, spiking amacrine cells), based on the following properties:

- **rates of spontaneous discharge** consistent with previous reports from rabbit retina (Ames III and Pollen, 1969; Caldwell and Daw, 1978; Ames III and Masland, 1976),
- **burst responses to changes in illumination** observed upon passing one's hand (darkening) or a flashlight beam (brightening) over the preparation,
- **discharge amplitudes** consistent with those obtained from salamander ganglion cells using a similar preparation (Meister et al., 1994), and
- **discharge waveforms** resembling those found in the cat retina (Kuffler, 1953).

The discharge waveforms, while somewhat variable, were well represented by the three types shown in Figure 2.6. The Type 1 discharges had a prominent initial negative deflection lasting 300-400μs, followed by a smaller, longer lasting positive deflection. Type 2 discharges had an initial positive deflection followed by a negative deflection, with a total duration comparable to that of the initial negative deflection of the Type 1 discharges. The Type 3 discharges had an initial positive-negative sequence like the Type 2 discharges, but also had a third, positive deflection.

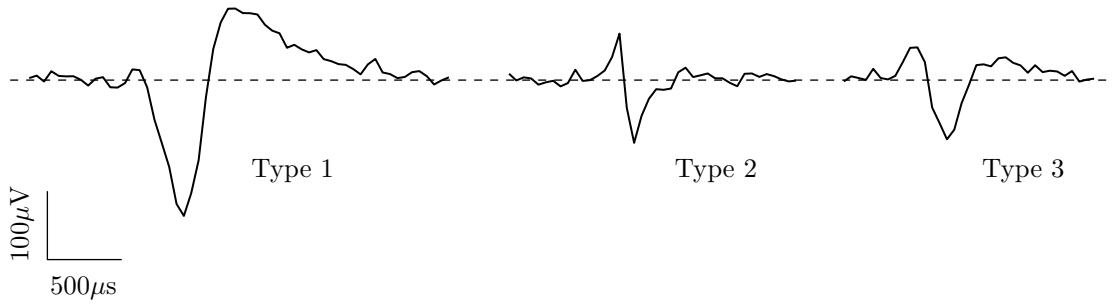

Figure 2.6: Examples of different spontaneous discharge types. Negative electrode voltages are plotted downward.

Correlated discharges on two or more electrodes, arising from pickup of the same unit, were common (Meister et al., 1994). These correlations often appeared on neighboring electrodes in the recording cluster, among all combinations of discharge types (i.e. Type i/Type j, where i, j=1,2,3). On the other hand, Type 2 discharges sometimes appeared in near simultaneity with discharges—of any type—on electrodes several hundred microns away. Furthermore, Type 2/Type 2 correlated discharges could be found on as many as four recording sites. These correlations always appeared on groups of electrodes roughly aligned with the expected optic nerve fiber direction. Closer inspection of the waveforms revealed a systematic ordering, with discharges appearing first on the recording sites furthest from the optic disk, and progressively later with decreasing distance from the disk. Apparent velocities, computed by dividing the distance between recoding sites by the time delay between negative peaks of the discharges, were 0.8-1.5m/s (n=13). These correlation properties, which were only seen for the Type 2 discharges, suggest that the Type 2 discharges were generated by ganglion cell axons, as discussed in Section 2.6.

It was also common to record numerous discharges of different types and amplitudes from a single electrode.

2.5.2 Electrically evoked activity

Properties of electrically evoked activity were studied by injecting current through stimulating electrodes while monitoring voltages in the recording cluster. All measurements in this chapter were made using a monopolar configuration, with the stimulator connected between a single stimulating electrode and the distant recording ground. Unless otherwise specified, stimuli were charge-balanced biphasic pulse pairs (anodic phase first) with 400μs phases and 400μs intra-phase delay, applied at a rate of 10/sec.

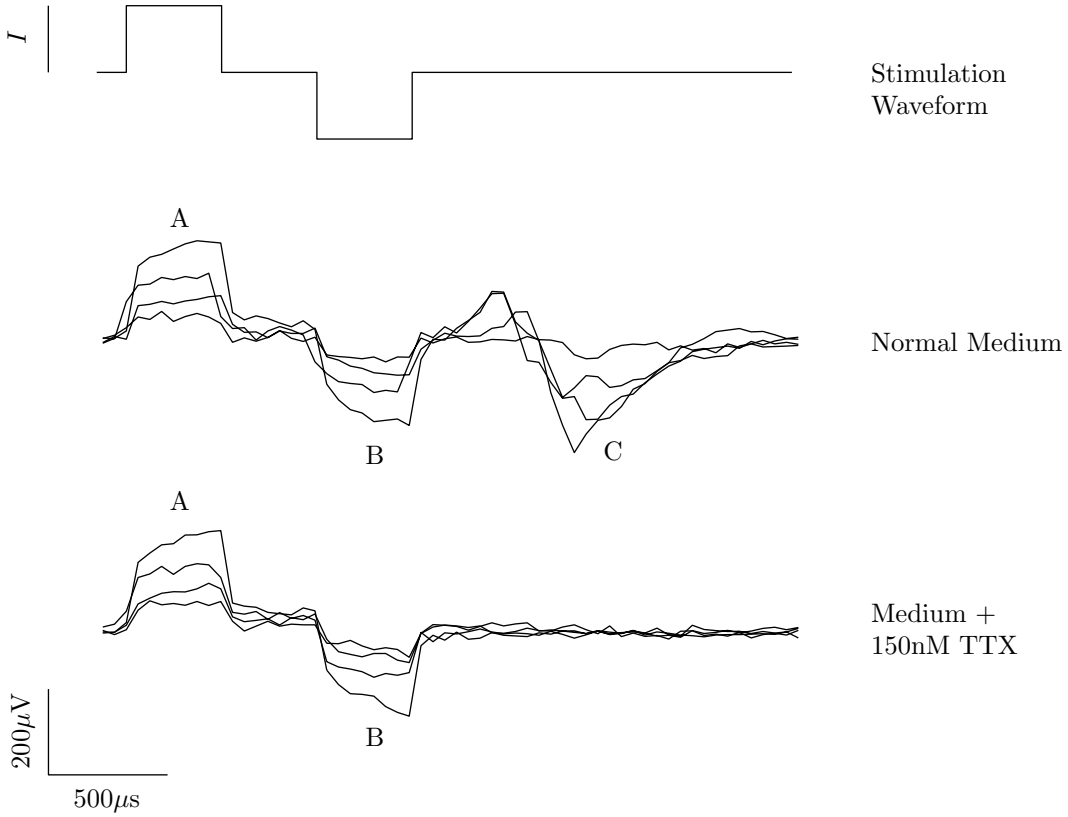

Figure 2.7: Overlay of response waveforms for four different stimulus amplitudes, before (middle traces) and after (bottom traces) addition of 150nM tetrodotoxin. The stimuli (top trace) were applied "by hand" at roughly fifteen second intervals. The amplitudes were $I = \pm.10$, $\pm.14$, $\pm.20$, and $\pm.29\mu$A.

Stimulus artifacts, graded potentials, and spikes

Figure 2.7 shows the most commonly observed responses to electric stimulation. In normal medium (middle traces), the responses had three components, labeled A, B, and C, which all grew with increasing stimulus amplitude. The A and B components were coincident with the positive and negative phases of the stimulus waveform (top trace), respectively, while component C arrived after the end of the stimulus. Addition of 150nM tetrodotoxin (TTX) abolished only the C component, as shown in the bottom traces. Hence the A and B components were stimulus artifacts while the C component was of neuronal origin.

It was also possible to record responses that, when they appeared, varied little with stimulus amplitude. This property is illustrated in Figure 2.8. Response compo-

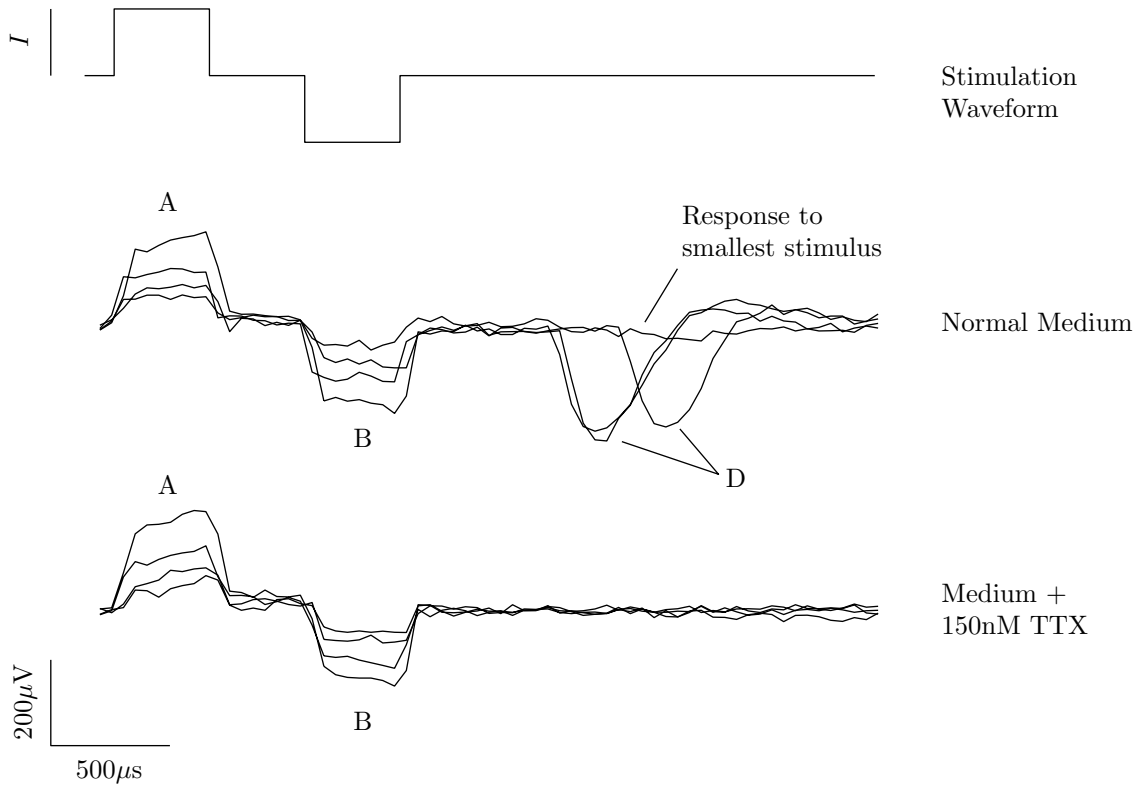

Figure 2.8: Response waveforms with an all-or-none component. Stimuli had the same timing and levels as in Figure 2.7.

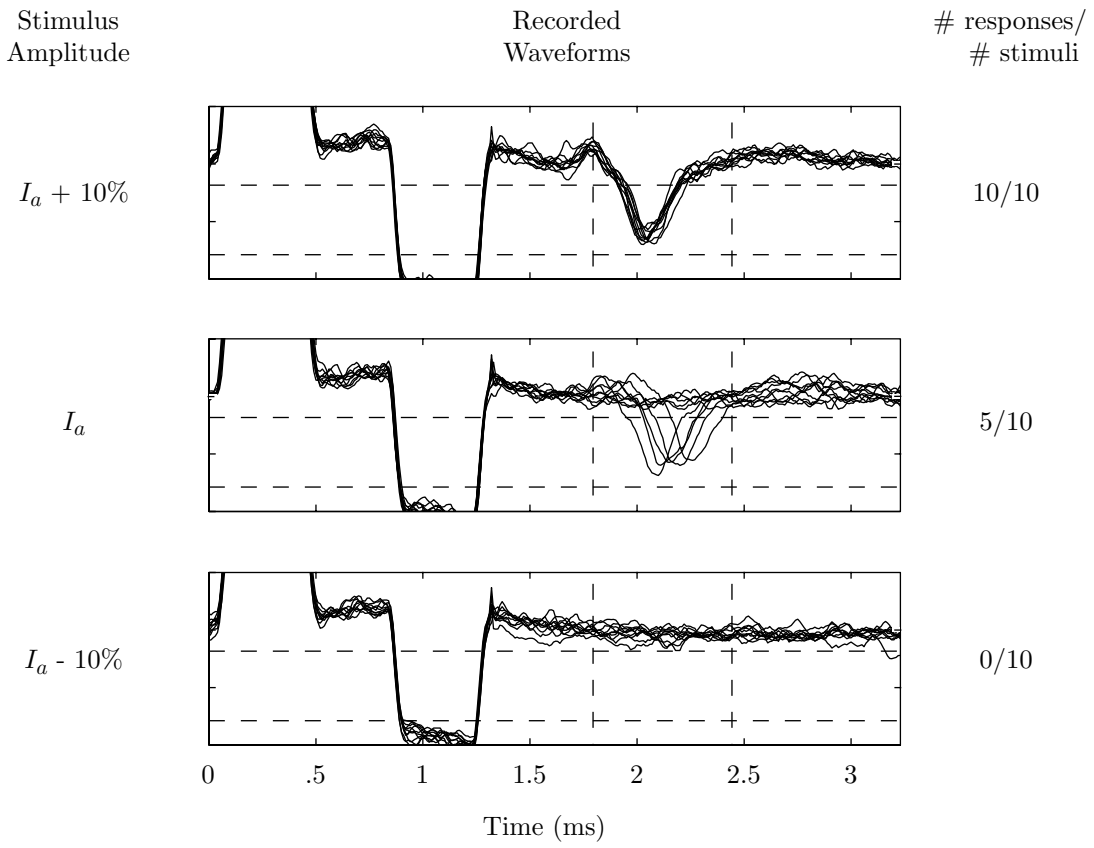

Figure 2.9: Example threshold measurement, with $I_a = .22\mu$A and the same stimulus timing as in Figure 2.7. Each waveform entering the region bounded by the dashed lines was counted as a response. Vertical ticks are at 100μV intervals.

nents A and B were stimulus artifacts as before. The D component failed to appear in response to the lowest amplitude stimulus and also after addition of 150nM TTX. While the latency of the D component was variable for the three largest stimuli, the response shape was highly conserved.

At specific threshold amplitudes the all-or-none responses appeared variably and with variable latencies. To measure thresholds precisely, an approximate threshold I_a was first determined by applying stimuli at a rate of 2-5/sec and manually varying the amplitude until the all-or-none response occurred roughly half the time. Next, the computer was used to present ten stimuli at each of three different amplitudes in a randomized order at 10/sec. Results from the automated measurement were plotted after presentation of all thirty stimuli. An example is illustrated in Figure 2.9. In this case the estimate I_a was equal to the threshold, defined as the amplitude at

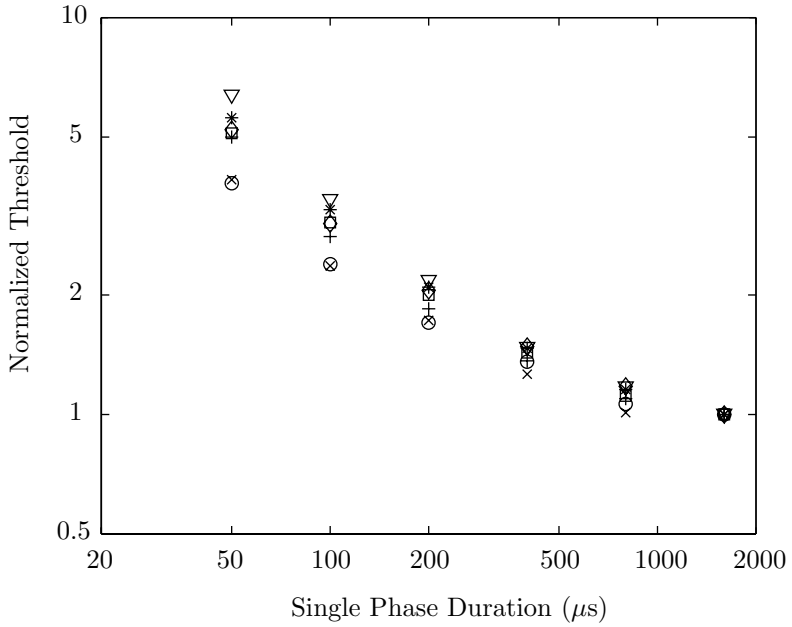

Figure 2.10: Normalized thresholds vs. phase duration for seven recording sites in seven retinas. Stimuli were anodic-first charge-balanced biphasic pulse pairs with equal phase durations and 400μs intra-phase delay. Thresholds at each recording site were normalized to the threshold for 1600μs phase duration. A unique symbol is used to plot measurements from each cell.

which responses occurred on half of the stimulus presentations. A relatively small deviation from I_a was sufficient to eliminate the variability: responses occurred on every presentation at ten percent above I_a and on no presentations at ten percent below I_a.

The thresholds for the all-or-none responses were dependent on the stimulus phase duration, as shown in Figure 2.10. Thresholds fell with increasing phase duration.

Responses were also refractory. This property was observed in several experiments, and measured carefully in one. The experiment utilized a pair of 400μs cathodal pulses, separated by a variable delay, as the stimulus. The first pulse was set to a supra-threshold amplitude, and the excitation threshold for the second pulse measured as a function of intra-pulse delay. Thresholds rose by 1.5 times as the delay between the two pulses was reduced from 4ms to 1ms.

Based on the all-or-none, duration-dependent, and refractory properties, as well as sensitivity to TTX, these responses were judged to be single unit spikes.

Additional properties of spike responses

While stimuli were almost always biphasic, the cathodic phase of the stimulus was most effective for generating spikes. The roles of the anodic and cathodic phases in spike generation were investigated by applying anodic-first and cathodic-first stimuli to the same unit. As exemplified in Figure 2.11, spike responses tracked the cathodic phase of the stimulus. The spikes were generated by the cathodic phase, and hence cathodic thresholds were lower than anodic thresholds. Furthermore, thresholds were the same for anodic-first and cathodic-first stimuli for a 400μs intra-phase delay. Anodic-first stimuli were used in order to minimize contamination of the response signal by the stimulus artifact.

A number of additional properties were characterized to support the claim (see Section 2.6) that responses were due to direct stimulation of ganglion cell axons. Two properties suggested that stimulation was direct rather than trans-synaptic. First, as suggested by the tests for refractoriness, spikes could be generated at high repetition rates. An example is illustrated in Figure 2.12, where responses were produced at approximately 2ms intervals. Second, spike responses were robust to addition of 200μM cadmium (a synaptic blocker) to the bathing medium. During fifteen minute period following start of cadmium flow, thresholds fluctuated but remained close to (within 30% of) pre-cadmium values. By contrast, responses to light were eliminated within minutes of the introduction of cadmium.

In a third type of measurement, thresholds were determined at numerous locations in the stimulating electrode cluster to produce a rough map of the target. Threshold variations with distance were different for the horizontal and vertical directions on the stimulating grid, as shown in the map of Figure 2.13.

The lowest thresholds on the map occurred along a vertical line, presumably closest to site(s) of excitation, with thresholds rising to the left and right. While the thresholds varied with vertical distance in the left and right columns, the threshold change per unit distance was at least a factor of two smaller than variations in the horizontal direction. Hence the target had an elongated, nearly vertically aligned geometry. This pattern of threshold changes was consistent across a number of experiments which will be described in Chapter 3.

Additional notes on threshold measurements

Dashed lines like the ones in Figure 2.9 were used to define a range of amplitudes and a segment of time that were used as a criteria for discriminating all-or-none responses from other signal components such as stimulus artifacts and discharges from other neurons. The line positions, which could be altered as needed during an experiment, were always identical in the response plots for the three different stimulus amplitudes used for each threshold measurement (see Figure 2.9). The tallies on the right side of the Figure were computed by counting only response waveforms with ten or more sample points ($\geq$100μs total duration) in the region bounded by the four lines.

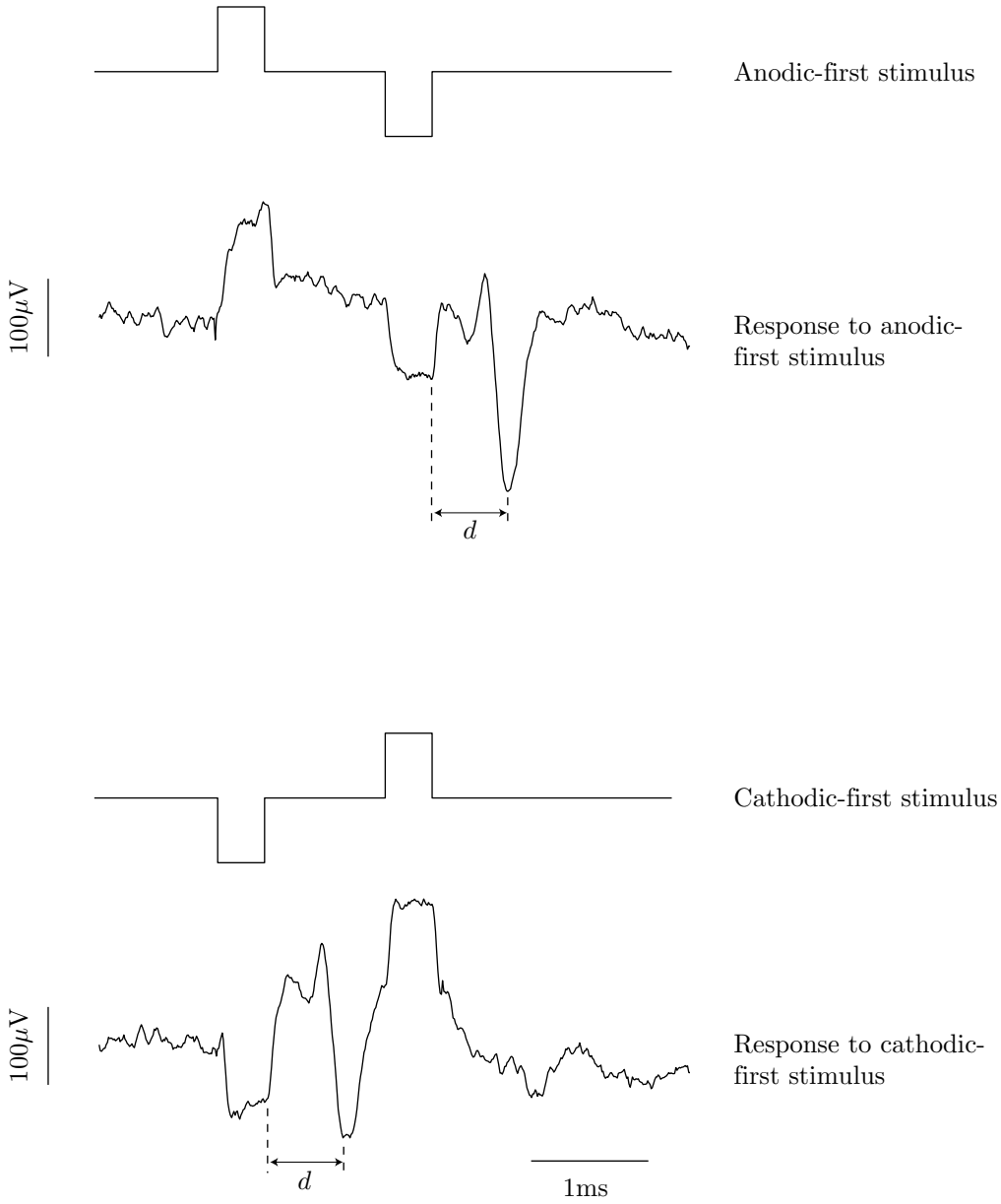

Figure 2.11: Stimulus and response waveforms for anodic-first and cathodic-first stimulation. The interval from the end of the cathodic phase to the negative peak of the spike, indicated by the horizontal lines below each waveform, was equal for the two cases ($d = 620\mu$s). An unusually long intra-phase delay of about 1ms was used to minimize contamination of the response by the artifact accompanying the anodic phase of the cathodic-first stimulus. The stimulus level was .17μA.

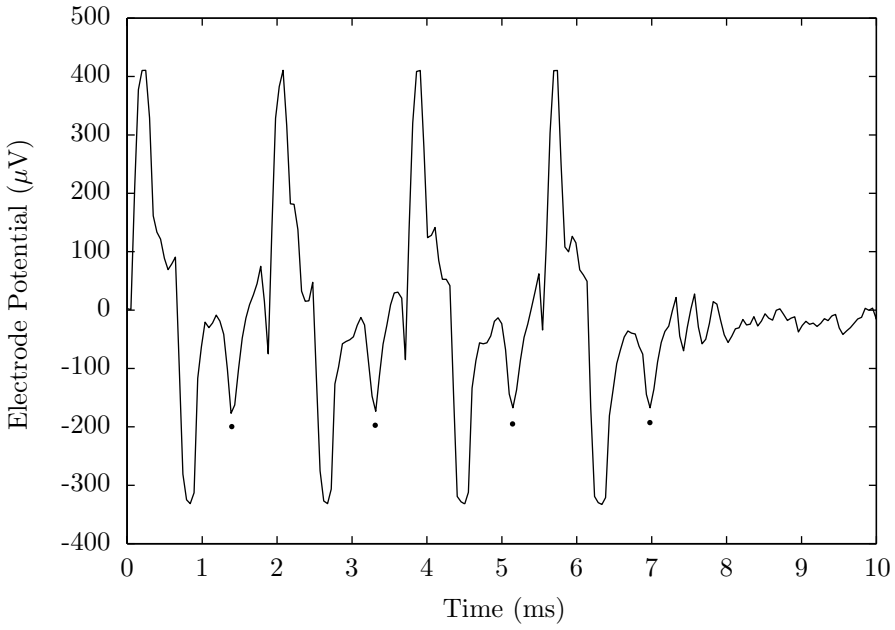

Figure 2.12: Responses to repetitive supra-threshold stimulation at approximately 500 stimuli/sec. Spikes are indicated by the dots below them.

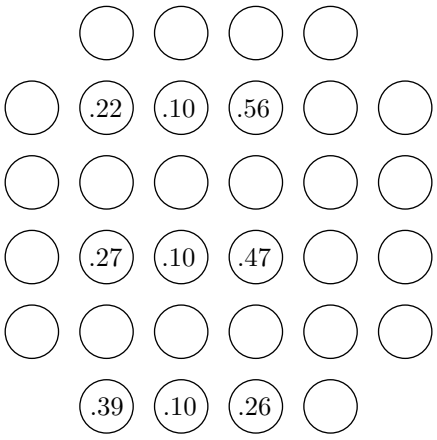

Figure 2.13: Map of thresholds for a single unit, measured by connecting the stimulator to nine different electrodes in the stimulating electrode cluster, one electrode at a time. Thresholds are in μA.

Since the recording electrodes often picked up discharges from multiple neurons, the shape of an all-or-none spike was stored at the beginning of a series of measurements. The stored spike was then displayed on the computer screen in a contrasting color while additional responses were measured. A series of responses—measured against variations in some stimulation parameter—was only attributed to one cell if these responses could be distinguished from other signal components and if they resembled the template.

The initial threshold estimate I_a was not always exact as in Figure 2.9. In cases where less than five responses were generated at one of the stimulus amplitudes and more than five responses were generated at a larger amplitude, thresholds were estimated by linear interpolation.

Control measurements, taken under nominally the same conditions as an earlier measurement, were often made during the course of an experiment. These usually fell within $\pm 10\%$ of the initial measurement. Out of 25 repeat measurements from eight cells, for example, 19 of these were within $\pm 10\%$ of the initial measurement and all were within $\pm 26\%$.

2.6 Discussion

This chapter has described a method for electrically stimulating and recording from retinal neurons using a multi-electrode array, and illustrated basic properties of the responses thereby obtained. One of the primary strengths of this method was illustrated in the example map of Figure 2.13, where excitation thresholds for a large number of electrode configurations were rapidly measured without any mechanical disruption of the retina preparation. This capability will be further exploited in Chapter 3. A second strength of this method is the great flexibility it affords in the design of stimulating electrode geometries. Further application of this advantage to the optimization of stimulation parameters for an epi-retinal prosthesis will be the focus of future work, as discussed in Chapter 5.

The arrangement of electrodes and orientation of the retina on the array were chosen to facilitate the study of excitation thresholds for ganglion cell axons. Several lines of evidence weigh against other stimulation sites such as pre-synaptic neurons or somata. Two different results discount the possibility of trans-synaptic stimulation. First, the responses remained in the presence of the synaptic blocker cadmium, at a concentration which eliminated responses to light and which completely blocked excitatory inputs to salamander ganglion cells (Mittman et al., 1990)[†]. Second, the spikes could be produced repetitively at intervals comparable to those required for synaptic transmission.

[†]A much larger concentration of 2mM cadmium chloride has been used in some amphibian experiments(Greenberg, 1998a; Grumet et al., 1998). This concentration was unusable in Ames' medium, which is commonly used for rabbits but for not amphibians, due to the formation of precipitate at physiologic pH.

Additional considerations show that the possibility of soma stimulation is unlikely. Spike responses were recorded at sites 300-700μm more distant from the optic disk than the stimulating electrodes. Were excitation initiated in nearby somata, the largest of which are perhaps 30μm in diameter (Amthor et al., 1983; Peichl et al., 1987), the responses could only have been recorded from axons or dendrites. Neither of these possibilities is likely, however, since axons course toward the optic disk upon emerging from somata and because dendrites, owing to their small caliber and large distance from the retinal surface, make them poor targets for recording with a planar electrodes. In addition, threshold variations with distance were strongly direction-dependent, in one case remaining constant despite a 100μm electrode displacement along the expected axon direction (middle column of Figure 2.13). Thus the target had an elongated geometry and was aligned with the expected axon direction.

The above arguments do not rule out the possibility that dendrites were stimulated in addition to, or instead of, axons. In some ganglion cell types these can extend many hundreds of microns from somata (Amthor et al., 1983; Peichl et al., 1987), which would be just sufficient to span the distance between the stimulating and recording clusters on the electrode array (see Figure 2.2). Furthermore, antidromic propagation of action potentials in the dendrites of retinal ganglion cells has recently been demonstrated (Velte and Masland, 1999). Hence it is conceivable that the spike responses were initiated in dendrites. This possibility will be given further consideration in Section 3.5.4.

Reports of direct stimulation of ganglion cell axons and dendrites are rare in the literature on electrical stimulation of retina (see Section 1.2 for a review). In most cases the lowest threshold stimuli acted directly on photoreceptors or bipolar cells. The present results are not in conflict with these reports because focal responses—such as would be expected for photoreceptor or bipolar cell stimulation—would probably not be found on electrodes in the distant recording cluster. In fact, spike responses were commonly observed on electrodes within the stimulating cluster, though these were not carefully studied.

The anatomical origin of the response signals deserves consideration. There is some evidence that the sources of the all-or-none responses can be deduced from the spike shapes. These responses strongly resembled the spontaneous discharge types of Figure 2.6, most commonly Type 1 or Type 3. Consider first the Type 2 spontaneous discharges, which were almost certainly recorded from ganglion axons. These had diphasic, initially positive shapes similar to those predicted by biophysical models for fibers (Plonsey, 1969; Woodbury, 1960), and were observed propagating toward the optic disk with velocities comparable to those of cat ganglion cell axons (Stanford, 1987). Furthermore, the light responses of spikes with similar shapes were described in detail by Kuffler in his studies of cat retina (Kuffler, 1953). Since they could be recorded at various displacements from the unit's optic receptive field, Kuffler attributed these spikes to axons. Kuffler also recorded spikes resembling the initially negative Type 1 discharges, attributing them to somata since they were always

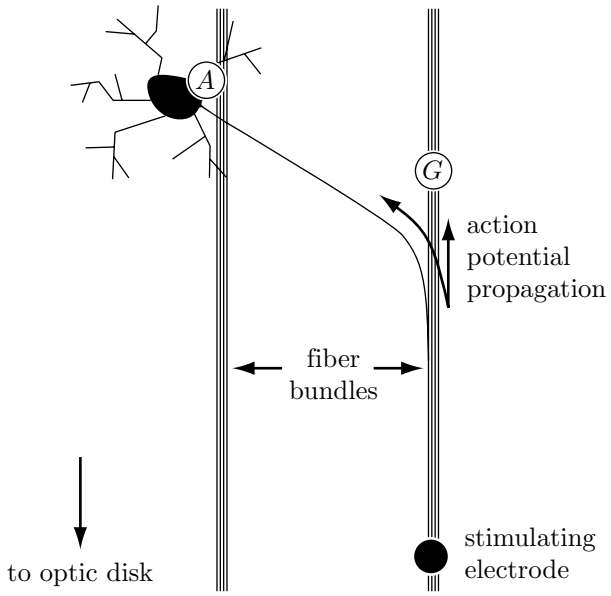

Figure 2.14: Speculative drawing of the anatomy underlying graded and all-or-none responses. A : Recording electrode with all-or-none response; G : recording electrode with graded response.

recorded within the optic receptive field (Kuffler, 1953). Hence the responses resembling Type 1 were probably due to nearby somata. The origin of the responses resembling Type 3 spontaneous discharges is less clear. Though their tri-phasic shape was also consistent with biophysical models for fibers, spontaneous Type 3 discharges were never seen propagating toward the optic disk.

The frequently observed graded responses were most likely compound action potentials in groups of ganglion cell axons, which gather into bundles as they course toward the optic disk (Peichl et al., 1987; Vaney, 1980). It is curious in light of this arrangement that the planar recording electrodes, which were large compared with conventional sharp-ended electrode tips, could isolate single unit responses at all. A clue to this dilemma comes from the observation that ganglion cell axons sometimes emerge from somata at oblique angles, crossing over one or more fiber bundles before joining one (Peichl et al., 1987). This situation is illustrated in Figure 2.14. An all-or-none response is picked up by the A recording electrode because the adjacent soma extends its axon near the stimulating electrode. Even though a fiber bundle also passes by this recording electrode, no graded responses are seen because this bundle is far from the stimulating electrode.

The scheme of Figure 2.14 also suggests that graded potentials might arise on

the A recording electrode for some stimulating electrode positions, even though all-or-none responses could be generated at others. In fact, this phenomenon was often observed in the threshold versus displacement experiments of Chapter 3.

Chapter 3

A Study of Fiber Excitation Thresholds Using Monopolar and Bipolar Stimulating Electrodes

3.1 Introduction

This chapter takes an experimental look at the problem of how to raise thresholds for stimulating axons. The experiments were motivated by reports that the excitability of elongated structures, such as axons or muscle cells, depended strongly on the orientation of the imposed electric field relative to the long axis of the structure. Thresholds were low with the stimulating field oriented along a structure and were high with the field oriented across the structure (Ranck, 1975; Ranjan and Thakor, 1995; Rushton, 1927; Tung et al., 1991). Analytical models employing infinite parallel plate stimulating electrodes and linear passive fibers predict transmembrane potential changes in accordance with this trend. In the steady state, longitudinal fields produce larger depolarizations than transverse fields provided that the plate separation is larger than a fiber diameter (Grumet, 1994; Plonsey and Altman, 1988).

These trends led my research group to hypothesize that axon thresholds could be raised with electrodes that minimize the longitudinal component of the stimulating field (Grumet, 1994; Wyatt and Rizzo, 1996). Experimental tests of this hypothesis were conducted using the apparatus described in Chapter 2, with the stimulator connected between electrode pairs oriented along or across target fibers (ganglion cell axons and possibly dendrites—see Sections 2.6 and 3.5.4) on the surface of the rabbit retina.

In addition, thresholds for monopolar stimulation (with distant return) of each fiber were measured at numerous sites in the stimulating electrode cluster. These were used to estimate the fiber locations, which provided a common reference frame for aggregating threshold data. A rough estimate of fiber locations could be made simply by inspection of threshold maps like the one in Figure 2.13. To illustrate,

the minimum threshold in that map (.1μA) appeared on three electrodes in the third column from the left. Hence the fiber was roughly aligned with this column. The fiber was probably not perfectly vertical, however, because the thresholds in the second and fourth columns varied along the vertical dimension. The thresholds in the second column decreased from .39μA to .22μA with increasing height in the column, whereas the thresholds in the fourth column increased from .26μA to .56μA. These variations were consistent with a fiber orientation which was rotated slightly counter-clockwise from vertical.

The fiber location estimates were formalized using two different mathematical models for thresholds as a function of distance to the monopolar stimulating electrode. The first model is derived from first principles. The second model is an empirical model. Predictions for bipolar thresholds were also developed for each model. The models are presented in the following section, and their application to location estimates is explained in Sections 3.3.2 and 3.6.

3.2 Models

3.2.1 First principles model

Activating function

A number of simplifying assumptions are made to model threshold variations with electrode position and orientation. The first is that axons satisfy the assumptions of the core conductor model. This general model underlies the cable and Hodgkin-Huxley models, but makes no assumptions regarding the electrical properties of the membrane. We will make use of the following core conductor equations (Weiss, 1996),

$$\frac{\partial I_i(z,t)}{\partial z} = -K_m(z,t),$$

$$\frac{\partial V_i(z,t)}{\partial z} = -r_i I_i(z,t),$$

$$V_m(z,t) = V_i(z,t) - V_o(z,t),$$

where z measures distance along the fiber, t is time, I_i is the axial current flowing in the fiber, K_m is the membrane current per unit length, V_i is the intracellular potential, r_i is the intracellular resistance per unit length, V_m is the membrane potential, and V_o is the potential on the outer surface of the membrane. These equations can be manipulated to yield

$$-\frac{\partial^2 V_m(z,t)}{\partial z^2} + r_i K_m(z,t) = \frac{\partial^2 V_o(z,t)}{\partial z^2} \tag{3.1}$$

which relates the membrane potential and current to the extracellular potential. The relation shows that the effective drive term for the membrane current and potential is the second spatial derivative of the extracellular potential in the longitudinal direction,

$$f_a = \frac{\partial^2 V_o(z,t)}{\partial z^2}.$$

This "activating function" f_a provides a useful tool for predicting fiber responses under a variety of stimulation conditions (Rattay, 1986). From equation 3.1, a positive activating function results in either an outward membrane current, a concave-downward membrane potential versus position, or both. The net result is to locally raise or depolarize the membrane potential. By a similar argument, a negative activating function tends to hyperpolarize the membrane. Thus the activating function may be taken as a rough picture of the membrane potential changes induced in a fiber by an extracellular stimulus.

Activating functions for stimuli used here may be derived if the following additional assumptions are made: 1) the tissue may be modeled as a uniform, linear conductor; 2) the presence of the fiber may be ignored when calculating the potential distribution during stimulation; 3) the planar, ten micron diameter electrodes may be modeled as point sources.

To calculate the activating function for a point source, we begin by finding the voltage it generates along a fiber. Consider a fiber oriented in the z-direction and a point source in the $z = 0$ plane, as illustrated in Figure 3.1a. The potential at points along the fiber is given by

$$V_o = \frac{i}{4\pi\sigma}(z^2 + D^2)^{-1/2},$$

where i is the stimulating current, σ is the conductivity of the medium, D is the minimum distance between the point source and fiber.

Carrying out the derivatives yields the activating function,

$$f_a = \frac{i}{4\pi\sigma}(z^2 + D^2)^{-5/2}(2z^2 - D^2).$$

Figure 3.1b illustrates the shape of the curves for cathodal stimuli ($i < 0$) located at $D = 1, 1.5$ and 3. The plots are consistent with two expected outcomes. First, the activating function is maximal, or most strongly depolarizing, at the point along the fiber which is closest to the cathode ($z = 0$). Second, the maximal value decreases with increasing distance between electrode and fiber.

Thresholds for monopolar stimulation

These observations suggest a simple way to model the threshold increase accompanying electrode movement away from the fiber. Consider the activating function's

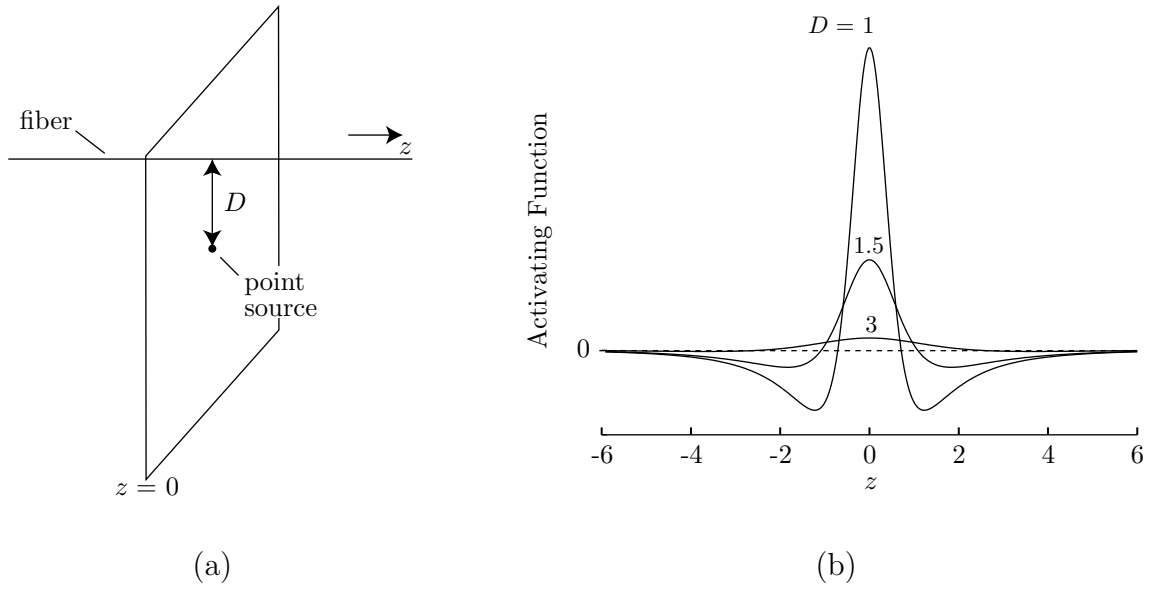

Figure 3.1: Activating functions for a point source electrode. (a) Point source in the $z = 0$ plane, at a distance D from the fiber. (b) Activating functions for cathodal stimuli at $D = 1, 1.5, 3$.

maximum, at $z = 0$, for a threshold stimulus $i = -I_{thr}$ with the point source at a specific distance D_o,

$$f_a|_{\max,\text{thr}} = \frac{I_{thr}(D_o)}{4\pi\sigma} D_o^{-3}.$$

Now, if it can be assumed that the threshold value of f_a is independent of distance, we have

$$I_{thr}(D) = kD^3, \tag{3.2}$$

where

$$k = (4\pi\sigma)\ f_a|_{\max,\text{thr}}\,.$$

Equation 3.2 predicts the shape of the threshold versus position curve for a monopolar point source electrode. This equation can be viewed as the product of two factors, one describing spatial properties of the stimulus (D^3) and one containing information about the tissue and fiber (k).

Bipolar thresholds: along orientation

The approach which yielded equation 3.2 is readily applied to the bipolar stimulation case. For simplicity we will assume that the fibers are oriented exactly parallel or perpendicular to the bipolar electrode pair.

(a) (b)

Figure 3.2: Bipolar stimulation (a) along fiber and (b) across fiber using a pair of point sources separated by a distance d. *Abbreviations:* a=anode; c=cathode.

Figure 3.2a illustrates the case where a bipolar electrode pair is oriented along a fiber. The cathode c is located at $z = 0$ and the anode a is located at $z = d$. The fiber is at a lateral displacement x_o from the electrodes and at a height h. The activating function for the bipolar pair is

$$f_a = \frac{|i|}{4\pi\sigma}\{ \quad [x_o^2 + h^2 + (z-d)^2]^{-5/2}[2(z-d)^2 - x_o^2 - h^2] - \\ (x_o^2 + h^2 + z^2)^{-5/2}(2z^2 - x_o^2 - h^2) \ \}.$$

The shape of this function can be obtained by taking one of the curves in Figure 3.1b and subtracting a shifted version of itself. To a good approximation, the maximum value aligns with the cathode at $z = 0$, as before. Hence the threshold is given approximately by

$$I_{thr} = \frac{k}{(x_o^2 + h^2 + d^2)^{-5/2}(2d^2 - x_o^2 - h^2) + (x_o^2 + h^2)^{-3/2}}. \tag{3.3}$$

Bipolar thresholds: across orientation

Figure 3.2b illustrates the case where a bipolar electrode is oriented across the fiber. Both anode and cathode are located at $z = 0$. The fiber is at a height h above the point sources, and is laterally situated between cathode and anode. The lateral distance to the cathode is x_o, and the lateral distance to the anode is $d - x_o$. The activating function for the bipolar pair is

$$f_a = \frac{|i|}{4\pi\sigma}\{ \quad [(d-x_o)^2 + h^2 + z^2]^{-5/2}[2z^2 - (d-x_o)^2 - h^2] - \\ (x_o^2 + h^2 + z^2)^{-5/2}(2z^2 - x_o^2 - h^2) \ \}.$$

The shape of this function can be obtained by taking one of the curves in Figure 3.1b and subtracting a scaled version of itself. If we assume the cathode is closer to the fiber than the anode (consistent with the experiments described in the sections to follow) the maximum value aligns with the cathode at $z = 0$ and the threshold is given by

$$I_{thr}(x,h) = \frac{k}{(x_o^2+h^2)^{-3/2} - [(d-x_o)^2+h^2]^{-3/2}}. \tag{3.4}$$

3.2.2 Empirical model

In numerous experiments reported in the literature, the relationship between threshold and distance was well-described by

$$I_{thr} = \hat{k}D^2 + I_{min} \tag{3.5}$$

where I_{thr} is the excitation threshold, $\hat{k}$ is a constant having different units than k above, D is the distance between the electrode and target, and I_{min} is the minimum threshold (Tehovnik, 1996). Note that I_{min} is effectively zero for the first principles model since the activating function for a point source becomes infinite at zero distance.

Extension of this model to the bipolar case is less straightforward than for the first principles model. One plausible approach is suggested by the fact that in an unbounded, uniform linear medium the electric field magnitude for a point source of current is

$$|\mathbf{E}| = \frac{|i|}{4\pi\sigma r^2}$$

where $\mathbf{E}$ is the electric field and r is the distance from the source. If D is defined as the minimum distance between the point source and a fiber, the maximum electric field magnitude experienced by the fiber is

$$|\mathbf{E}|_{max} = \frac{|i|}{4\pi\sigma D^2}$$

assuming that the field at the fiber is not modified by the presence of the fiber. Consider this maximum for a threshold stimulus $i = -I_{thr}$ with the point source at a specific distance D_o,

$$|\mathbf{E}|_{max,thr} = \frac{I_{thr}}{4\pi\sigma D_o^2}.$$

If it can be assumed that the threshold value of $|\mathbf{E}|$ is independent of distance, then

$$I_{thr} = \hat{k}D^2 \tag{3.6}$$

where

$$\hat{k} = (4\pi\sigma)|\mathbf{E}|_{\mathrm{max,thr}}.$$

This result is equivalent to equation 3.5 provided that I_{min} is zero.

Bipolar thresholds: along orientation

If the cathode in Figure 3.2a is located at the origin, the normalized electric field components generated by the bipolar electrode pair at points $(x = x_o, y = h, z)$ along the fiber are given by

$$\begin{aligned}
\overline{\mathrm{E}}_x &= x_o \left\{ (x_o^2 + h^2 + z^2)^{-\frac{3}{2}} - \left[x_o^2 + h^2 + (z-d)^2 \right]^{-\frac{3}{2}} \right\}, \\
\overline{\mathrm{E}}_y &= h \left\{ (x_o^2 + h^2 + z^2)^{-\frac{3}{2}} - \left[x_o^2 + h^2 + (z-d)^2 \right]^{-\frac{3}{2}} \right\}, \\
\overline{\mathrm{E}}_z &= z(x_o^2 + h^2 + z^2)^{-\frac{3}{2}} - (z-d) \left[x_o^2 + h^2 + (z-d)^2 \right]^{-\frac{3}{2}}
\end{aligned}$$

where normalization was accomplished by dividing each field component by $i/4\pi\sigma$. The magnitude of the normalized field is computed from

$$|\overline{\mathbf{E}}| = \sqrt{(\overline{\mathrm{E}}_x)^2 + (\overline{\mathrm{E}}_y)^2 + (\overline{\mathrm{E}}_z)^2}.$$

The maximum magnitude, which occurs at $z = 0$ (and also at $z = d$), can be readily calculated for specified x_o, h, and d. As in the monopolar case, the predicted threshold is proportional to the reciprocal of this maximum value,

$$I_{thr} = \frac{\hat{k}}{|\mathbf{E}|_{max}(x_o, h, d)}. \tag{3.7}$$

Bipolar thresholds: across orientation

If the cathode in Figure 3.2b is located at the origin and the anode is located at $(x = d, y = 0, z = 0)$, the normalized electric field components generated at points $(x = x_o, y = h, z)$ along the fiber are given by

$$\begin{aligned}
\overline{\mathrm{E}}_x &= \left\{ x_o(x_o^2 + h^2 + z^2)^{-\frac{3}{2}} - (x_o - d) \left[(x_o - d)^2 + h^2 + z^2 \right])^{-\frac{3}{2}} \right\}, \\
\overline{\mathrm{E}}_y &= h \left\{ (x_o^2 + h^2 + z^2)^{-\frac{3}{2}} - \left[(x_o - d)^2 + h^2 + z^2 \right]^{-\frac{3}{2}} \right\}, \\
\overline{\mathrm{E}}_z &= z \left\{ (x_o^2 + h^2 + z^2)^{-\frac{3}{2}} - \left[(x_o - d)^2 + h^2 + z^2 \right]^{-\frac{3}{2}} \right\}.
\end{aligned}$$

The maximum magnitude, which occurs at $z = 0$, can be readily calculated for specified x_o, h, and d. The predicted threshold is proportional to the reciprocal of this maximum value.

3.3 Methods

3.3.1 Threshold measurements

The methods for isolating rabbit retinas, sustaining them *in vitro*, and recording responses from their neurons to electric stimulation are described in Chapter 2. All

threshold measurements used the same charge-balanced, four hundred microsecond per phase rectangular stimulus with a four hundred microsecond delay between phases (also shown in Figure 3.3d).

After mounting the retina in its chamber, a search was performed to find a recording electrode which exhibited all-or-none responses to stimulation through one of the stimulating electrodes. A platinum wire at the edge of the bath served as both the current source return and the recording ground. Responses were monitored on eight electrodes at a time as the amplitude of the stimulus waveform was varied from zero to approximately $\pm.3\mu$A. Compound responses, which grew in proportion to the stimulus, were picked up on the majority of the electrodes. When an all-or-none response was found, the excitation threshold was measured and the response shape stored for comparison with subsequent measurements. This provided a check against attributing responses of two or more cells to a single cell, as discussed in Chapter 2.

Next a threshold map was created from which the fiber's lateral displacement within the stimulating grid and tilt angle relative to vertical could be deduced. This was done by measuring a series of monopolar thresholds using adjacent electrodes along several rows of the stimulating grid, progressing along each row until a point of minimum threshold was found. One such map is shown in Figure 2.13. The number and distribution of threshold measurements in the map, a total of nine along three rows, was typical. Complete maps employing all thirty-two electrodes were not made primarily because stimulus artifacts often overtook the response signals as thresholds grew at large distances from the electrodes yielding lowest thresholds. Also, threshold measurements in additional rows (made on a few occasions) did not substantially alter the fiber position estimates.

Mapping efforts were often unsuccessful due to the appearance of responses from units other than the one initially identified. A recording electrode might pick up all-or-none responses to stimulation through some stimulating electrodes and graded responses to stimulation through others, as discussed at the end of Chapter 2. The distortion contributed by the firing of additional cells often made it impossible to accurately determine the threshold for the cell of interest. The search and mapping process was repeated until a recording electrode was found for which a complete map could be successfully produced. A map was considered complete when a single local minimum could be found in each row for two or more rows.

Once a map was successfully completed, thresholds were measured with the current source connected in different bipolar configurations on the stimulating grid. Bipolar electrode pairs were oriented either along or across the fiber as illustrated in Figure 3.3a and b, respectively. These measurements were always made in pairs. In each pair, the positive current source terminal, indicated by a + in Figure 3.3c, was held fixed. The orientation of the bipolar electrode pair was then controlled by switching the negative terminal (–) between either of two return electrodes. Hence a total of three electrodes was used for each pair of measurements. These electrodes usually had unequal monopolar thresholds, presumably due to unequal electrode-fiber

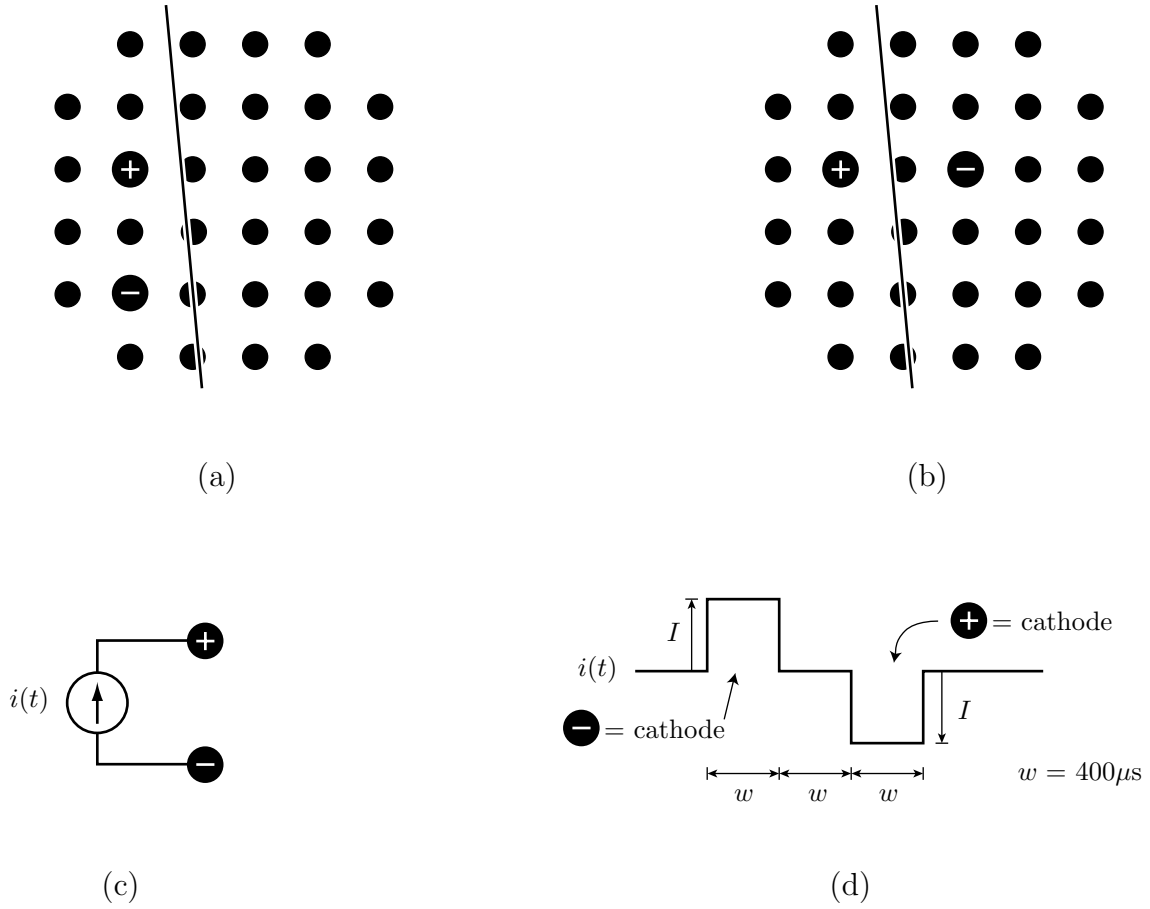

Figure 3.3: Bipolar stimulation: (a) Stimulation along the fiber; (b) Stimulation across the fiber; (c) Current source connections; (d) Drive waveform. Note that because the drive is biphasic, both the + and - electrodes are driven negatively (i.e. cathodically) during each stimulus presentation. The fiber location, indicated by a dark line in (a) and (b), was estimated from the map in Figure 2.13 using the method described in Section 3.3.2.

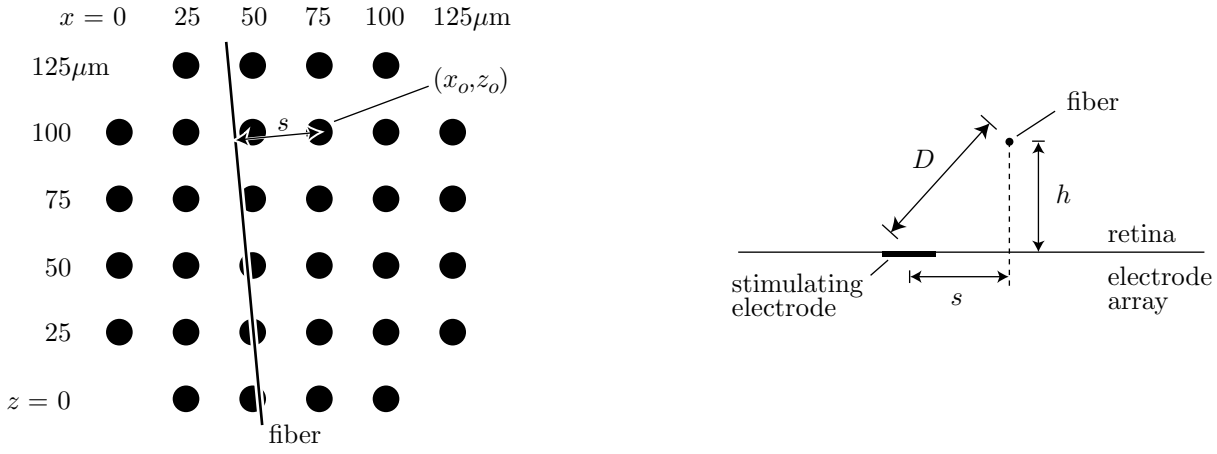

(a) (b)

Figure 3.4: Relative positions of electrodes and fiber. (a) Head on view of the array and fiber. s is the minimum distance from an electrode centered at (x_o, z_o) to the fiber's projection onto the plane of the array. (b) Cross-section view. The fiber extends out of the page, at a height h above the array.

separations. For reasons described in Section 3.4.2, the fixed and moving electrodes were chosen so that the fixed electrode had the lowest monopolar threshold of the three. One to five pairs of measurements was made on each of five fibers. The bipolar electrode pair separation d was always 50μm.

3.3.2 Data analysis

To use the models presented in Section 3.2 to estimate fiber positions, coordinate axes were superimposed on the fiber and stimulating electrodes, as shown in Figure 3.4(a). The fiber was assumed to be a straight line satisfying

$$\left.\begin{array}{c} x + bz + c = 0, \\ y = h, \end{array}\right\} \tag{3.8}$$

where b and c were unknown constants describing the position and angle of the fiber in the plane of the electrode array, and h was the unknown height of the fiber above the array. Defining s as the minimum distance from a point (x_o, z_o) in the xz-plane to the fiber's projection onto the plane, it followed that

$$s = \frac{|x_o + bz_o + c|}{\sqrt{1 + b^2}}, \tag{3.9}$$

$$D^2 = s^2 + h^2. \tag{3.10}$$

The relationship between D, s, and h is illustrated in Figure 3.4b.

The remaining steps in the position estimates differed slightly for the two models. The first principles model is used here to demonstrate the technique. The similar procedure for the empirical model is given in Section 3.6.

Substituting for D and s in equation 3.2 yielded

$$I_{thr} = k\left\{\frac{(x_o + bz_o + c)^2}{1+b^2} + h^2\right\}^{3/2} \tag{3.11}$$

Each threshold map consisted of a set of x_o's, z_o's, and corresponding I_{thr}'s from which the unknown parameters b, c, k and h could be estimated. This process began by re-writing equation 3.11

$$I_{thr}^{2/3} = a_1 x_o^2 + a_2 x_o + a_3 + a_4 x_o z_o + \left(\frac{1}{2}\frac{a_2 a_4}{a_1}\right) z_o + \left(\frac{1}{4}\frac{a_4^2}{a_1}\right) z_o^2, \tag{3.12}$$

where

$$a_1 = \frac{k^{2/3}}{1+b^2}, \tag{3.13}$$

$$a_2 = \left(\frac{k^{2/3}}{1+b^2}\right)(2c), \tag{3.14}$$

$$a_3 = k^{2/3}\left(\frac{c^2}{1+b^2} + h^2\right), \tag{3.15}$$

$$a_4 = \left(\frac{k^{2/3}}{1+b^2}\right)(2b). \tag{3.16}$$

A nonlinear least-squares fit was then performed on the two-thirds power of the thresholds to obtain parameters a_1, a_2, a_3, and a_4 which best satisfied equation 3.12 for each threshold map.

The parameters b, c, k and h were then calculated as follows:

$$b = \frac{a_4}{2a_1}, \tag{3.17}$$

$$c = \frac{a_2}{2a_1}, \tag{3.18}$$

$$k = \left[a_1(1+b^2)\right]^{3/2}, \tag{3.19}$$

$$h = \sqrt{\frac{a_3}{k^{2/3}} - \frac{c^2}{1+b^2}}. \tag{3.20}$$

The location estimate for the empirical model differed significantly from the preceding developments in that h could not be estimated independently from I_{min}. As discussed

in Section 3.6, an upper bound estimate for h, defined as h_{max}, was made by setting I_{min} to zero.

To plot thresholds versus distance, the displacement s on the retinal surface was calculated for each electrode by substituting b and c (estimated for each fiber) and x_o and z_o (defined for each electrode) into equation 3.9. The total displacement D could also be calculated from s and the estimated h, according to equation 3.10. Estimates for h were more strongly dependent on the choice of model than b and c, however (see Section 3.5.3), so s was used instead of D.

3.4 Results

3.4.1 Monopolar threshold vs. distance

Monopolar threshold maps were made for nine fibers in seven retinas. Individual threshold vs. displacement plots for the nine fibers, with best-fit curves for each, are shown in Figure 3.5 for the first principles model, and in Figure 3.6 for the empirical model.

The curves in Figures 3.5 and 3.6 were obtained by computing I_{thr} from equations 3.12 and 3.22, respectively, using the best-fit parameters a_1–a_4 for each fiber, at points (x_o, z_o) along a line perpendicular to the fiber. Error terms, also shown in each of the nine plots in each Figure, were obtained from

$$e = \sqrt{\frac{\Sigma_{i=1}^{N} \left(y_i - y_p(s_i)\right)^2}{N}}$$

where e is the error, N is the number of thresholds measured, y_i is the ith threshold measurement, s_i is the inferred distance on the retinal surface between the ith electrode and the fiber, and $y_p(s_i)$ is the theoretical prediction for the threshold at a displacement s_i.

Table 3.1 summarizes the results from the fiber position estimates using the first principles model. The estimates exhibit a range of nonzero tilt angles. This is due to imperfect alignment of retina patches on the array. Hence the bipolar measurements were approximately but not strictly parallel and perpendicular to the fibers. The range of x-intercept values simply indicates that fibers were studied at various horizontal displacements on the array. The h and k estimates and the error e will be considered in Section 3.5.3. Table 3.2 summarizes the same data for the empirical model.

The differences in tilt angles, x-intercepts, heights, and errors obtained with the two models are summarized in Table 3.3. The differences in tilt angles and x-intercepts are quite small when compared with the range of tilt angles observed and with the spacing between bipolar stimulating electrode pairs. The estimated heights of the fibers above the array were always higher for the first principles model than for the

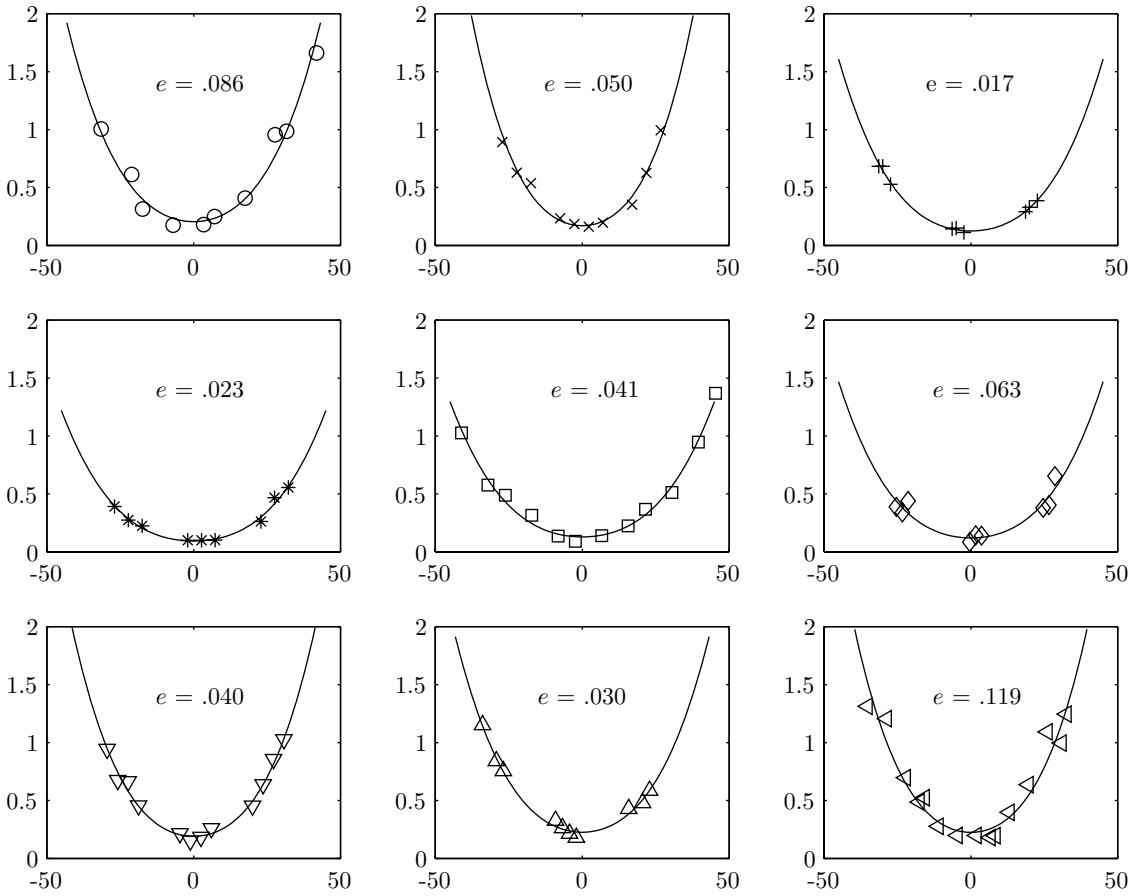

Figure 3.5: Measured data (symbols) and best-fit theoretical curves (first principles model) for monopolar threshold (vertical axes, in μA) vs. inferred displacement (horizontal axes, in μm) on the retinal surface, for each of nine fibers. Displacements were inferred using the first principles model. Negative displacements indicate stimulation on the left side of the fiber; positive displacements indicate stimulation on the right side of the fiber. An error term e, described in the text, is also given for each curve fit.

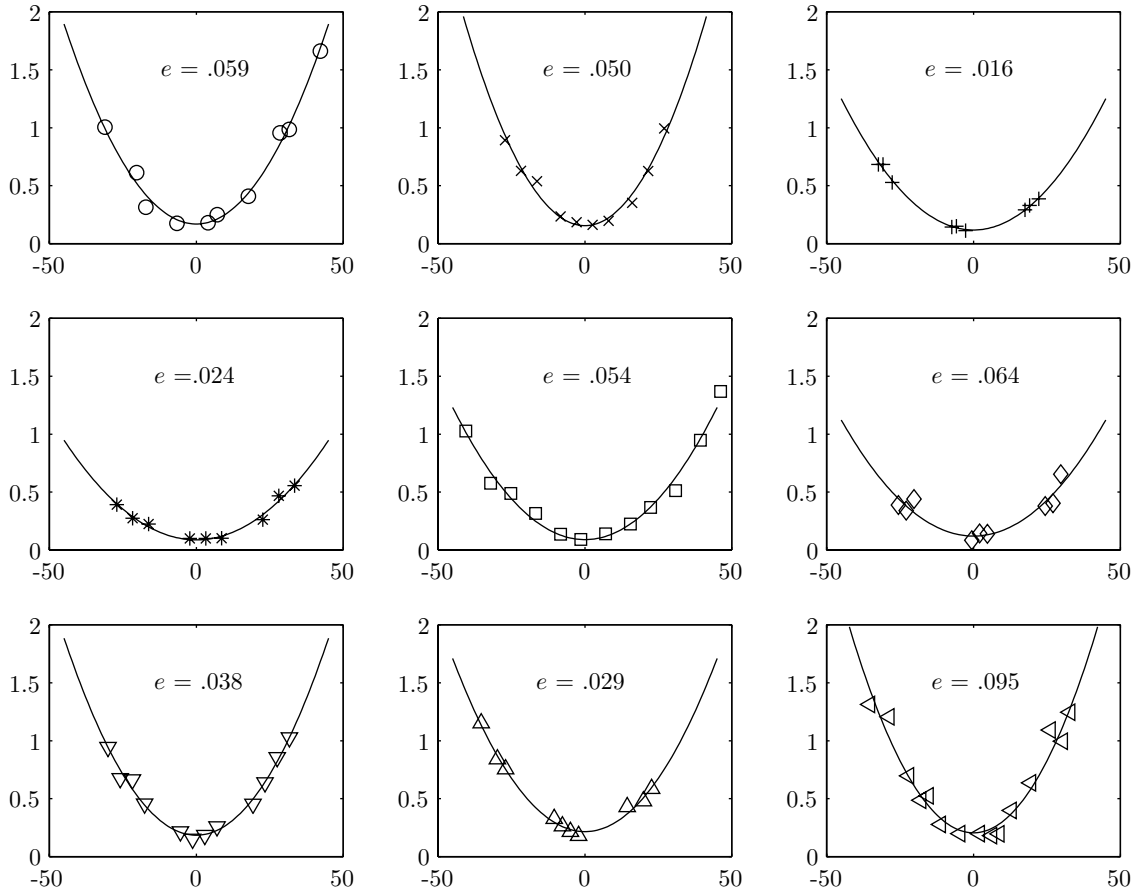

Figure 3.6: Measured data (symbols) and best-fit theoretical curves (solid lines) for monopolar threshold (vertical axes, in μA) vs. inferred displacement (horizontal axes, in μm) on the retinal surface, for each of nine fibers. Displacements were inferred using the empirical model. Negative displacements indicate stimulation on the left side of the fiber; positive displacements indicate stimulation on the right side of the fiber. An error term e, described in the text, is also given for each curve fit.

	Mean	Range
Tilt Angle	-5.2°	-17.3° to 8.2°
x-intercept	47.4μm	15.3 to 101μm
h	21.9μm	18.6 to 24.3μm
k	$1.6\times10^4\mu$A/mm^3	1 to $2.7\times10^4\mu$A/mm^3
e	.052μA	.017 to .119μA

Table 3.1: Curve fit statistics for fiber position estimates using the first principles model. The tilt angle was found by taking the inverse tangent of $-b$, and measures the fiber's angular deviation from vertical. The x-intercept, $-c$, indicates the horizontal displacement of the fibers along the top row of the stimulating grid.

	Mean	Range
Tilt Angle	-5.3°	-17.9° to 9.5°
x-intercept	47.5μm	13.7 to 101μm
h_{max}	14.4μm	12.1 to 17.1μm
$\hat{k}$	724μA/mm^2	424 to 1055μA/mm^2
e	.048μA	.016 to .095μA

Table 3.2: Curve fit statistics for fiber position estimates using the empirical model.

	Mean	Range
ΔTilt Angle	.2°	-1.3° to 1.3°
Δx-intercept	-.1μm	-1.4 to 1.6μm
Δh	7.5μm	6.1 to 10.9μm
Δe	.004μA	-.013 to .027μA

Table 3.3: Comparison of curve fit parameters for the first principles and empirical models. The table entries each represent a mean or range of nine Δs (one per fiber) each of which was computed by subtracting the empirical model estimate from the first principles estimate.

empirical model. The mean height difference was a substantial fraction of the mean height predicted by either model. This fraction was about 30% for the first principles model and about 50% for the empirical model. The goodness of fit is marginally better for the empirical model, as indicated by the small, positive Δe. A meaningful comparison cannot be made between the current-distance constants k and $\hat{k}$, since these have different units.

Figure 3.7 shows a summary plot of thresholds vs. s, the estimated electrode displacement on the retinal surface, for all nine fibers. Thresholds ranged from .1 to .2μA nearest the fiber and rose with displacement. Displacements were estimated in the Figure using the first principles model. The comparable plot for the empirical model (not shown) is nearly identical due to the close agreement in tilt angles and x-intercepts for the two models (Table 3.3).

3.4.2 Bipolar threshold vs. orientation

Bipolar thresholds were measured for five fibers in five retinas. Figures 3.8 and 3.9 plot the thresholds for stimulation along and across fibers as a function of the surface distance s from the fixed electrode to the fiber, where s was estimated using the first principles model and empirical model, respectively. Each symbol in these plots represents the ratio of a bipolar threshold to the monopolar threshold measured on the corresponding fixed electrode. The data in the two plots exhibit the same general trends. The along threshold ratios do not vary significantly with displacement, remaining close to one. The across threshold ratios, on the other hand, are close to one when the fiber is near the fixed electrode and rise rapidly for fibers at increasing proximity to the midpoint between the two poles ($s = 25\mu$m).

Theoretical predictions for the threshold ratios are also shown in Figures 3.8 and 3.9. These predictions were generated by extending the models for monopolar stimulation to the bipolar case, as described in Section 3.2.1 for the first principles

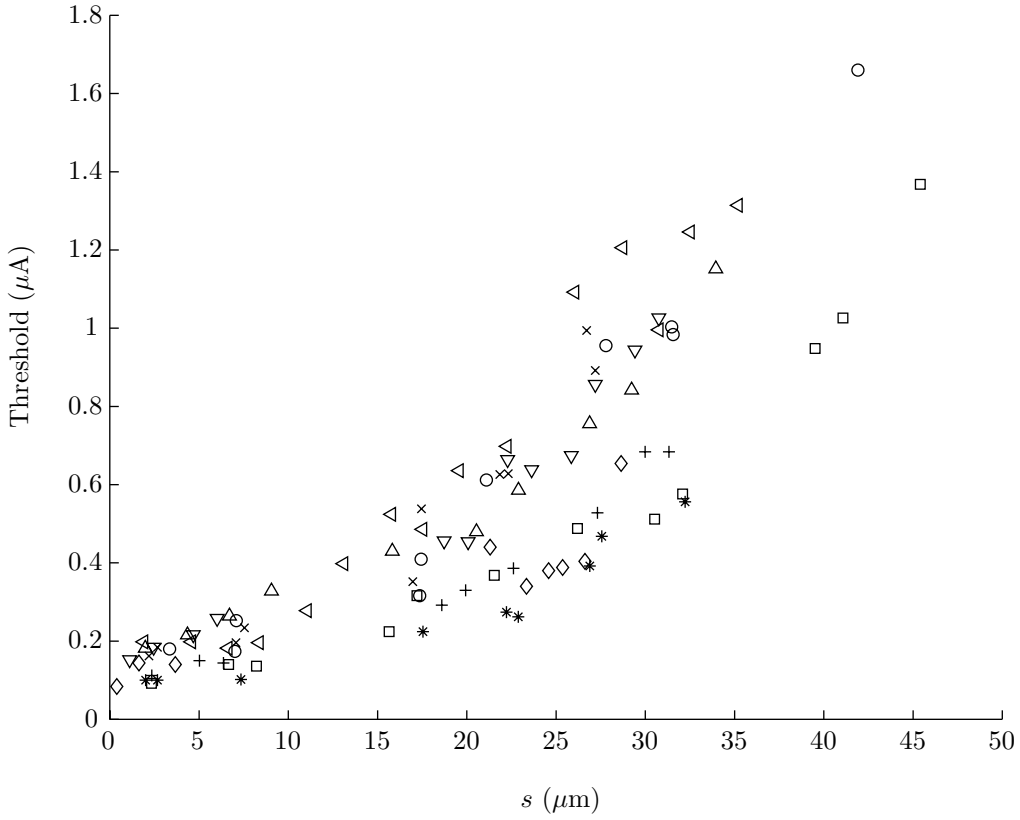

Figure 3.7: Monopolar threshold vs. inferred displacement s on the retinal surface (estimated using first principles model). Data from each cell is plotted with a unique symbol.

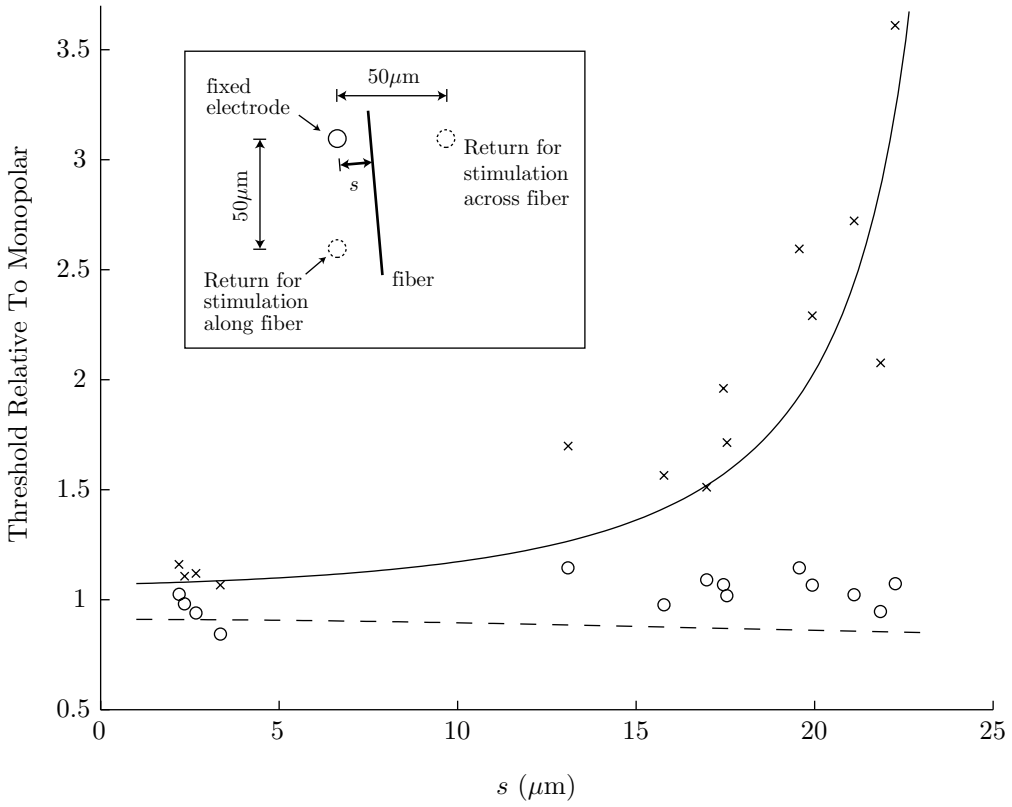

Figure 3.8: Normalized bipolar thresholds vs. inferred displacement s on the retinal surface (estimated using the first principles model), with theoretical curves superimposed. A $\times$ is used for thresholds measured with the bipolar electrode pair oriented across the fiber, and a $\circ$ when the pair was oriented along the fiber. Normalization was carried out by dividing each bipolar threshold by the monopolar threshold measured on the fixed electrode. Threshold predictions for stimulation along fibers are indicated with a dashed line, and predictions for stimulation across fibers are indicated with a solid line.

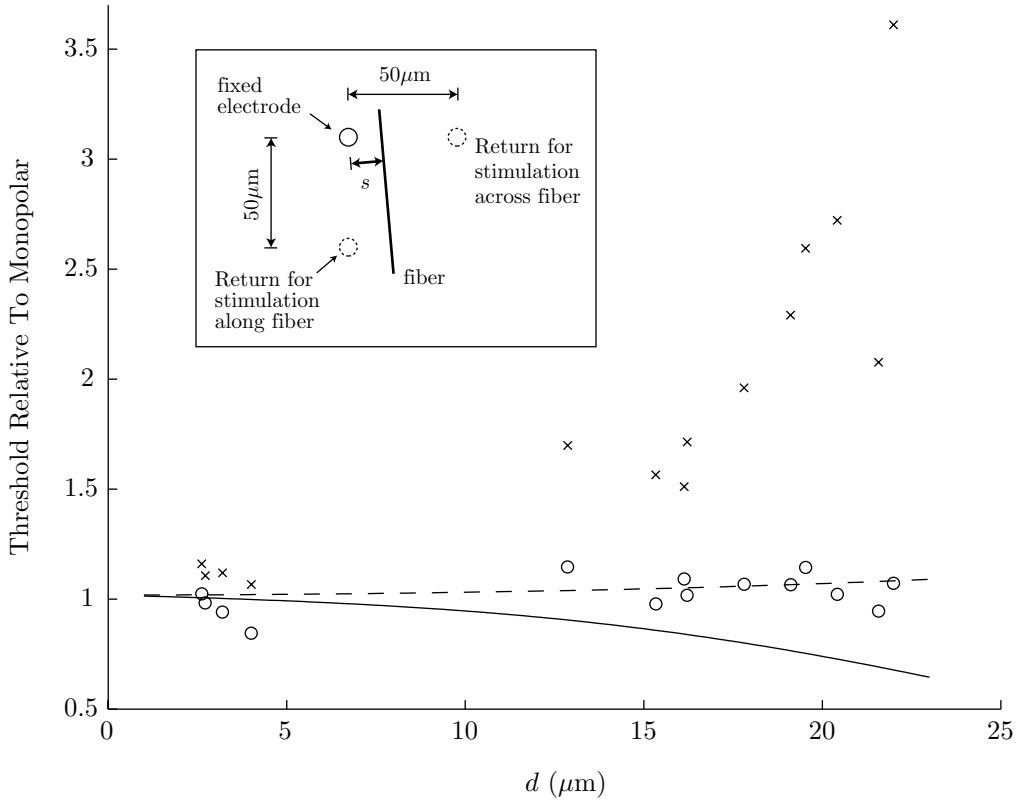

Figure 3.9: Normalized bipolar thresholds vs. inferred displacement s on the retinal surface (estimated using the empirical model), with theoretical curves superimposed. A $\times$ is used for thresholds measured with the bipolar electrode pair oriented across the fiber, and a $\circ$ when the pair was oriented along the fiber. Normalization was carried out by dividing each bipolar threshold to the monopolar threshold measured on the fixed electrode. Threshold predictions for stimulation along fibers are indicated with a dashed line, and predictions for stimulation across fibers are indicated with a solid line.

model and in Section 3.2.2 for the empirical model. The curves for stimulation along (dashed line) and across (solid line) fibers were produced by normalizing the bipolar threshold predictions for each model to its corresponding monopolar threshold prediction, assuming $h = 21.9\mu$m for the first principles model and $h = 14.4\mu$m for the empirical model (i.e. the mean values from the location estimates, given in Tables 3.1 and 3.2), and identifying $x_o = s$ and $d = 50\mu$m. While both models reasonably predicted thresholds for stimulation along fibers, only the first principles model provided a good prediction for stimulation across fibers.

The fixed electrode served as a general reference for the threshold comparisons in Figures 3.8 and 3.9: its position was used to determine the displacement s, and its monopolar threshold was used to normalize the bipolar thresholds. As described in Section 3.3.1, the fixed electrode was chosen so that it always had the lowest monopolar threshold of the three electrodes used to make the paired along/across measurements (see inset of Figure 3.8 or 3.9). This lowest-threshold electrode was used as a reference because it played the dominant role in excitation when used with a second, more distant electrode for bipolar stimulation. This dominance was indicated by a few experiments in which the sequence of anodal and cathodal pulses was reversed by either inverting the stimulation waveform or reversing the stimulator connections. In all cases, spike responses to threshold-level stimuli tracked the stimulus phase which drove the fixed electrode cathodically. Since cathodic thresholds are lower than anodic thresholds for monopolar stimuli (see Section 2.5.2), this behavior is consistent with localized excitation near the fixed electrode.

The preceding developments motivated the choice of stimulus sequence in Figure 3.3d. While thresholds were identical for both stimulus sequences, better separation of the responses from artifacts was achieved by driving the fixed (+) electrode cathodically for the second phase. Since the cathodic phase was responsible for excitation, this sequence ensured that responses were almost always recorded after the end of the stimulus. There were a few cases were suprathreshold stimuli evoked spikes which randomly followed either the first and second phase of the stimulus. In these cases the fiber was at very nearly the same distance from both poles of the bipolar pair (e.g. the fiber was near $s = 25\mu$m for across stimulation). Hence neither electrode played a dominant role. All spikes generated under such circumstances were counted—regardless of which stimulus phase they followed—when determining the threshold.

3.5 Discussion

3.5.1 Monopolar stimulation

Threshold order of magnitude

At points closest to the fibers, monopolar excitation thresholds ranged from approximately .1 to .2μA for a 400μs stimulus phase duration. Table 3.4 compares this result with thresholds reported by others who placed stimulating electrodes against the epi-retinal surface.

The reported threshold currents span a range of over three orders of magnitude, with the threshold currents in this study falling about a factor of five below the lowest threshold reported previously. Some of the variability can be accounted for by differences in stimulation parameters. Threshold currents are modestly correlated with electrode area, for example. Electrode areas were less than 10^{-6}cm^2 in the three cases where threshold currents were below a microampere, and greater than 10^{-6}cm^2 for larger threshold currents. Expressing thresholds as average current densities (threshold $\div$ area)* reduces the variability by an order of magnitude. These results are not surprising since a simple electric field calculation shows that, near the surface of a spherical stimulating electrode, the current required to produce a given voltage gradient increases with electrode radius (Ranck, 1981)†. Since phase durations were not all the same, some of the variability in the current and current density thresholds might be accounted for by classic strength-duration behavior. In the three studies reporting sub-microampere threshold currents, for example, the total charge (current $\times$ phase duration) varied by less than a factor of two despite a five- to six-fold variation in threshold current. Expressing thresholds as an average charge density (charge $\div$ area)†, which takes into account both the phase duration and the electrode area, results in less variability than the currents but slightly larger variability than the current densities. The remaining variability might be accounted for by a number of methodological differences, including the electrode shape, the species studied, or the site of initial excitation within the retina.

Although the threshold currents reported in this study are quite low when compared with other retinal stimulation experiments, these were not unusually low when expressed as average current densities and average charge densities. Furthermore, comparably low current thresholds for extracellular stimulation have appeared in

*Note that the average current and charge densities may not represent the actual distribution of current and charge in real electrodes, since stimulating electric fields are not necessarily uniform across electrode surfaces In addition, some caution is in order when using current and charge densities, since both will tend to rise without limit as the electrode area approaches zero, and the charge density will rise without limit for stimulus phase durations well above chronaxie.

†Ranck calculated the current needed to cause a 30mV difference in voltage between a site just adjacent to the electrode and another site 600μm away. For electrode radii between 1μm and 100μm, this current appeared to scale with electrode radius. In the limit where the radius becomes very large compared to 600μm, the requisite current is proportional to the square of the radius.

Study	Threshold current	Electrode area	Current density	Phase duration	Phase charge	Charge density
Dawson & Radtke (1977)	65μA	4.91×10^{-6} to 7.90×10^{-4}cm^2		800μs		30.5μC/cm^2
Greenberg (1998c)	206μA	1.26×10^{-3}cm^2	163mA/cm^2	520μs	1.07×10^{-7}C	85μC/cm^2
Humayun et al. (1994)	50μA (frog)	1.26×10^{-3}cm^2	40mA/cm^2	75μs	3.75×10^{-9}C	2.98μC/cm^2
	150μA (rabbit)	1.26×10^{-3}cm^2	119mA/cm^2	75μs	11.2×10^{-9}C	8.92μC/cm^2
	200μA (rd rabbit)	1.26×10^{-3}cm^2	159mA/cm^2	75μs	15×10^{-9}C	11.9μC/cm^2
Humayun et al. (1999)	(phosphenes)	1.26×10^{-3}cm^2 (array)		$\leq$2ms	5×10^{-7}C	397μC/cm^2
Jensen et al. (1996)	8μA	7.8×10^{-5}cm^2 (bipolar)	102mA/cm^2	200μs	1.6×10^{-9}C	20μC/cm^2
(near soma)	.8μA	1.6×10^{-7}cm^2 (monopolar)	5000mA/cm^2	100μs	8×10^{-11}C	500μC/cm^2
Rizzo et al. (1997)	16μA	7.8×10^{-5}cm^2 (bipolar)	205mA/cm^2	200μs	3.2×10^{-9}C	41μC/cm^2
(axon)	.9μA	1.6×10^{-7}cm^2 (monopolar)	5625mA/cm^2	100μs	9×10^{-11}C	562μC/cm^2
This study	.15μA	7.8×10^{-7}cm^2	192mA/cm^2	400μs	6×10^{-11}C	77μC/cm^2

Table 3.4: Summary of thresholds for stimulation at the epi-retinal surface. Entries were left blank where relevant information could not be determined. For studies where a range of thresholds was reported rather than a mean or median, the table entries represent the average of the minimum and maximum values reported. For studies where thresholds were reported at various positions of the stimulating electrode, the table data represent measurements at the lowest-threshold position. And for studies where both anodal and cathodal monopolar stimuli were used, the table data represent cathodal thresholds only. Doty & Grimm (1962) also placed stimulating electrodes the epi-retinal surface (see Table 1.1), but reported thresholds in terms of voltage rather than current and did not report the electrode area. *Abbreviations:* rd = retinal degenerate (experimentally induced).

previous studies of other neural systems (Ranck, 1975).

Spatial extent of stimulation

The spatial extent of fiber excitation for a given stimulus amplitude may be estimated from the plot of Figure 3.7 by superimposing a horizontal line at the desired level and finding its intercept with the data. A .2μA stimulus, for example, would be expected to excite fibers within about 10μm of the of the stimulating electrode since thresholds were higher at larger distances. Similarly, a 1μA stimulus will excite fibers within 40μm of the electrode. Such estimates are somewhat simplistic, however, because they fail to take into account the fact that cathodal pulses far above threshold can fail to generate propagated action potentials (Ranck, 1975). This effect is caused by hyperpolarization in regions where stimulation currents enter the fiber, away from the cathode. Hence for sufficiently large cathodal currents there will be a central region of non-stimulated fibers surrounded by an annular, stimulated region. No attempts were made in the present study to detect or characterize this phenomenon.

The rise of thresholds with electrode displacement away from the target has been studied elsewhere. Rizzo et al. (1997) measured axon excitation thresholds vs. stimulating electrode position in rabbit retina using three different stimulation protocols. For the protocol most resembling the present experiments (Protocol II), median thresholds rose by a factor of six when the electrode was displaced to $s = 50\mu$m[‡]. Greenberg (1998c) measured excitation thresholds for ganglion cells in frog retina, and found that displacements of several hundred microns were required for a 1.4-fold (i.e. 3dB) increase in threshold. Stimulation in the present study was somewhat more focal than in the previous two cases, since thresholds rose by roughly a factor of ten at a distance of 40μm. The current-distance constants k and $\hat{k}$ in Tables 3.1 and 3.2 also measure the spatial extent of stimulation. The range of values listed for $\hat{k}$ is similar to those found in other neural systems (Tehovnik, 1996).

3.5.2 Orientation dependence

Figures 3.8 and 3.9 show that fiber excitation thresholds were sensitive to the orientation of the stimulating electric field. Thresholds for each fiber were highest when the stimulating field was most nearly perpendicular to its long axis, achieved in practice when the fiber was most nearly at the midpoint between the two poles used for transverse bipolar stimulation. When the fiber was within 5μm of this midpoint, thresholds were about a factor of 2 to 3.5 larger than when monopolar or longitudinal bipolar stimulation was used.

Note, however, that even in these cases the estimated fiber paths were still 2-3μm away from the midpoint between the two poles and were often tilted with respect to

[‡]Rizzo et al. used the variable name y, rather than s, to measure distances along a line perpendicular to the axon's course.

vertical. The first principles model predicts that thresholds will become infinite as the fiber approaches this midpoint, but this is simply a consequence of one of the model's assumptions. The model assumes, as do many in the extracellular stimulation literature, that the transverse component of the stimulating field contributes negligibly to excitation (McNeal, 1976; Rattay, 1986; Rubinstein and Spelman, 1988; Warman et al., 1992). The assumption arises from the common occurrence of both transverse and longitudinal field components in the experimental literature. The transverse voltage drop across a fiber's outer surface is usually small, at least when compared to the voltage drop developed by the longitudinal component of the field, owing to the fiber's small diameter.

Such justification would not apply if the stimulating field were purely transverse. Suppose for the sake of argument that purely transverse fields were insufficient to produce excitation in fibers. In practice, one would still not expect thresholds with optimally positioned electrodes to become unbounded for at least two reasons. First, electrical inhomogeneities or anisotropies in the tissue could deflect the stimulating field to generate longitudinal field components. Second, at high enough currents other regions of the same cell or pre-synaptic elements will be stimulated. On the other hand, the most dramatic increases in threshold are expected to occur within the vary narrow, as yet unexplored gap of $\approx 3\mu$m between the best-centered data points in Figure 3.8 and the exact center at 25μm. It therefore seems reasonable that a more exhaustive study could reveal larger threshold ratios in a narrow band at the center of the bipolar electrode pair.

3.5.3 Models

Monopolar stimulation and location estimates

Both the first principles and empirical models provided provided a good fit to the data. The goodness of fit, as measured by the error term e, was similar for the two models. The mean error was marginally larger for the first principles model than for the empirical model (see Tables 3.1 and 3.2). In both cases, this mean error was at least a factor of two smaller than the lowest thresholds observed. The best-fit curves for the two models were nearly identical, as could be verified by overlaying the plots in Figures 3.5 and 3.6. The largest differences were seen near $\pm 50\mu$m, where the curves for the first principles model sometimes rose more steeply than those for the empirical model. A more competitive comparison of the two models would likely be possible if threshold data were available for a larger range of electrode displacements.

The two models differed significantly in their estimates for the fibers' heights h above the array (Table 3.3). On average, the upper bound height h_{max} predicted by the empirical model was 7.5μm less than the height predicted by the first principles model. This discrepancy is simply a consequence of the difference in steepness of the threshold vs. electrode-fiber distance curves in the two models. The steeper first principles model predicts a larger height because this results in a slower increase of

total distance—and hence a slower increase of predicted thresholds—with increasing surface distance (the independent variable in the monopolar threshold maps).

Estimates for the fibers' projections onto the electrode array plane, described by the tilt angle and $x-$intercept (or equivalently by b and c), were more certain. The two models provided nearly identical estimates for these projections. Furthermore, whole-mount stains from other studies (Peichl et al., 1987; Vaney, 1980) show that in small regions away from somata such as that spanned by the stimulating cluster in Figure 2.2, it is very reasonable to assume that axons follow straight-line paths. A possible weakness in the model is the assumption that fibers run at a constant height above the array. Hence errors could be introduced into the tilt angle and x-intercept estimates if threshold variations across the maps were partially due to height variations. This possibility was explored by assigning an out-of-plane slope r to the fiber such that

$$h = h_o + rz$$

and re-estimating the parameters b, c, h_o, and k using the first principles model. For an r-range corresponding to an out-of-plane slope of -5° to 5° (or a height difference of over 10μm across the 125μm span of the array), the in-plane tilt angle varied by no more than 3.3° and the x-intercept varied by less than 2μm[§]. Hence the location estimates were not substantially changed when height of the fiber was allowed to vary. Because the actual height of the fibers above the array was uncertain, the surface displacement s was used in the threshold plots rather than the total displacement D.

The accuracy of the fiber position estimates might be improved by imaging retinas during experiments. This approach was not attempted in the present study, primarily because optical access was impeded from above by the dialysis membrane holding the patch in place, and below by the opaque chrome/gold electrode conductors. The latter problem can be remedied by using indium tin oxide (Meister et al., 1994), a transparent conductor, instead of chrome/gold. The large number and complex arrangement of neural elements could also make it difficult to correctly identify the precise fiber under study. Conducting studies in peripheral retina should increase the chances of uniquely identifying the axon under study.

Bipolar thresholds

While both models reasonably predicted thresholds for stimulation along fibers, only the first principles model provided a good prediction for stimulation across fibers (Figures 3.8 and 3.9). Predicted thresholds fell with increasing s in the empirical model because the maximum field magnitude *was larger* between the two poles of transverse bipolar pair than at a comparable distance from a monopolar electrode, even though the longitudinal component of the field was reduced. Since the physi-

[§]At larger out-of-plane slopes, the software routine used for least-squares estimation—MATLAB's `nlinfit` function—either converged to non-real (i.e. complex) values or did not converge at all.

ologic thresholds rose for transverse bipolar stimulation, electric field strength alone does not accurately predict fiber excitation thresholds.

Use of the activating function

The first principles model made a number of assumptions in order to permit a purely theoretical formulation. For example, the activating function rather than the membrane potential was used to gauge thresholds. Because it ignores the distribution of stimulating currents in the fiber, the activating function only approximates the membrane potential profile generated by a stimulus (Warman et al., 1992). The main advantage of this approach is that it eliminated the need to model membrane electrical properties, which are nonlinear and would have required computer simulation.

3.5.4 Axons or dendrites?

The possibility was raised in Chapter 2 that some or all of the recorded responses might be due to stimulation of dendrites rather than axons. Hence the use of the more general term *fiber*. Since both axons and dendrites share the same basic cylindrical geometry, the identity of the target little effects the primary result of this Chapter. However, it seems reasonable to suggest that responses were due at least in part, if not in total, to stimulation of axons. The dendrites stratify in the inner plexiform layer, several tens of microns further than axons from the stimulating electrode plane. The very lowest excitation thresholds would therefore be expected for axon excitation. Furthermore, the magnitude of current necessary for stimulating axons could be judged from the minimum amplitude which produced graded potentials. These magnitudes were not systematically lower than the spike thresholds, as would be expected if spikes arose only as a result of dendrite stimulation.

The height estimates yielded by the first principles and empirical models are consistent with stimulation of elements near the retinal surface, but do not conclusively identify the stimulation target. The empirical model yielded an upper bound h_{max} on the fiber height of 17.1μm or less. Assuming that the arrays were in direct contact with the inner limiting membrane (ILM), this range of heights could be consistent with with either axon or dendrite stimulation. The first principles model yielded height estimates of 18.6μm or more. For arrays in direct contact with the ILM, this range of heights would not be consistent with axon stimulation because the nerve fiber layer is only about 10μm thick in the retinal regions where these studies were conducted. On the other hand, it is likely that the model over-estimated the heights, since at the same current a 10μm diameter electrode would have to be closer to its target than a point source in order to generate an equally strong activating function. It is also possible that the electrode arrays were not in direct contact with the ILM, but separated from it by a thin layer of vitreous. Hence the height estimates from the first principles model do not rule out axon stimulation.

A more definitive statement about the stimulation target could be made if the stimulating and recording clusters were placed further apart than the largest dendritic spreads, perhaps 1mm or more. In the present experiments the cluster separation was kept small to reduce the sensitivity of the measurement to imperfect vertical alignment of axons. At larger separations, the chances of recording from a cell whose axon ran through the stimulating cluster would be reduced.

3.6 Appendix: Location estimates using the empirical model

Equation 3.5 was used to estimate fiber locations in a manner analogous to that described in Section 3.3.2. Threshold map data are incorporated into this model according to

$$I_{thr} = \hat{k}\left\{\frac{(x_o + bz_o + c)^2}{1+b^2} + h^2\right\} + I_{min}. \tag{3.21}$$

(see Section 3.3.2 and Figure 3.4 for descriptions of the variable definitions).

The parameters b, c, and $\hat{k}$ were estimated by re-writing this relation as

$$I_{thr} = a_1 x_o^2 + a_2 x_o + a_3 + a_4 x_o z_o + \left(\frac{1}{2}\frac{a_2 a_4}{a_1}\right) z_o + \left(\frac{1}{4}\frac{a_4^2}{a_1}\right) z_o^2, \tag{3.22}$$

where

$$a_1 = \frac{\hat{k}}{1+b^2}, \tag{3.23}$$

$$a_2 = \left(\frac{\hat{k}}{1+b^2}\right)(2c), \tag{3.24}$$

$$a_3 = \hat{k}\left(\frac{c^2}{1+b^2} + h^2\right) + I_{min}, \tag{3.25}$$

$$a_4 = \left(\frac{\hat{k}}{1+b^2}\right)(2b). \tag{3.26}$$

Performing a nonlinear least-squares fit yields parameters a_1, a_2, a_3, and a_4 which best satisfied equation 3.22 for each threshold map.

Estimates for each cell's b, c and $\hat{k}$ were then calculated as follows:

$$b = \frac{a_4}{2a_1}, \tag{3.27}$$

$$c = \frac{a_2}{2a_1}, \tag{3.28}$$

$$\hat{k} = a_1(1+b^2). \tag{3.29}$$

The parameters h and I_{min} could not be estimated independently because these contributed only additive terms to the threshold maps. However, a maximum bound on h could be estimated by assuming $I_{min} = 0$. The upper bound, h_{max}, was given by

$$h_{max} = \sqrt{\frac{a_3}{\hat{k}} - \frac{c^2}{1 + b^2}}.$$

Chapter 4

Conclusions

4.1 Strengths and weaknesses of new experimental method

A significant proportion of the effort in this thesis was aimed at the development of new techniques for characterization of retinal responses to electric stimulation. It is useful at this point to consider the advantages and disadvantages of these techniques.

4.1.1 Stimulating electrode arrays

The main strength of the new experimental setup was its use of microfabricated stimulating electrode arrays. With these arrays it was a simple matter to quickly perform a number of threshold measurements with a number of electrode configurations, all without any mechanical disruption of the retina preparation. Furthermore, arrays provide the experimenter with detailed control over the shape and distribution of electrodes. Though in this study conventional disk shapes of a uniform size were used, future work is likely to benefit from more complex and unconventional electrode arrays (see Chapter 5).

A possible drawback of the stimulating array approach is that unused electrodes on the array can play a role in shaping the stimulating electric field distribution*. The exposed metal electrode surfaces are equipotentials in the frequency ranges of interest to electrophysiologic studies, and will tend to equalize tissue potentials in their immediate vicinity. The extent of field distortion from unused electrodes will depend on the relative sizes of the tissue impedance and electrode interface impedances. Such distortion needs to be taken into account in particular when considering experiments with large, closely-spaced electrodes, as discussed in Section 5.4.

*This was first pointed out to me by a member of my thesis committee, Don Eddington.

4.1.2 Recording arrays

Multi-electrode recording systems permit simultaneous monitoring of activity at many sites in a tissue. In the measurements described in Chapters 2 and 3, this capability was utilized to record correlated spontaneous firing, which in turn suggested the anatomical substrates underlying different spike waveforms (see Figure 2.6 and Section 2.6), and to speed up the search for sites within the recording cluster exhibiting single unit responses to electric stimulation. Multi-channel recordings were not employed for the mapping and orientation measurements, though in principle they could be. For such an approach it would be useful to have an automated system for determining excitation thresholds, which in turn would require a means of discriminating all-or-none responses from graded responses and stimulus artifacts.

The main drawback of the new method is that each recording electrode tends to pick up multiple units. Hence the ubiquitous graded potentials, which required a tedious search for sites with clean all-or-none potentials for stimulation at a number of different stimulating electrode positions. With its smaller tip diameter and ability to penetrate the surface, a needle-shaped recording electrode provides better isolation of single units. On the other hand, this geometry does not lend itself as easily to multi-electrode studies (but see Normann, 1999).

4.1.3 Soma stimulation

The setup did not lend itself well to measuring thresholds for excitation of somas and associated structures (i.e. the axon hillock and initial segment). Such experiments are most easily performed by applying stimuli in the vicinity of a ganglion cell's optic receptive field center and recording the orthodromic responses at a location along the cell's axon. In the present setup, axon spikes (Type 2 in Figure 2.6) were usually smaller and more difficult to discriminate than the soma spikes (Type 1). Early attempts were made to both stimulate and record from the soma by stimulating through electrodes which were very close to a recording electrode with Type 1 spikes, but stimulus artifacts always obscured at least the first 3-5ms of the response. While difficult for flat recording electrodes, soma threshold measurements can be more readily made with needle-shaped recording electrodes which better isolate single axons.

4.2 Related work re-considered

Chapter 3 demonstrated that thresholds for retinal ganglion cell axons (and possibly dendrites) depended in a consistent manner on the orientation of a bipolar stimulating electrode. Thresholds were highest when the imposed electric field was most nearly perpendicular to fibers, achieved in practice when the fiber was near the midpoint between the two poles of a transversely oriented bipolar electrode pair. This result

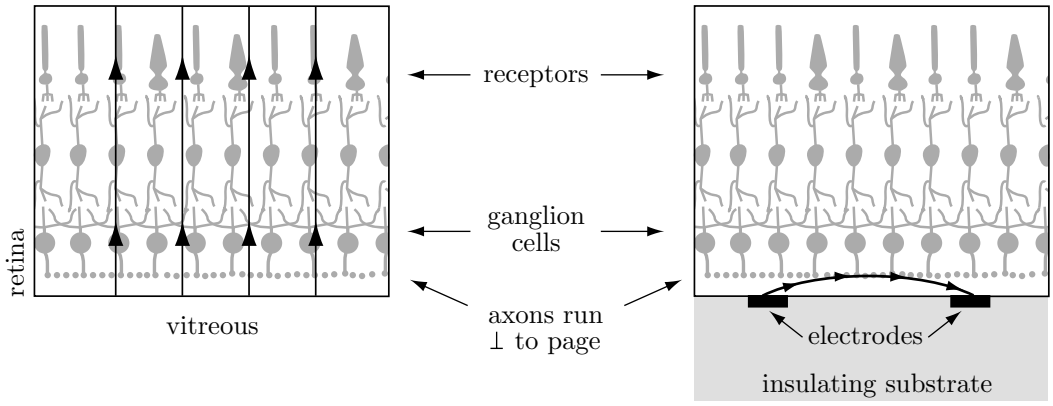

Figure 4.1: Both transretinal (left) and transverse bipolar (right) stimulation produce stimulating fields which run perpendicularly to axons.

is consistent with theoretical predictions (Plonsey and Altman, 1988; Grumet, 1994) and experimental work in other neural systems (Ranck, 1975; Rushton, 1927).

This result also indicates that axon thresholds will be comparatively high for transretinal current (Figure 4.1, left hand side). Like the current from a carefully placed transverse bipolar electrode pair (Figure 4.1, right hand side), transretinal current runs perpendicularly to ganglion cell axons. Furthermore, initial excitation of deeper elements such as photoreceptors and bipolar cells is perhaps more likely under these conditions (Greenberg, 1998a). Except in regions of high receptor density, a number of receptor and bipolar cells will converge on each ganglion cell. Because the ganglion cell can spatially integrate synaptic contributions to its membrane potential from many bipolar cells—each of which can integrate contributions from many photoreceptors—weak stimulation of a population of pre-synaptic cells could conceivably result in ganglion cell spiking at current levels below the threshold for direct ganglion cell stimulation.

In the majority of the studies listed in Table 1.1, stimulating electrodes were placed at a considerable distance (500μm or more) from the epi-retinal surface. It seems likely that in many such cases the fields were either stronger in other parts of the retina than at the epi-retinal surface, or were predominantly transretinal. In two studies, electrodes were placed outside the eye, against the sclera (Brindley, 1955; Greenberg, 1998a). Reponse characteristics in these studies were consistent with stimulation by the transretinal component of the field. If the stimulating fields were not purely transretinal, they would have been strongest in regions closer to the

electrode such as the photoreceptor or bipolar cell layers. In other studies, stimulation current was passed between a monopolar electrode in the vitreous and a distant, extra-ocular return (Crapper and Noell, 1963; Humayun et al., 1996; Humayun et al., 1999). The low resistivity of the vitreous relative to that of the retina, choroid and sclera (Ogden and Ito, 1971; Rodieck, 1973) probably reduced voltage gradients in the retinal plane—and hence, along axons—so that most of the field ran perpendicularly to the retina. These observations may account for the fact that axons were not maximally sensitive to electric stimulation in many of the studies in Table 1.1.

In a retinal prosthesis the stimulating electrodes must be placed at the retinal surface to keep the excitation thresholds as low as possible. Even when monopolar configurations were used, thresholds rose rapidly with distance as the stimulating electrode was raised above the epi-retinal surface (Humayun et al., 1999; Jensen et al., 1996). Electrodes placed against the epi-retinal surface will produce the largest voltage gradients in the adjacent nerve fiber layer. This effect will be especially pronounced when electrodes reside on a planar, insulating substrate since in this case shunt paths through the vitreous will not be available. Hence axons are particularly likely to be stimulated by the electrode configuration which will be used by a retinal prosthesis.

Stimulating electrodes were placed at the retinal surface in only four of the studies permitting threshold comparisons for axons and other elements (Doty and Grimm, 1962; Greenberg, 1998c; Humayun et al., 1999; Jensen et al., 1996), and were mounted on insulating backplanes in only two (Greenberg, 1998c; Humayun et al., 1999). The results were mixed, with axons sometimes maximally sensitive in two of the studies (Greenberg, 1998c; Jensen et al., 1996), but not maximally sensitive in the other two (Doty and Grimm, 1962; Humayun et al., 1999). Differences in stimulus phase duration may partially account for this variability (see Section 1.2.3), though the pulse duration hypothesis has not yet been tested with a realistic electrode configuration (see Section 5.3). As discussed in Chapter 5, further work needs to be conducted to determine whether axon stimulation can be avoided with electrodes resembling those which will be used in an eventual prosthesis.

4.3 Implications for epi-retinal prosthesis design

Thresholds only rose for transverse bipolar stimulation when fibers were nearly centered between the two poles of the bipolar pair. When the fiber was within 5μm of either electrode, thresholds for monopolar, longitudinal bipolar, and transverse bipolar stimulation were about equal. Hence in an epi-retinal prosthesis, transverse bipolar electrodes made of 10μm diameter disks would only raise axon thresholds within narrow bands between the electrodes in each bipolar pair. Furthermore, bipolar electrodes might actually stimulate fibers over a wider area of retina than monopolar electrodes, depending on the choice of stimulation current waveform. This possibility is explained in Figure 4.2.

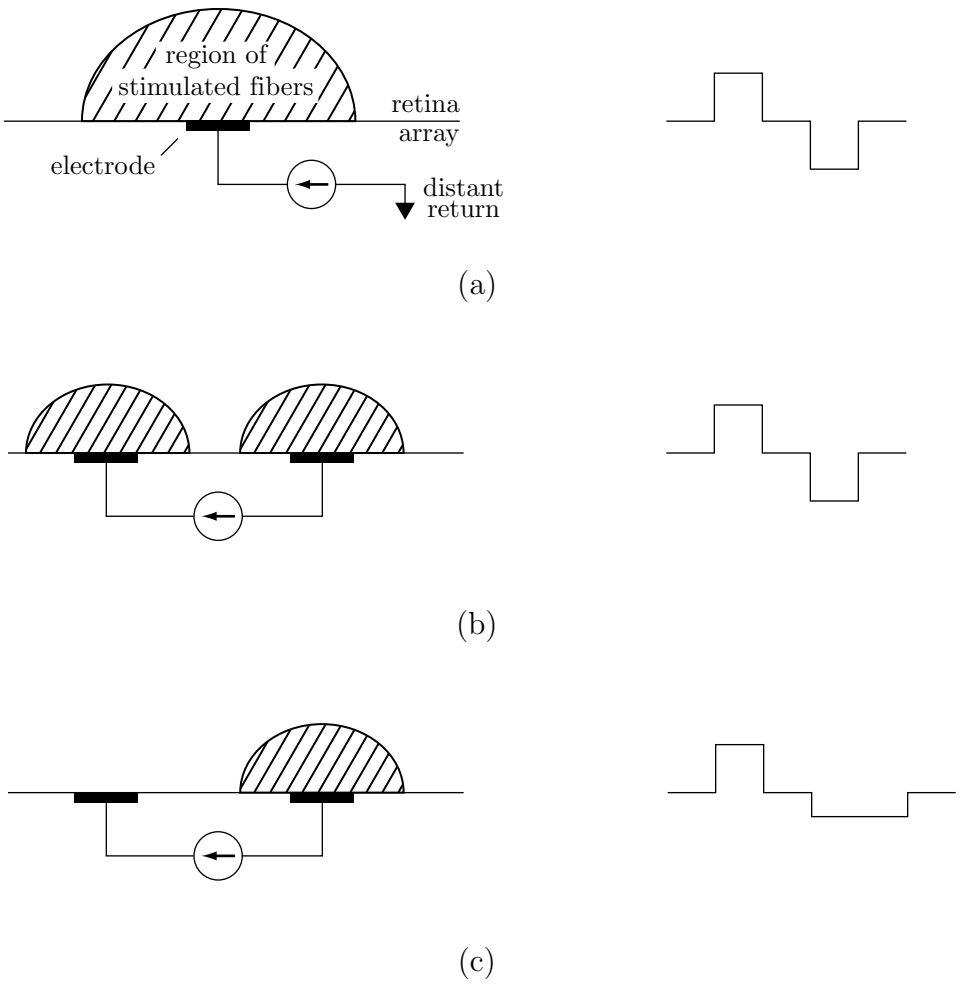

Figure 4.2: Highly schematic comparison of excitation patterns for monopolar and transverse bipolar stimulation. Left column: electrode configurations and extents of excitation; right column: stimulation current waveforms. (a) Stimulation with a monopolar electrode; (b) and (c) Stimulation with bipolar electrodes. For bipolar stimulation, the extent of excitation around each electrode will be less than for monopolar stimulation. However, for bipolar stimulation and sufficiently large stimuli, as in (b), excitation will be initiated over both poles of the bipolar pair during the corresponding cathodic phase. Excitation on one of the poles can be minimized by choosing an asymmetric stimulation waveform as in (c), provided that the waveform is charge-balanced and the longer pulse duration is well above chronaxie.

The findings in this thesis demonstrate that longitudinal fields are more efficient for stimulating axons than transverse fields. Minimizing axon stimulation therefore requires an electrode design which minimizes longitudinal field components between the poles of a bipolar electrode pair as well as in the immediate vicinity of each electrode.

Chapter 5

Future work

5.1 Refinements to the present work

As discussed in Section 3.5.4, some fraction of the measured thresholds may represent stimulation of dendrites rather than axons. Since both axons and dendrites share the same basic cylindrical geometry, the identity of the target little effects the primary result of this thesis. Still, a more definitive statement about the stimulation target could be made if the stimulating and recording clusters were placed further apart than the largest dendritic spreads, perhaps 1mm or more. In the present experiments the cluster separation was kept small to reduce the sensitivity of the measurement to imperfect vertical alignment of axons. At larger separations, the chances of recording from a cell whose axon ran through the stimulating cluster would be reduced. The experimental setup will soon be modified, however, to permit single needle recording (to better isolate cells) while stimulating through an electrode array. The modified setup should facilitate threshold measurements with large stimulating-recording electrode separations, so that the measurements described in Chapter 3 can be repeated under conditions in which dendrite stimulation would be highly unlikely.

5.2 Field direction

This thesis suggests that axon thresholds can be raised through a strategic choice of electrode geometry. Thresholds for the transverse bipolar geometry, however, were very sensitive to fiber position, only becoming substantially elevated relative to thresholds for monopolar or longitudinal bipolar stimulation when the fiber under study was well-centered between the electrode poles. Longitudinal fringing fields near the electrode poles provide the most plausible explanation for this threshold profile. Hence future *in vitro* experiments might endeavor to design novel electrode geometries with better field directionality and minimal fringing.

One candidate design inspired by previous work (Grumet, 1994) is shown in Fig-

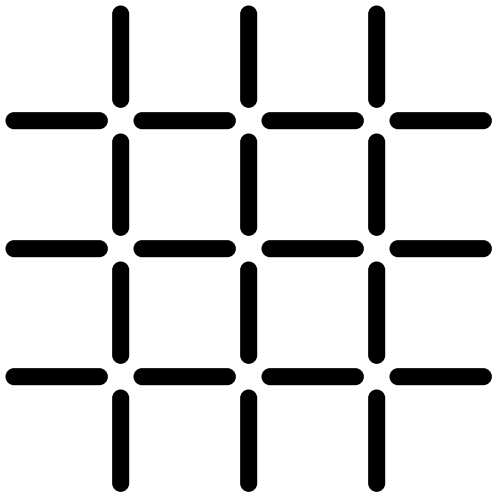

Figure 5.1: A stimulating electrode array resembling a tic tac toe board should provide better field uniformity than pairs of 10μm diameter disks for measuring thresholds versus field direction.

ure 5.1. Approximately uniform fields in the horizontal and vertical directions can be produced by connecting a stimulator across rows and columns of the array, respectively*. Longitudinal fringing fields will be a concern as before, though perhaps the elongated electrode geometry will reduce this fringing. Computer simulations or physical models might be employed to solidify qualitative notions about how much longitudinal fringing is to be expected for a particular electrode geometry.

Showing that axon thresholds depend on field orientation *suggests* a strategy for bypassing axons, but it does not *validate* this approach. Excitation thresholds for axons must ultimately be compared with thresholds for other retinal elements such as pre-synaptic cells or the ganglion cell's peri-somal region (i.e. the soma or axon hillock or initial segment) under comparable conditions. Responses originating in pre-synaptic elements can be distinguished from direct ganglion cell excitation by examining response latencies and using synaptic blockers like cadmium and APB†. To measure peri-somal thresholds, the location of the soma must first determined. This can be done coarsely by recording from the cell's axon and then probing the retina with

*Open-circuited electrodes can distort the stimulating field, as discussed in Section 4.1.1. Hence the actual field distribution may be more complex, depending on the relative sizes of the tissue and interface impedances.

†APB is an abbreviation for 2-amino-4-phosphonobutyrate, which blocks synapses in the retinal ON channel.

a spot of light to find the cell's receptive field center (Jensen et al., 1996). Further refinement of this estimate might be achieved with a tissue stain after threshold measurements are complete, provided that the cells are distributed sparsely enough that the target of stimulation can be unambiguously identified. Performing these measurements will require additional optical equipment not present in the current experimental apparatus.

5.3 Pulse duration

As discussed in Section 1.2.3, Greenberg (1998b) has found that stimulation targets depended on the duration of the stimulation pulse. However, all but one of these measurements (the phosphene experiment) were performed with 1.5mm diameter electrodes which were placed far from the epi-retinal surface. Will the same arguments apply with smaller surface-residing stimulating electrodes, where field strength will vary rapidly with retinal depth? The work of Doty and Grimm (1962) and Humayun (1999) provide some evidence to the affirmative, since these studies placed electrodes on the retinal surface and used pulse durations which were 1ms or longer, and in neither case were axons stimulated at the lowest currents. This hypothesis, however, has not yet been examined systematically with a realistic electrode configuration. Future work could also be directed at experiments to test this.

5.4 Electrode size

Table 3.4 shows that a significant range of electrode areas was used in the literature. In Section 3.5.1 I noted that the unusually small stimulating electrode size used for this thesis might account for the unusually low excitation thresholds reported in Chapters 2 and 3. Are thresholds small for small stimulating electrodes and large for large electrodes? And if so, how do the threshold versus diameter functions compare for different retinal elements? It may be that different electrode sizes stimulate different targets, in which case electrode size could be used as a tool for selectivity.

These questions can be answered experimentally using stimulating electrode array techniques. For example, a series of arrays with a range of disk diameters could be produced, with each array containing electrodes of one size. Several experiments could then be performed with each electrode size, and average thresholds compared for the different sizes. Alternatively, a range of electrode sizes could be fabricated on the same array. Measurements of the threshold versus diameter function for a particular element may prove problematic, however. On a first glance, the electrode pattern in Figure 5.2a would appear to be just the tool for the job. Using this type of pattern, thresholds could be measured with the stimulator connected between the central electrode and a distant return, then using the parallel combination of the central electrode and first ring, and so forth. Unfortunately, unused electrodes may

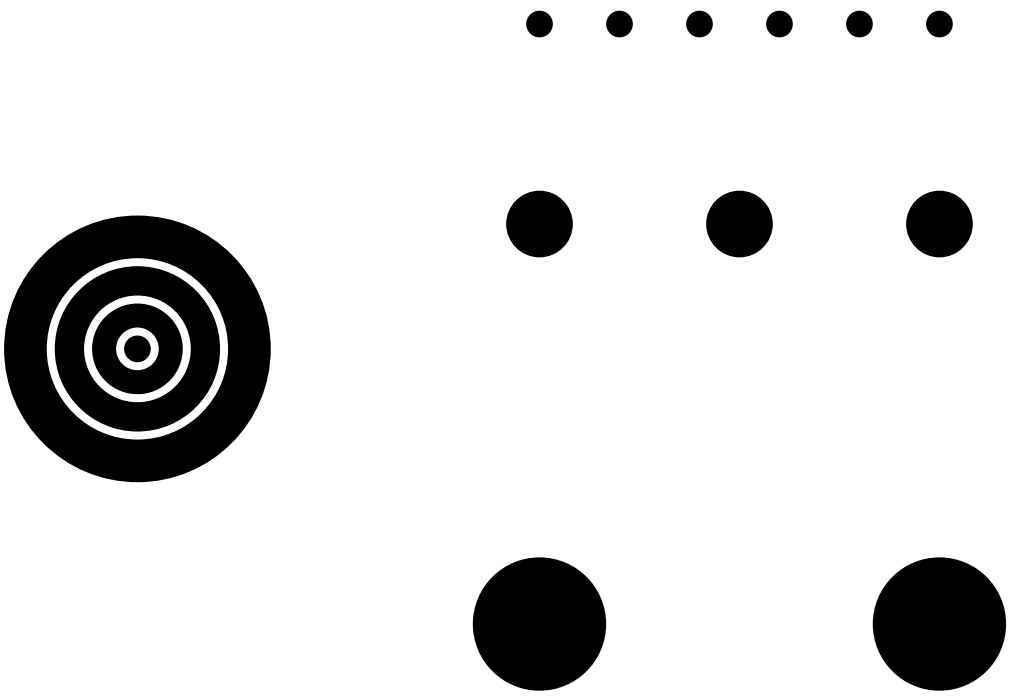

(a) (b)

Figure 5.2: Array patterns for measuring thresholds versus electrode diameter. (a) A concentric ring electrode could be used to measure thresholds for several electrode diameters, but field distortion from unused electrodes will probably confound the results. (b) An array with several electrode sizes can be used to compare thresholds from the same retina but at different stimulation sites.

significantly distort the stimulating field as noted in Chapter 4. Hence stimulating fields obtained with central electrode alone will be spatially smoothed by the large surrounding rings, and will probably have higher threshold currents than would the same electrode surrounded by insulator only. This ambiguity can be avoided with arrays containing simple disks of different sizes which are placed reasonably far apart (a few electrode diameters), as in Figure 5.2b. Thresholds for a range of different sizes can be measured on the same retina, but the group of neurons stimulated will be different for each electrode.

Appendix A

Thresholds for *In Vitro* Human Retina

On August 18, 1999, a sample of living human retina was made available for study. The sample came from the eye of a patient at the Massachusetts Eye and Ear Infirmary with cancer of the lacrimal gland extending throughout the eye socket. The patient's eye was removed as part of the cancer treatment. The patient was aged 77, male, with 20/25 acuity and no known visual problems.

In surgery, the entire eye socket with surrounding bone was removed. The intact eye was then removed from the socket, placed in normal saline solution, and rushed to the laboratory where it was opened and the retina dissected free. The retina was placed in oxygenated Ames' medium (pH 7.3-7.4) approximately one hour after removal of the eye from the patient.

Single unit spike thresholds were measured exactly as described in Chapter 2, except that in this case the retina patch was cut from the periphery. A total of 53 thresholds were measured for units picked up by six different recording electrodes. Monopolar thresholds were similar to those found in rabbit, ranging from .2 to 1.3μA.

A partial monopolar threshold map was made for one unit. This map is shown in Figure A.1.

Graded potentials made it impossible to determine thresholds at many of the stimulating electrodes. However, the low variation in thresholds along the third column of the map (particularly among the upper five electrodes) suggests that the alignment of the fiber under study was close to vertical. Furthermore, the fourth column contained two large thresholds which suggested that the fiber was to its left.

Bipolar thresholds were measured with pairs of electrodes spaced 50μm apart in the same row (horizontal alignment) or column (vertical alignment). The current source was connected to the bipolar electrode pairs in a manner analogous to that described in Chapter 3, with the + terminal of the current source connected to the electrode with lower monopolar threshold. This was verified by the fact that spikes always immediately followed the end of the stimulus phase which drove this electrode

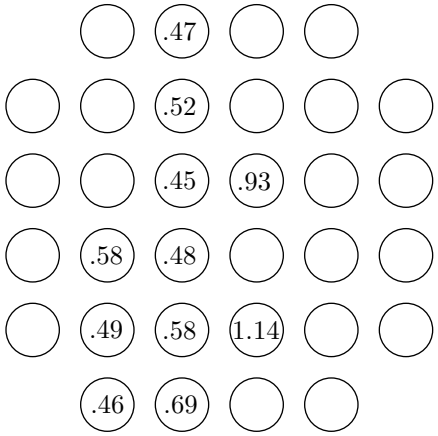

Figure A.1: Monopolar threshold map for *in vitro* human retina. Thresholds are in μA

Normalized thresholds	
Vertical	Horizontal
1.02	1.39
1.11	1.46
1.16	1.51
1.22	1.54
	1.56
	1.64

Table A.1: Normalized thresholds for horizontal and vertical bipolar stimulation.

cathodically (see Chapter 3).

Normalized bipolar thresholds are listed in Table A.1. Even though the surface separation between fiber and electrodes was uncertain, it is clear that normalized thresholds for horizontally aligned stimuli were greater than those for vertically aligned stimuli.

These results suggest that:

- The unusually low thresholds reported in Chapter 3 are not particular to rabbit; fibers at the surface of human retina can also be stimulated at sub-microampere currents. The discrepancy with thresholds for human phosphene perception, which were several hundred microamperes or larger, cannot be accounted for by retinal anatomy differences in the two species.

- Fiber thresholds depend on field orientation in human retina just as they do in rabbit retina. Thresholds are larger for fields running perpendicular to fibers

than for fields running parallel to fibers.

Appendix B

Instrument Designs

B.1 Introduction

To make the measurements documented in earlier parts of this thesis I designed and built several specialized electronic instruments. These instruments consist of: a current source which delivers stimuli to the retina, a bank of nerve response amplifiers which simultaneously monitor the activity at eight sites on the retina, and a pair of amplifiers which monitor the electrode current delivered (which, in principal, should be equal to that requested of the source) as well as the voltage required for delivery. Functional block representations of the new instruments are shown in bold outline in the diagram of Figure B.1. This appendix details their designs.

B.2 Stimulator design

A block diagram of the stimulator is shown in Figure B.2. The circuit consists of several subsystems, including an isolator which decouples the computer D/A ground from the current source ground, an active filter to reduce high frequency noise added to the signal by the isolator, a switching network to decouple the still somewhat noisy signal from the current source when the stimulator is not in use (this reduces noise picked up by the response amplifiers), and the current source itself. The details of these subcircuits will now be considered in turn, followed by a summary of the stimulator's measured performance.

B.2.1 Isolator

The current source ground is isolated from the computer D/A ground using a Hewlett-Packard HCPL-7820 chip, which converts input voltages to a stream of digital bits, transmits the stream optically across an electrical isolation barrier and then converts the bits back to an analog voltage on the output side. Isolation implies that almost

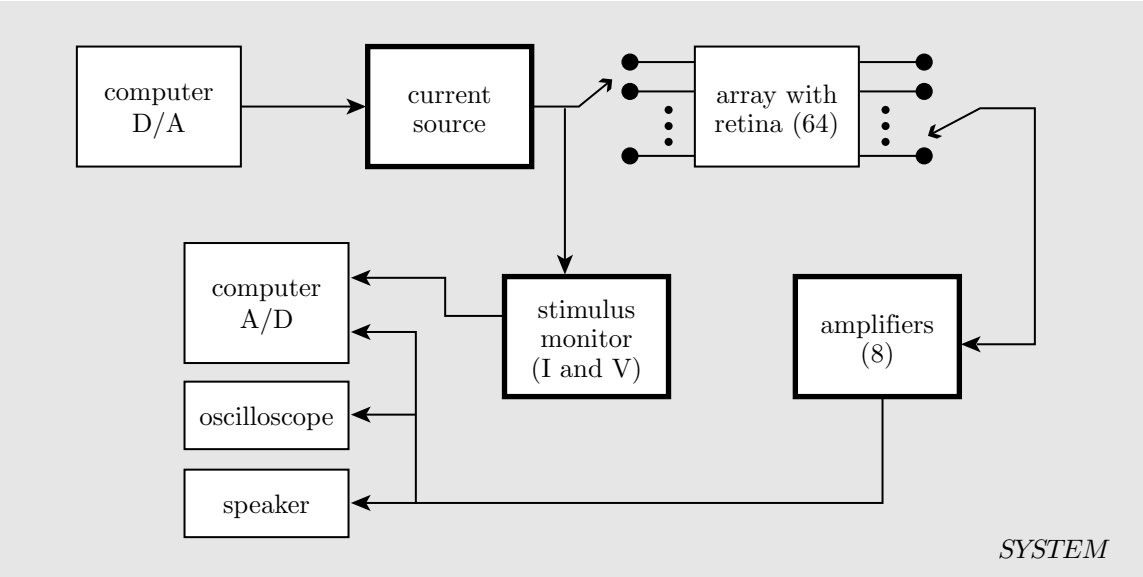

Figure B.1: Block diagram representing signal flow in the experimental apparatus.

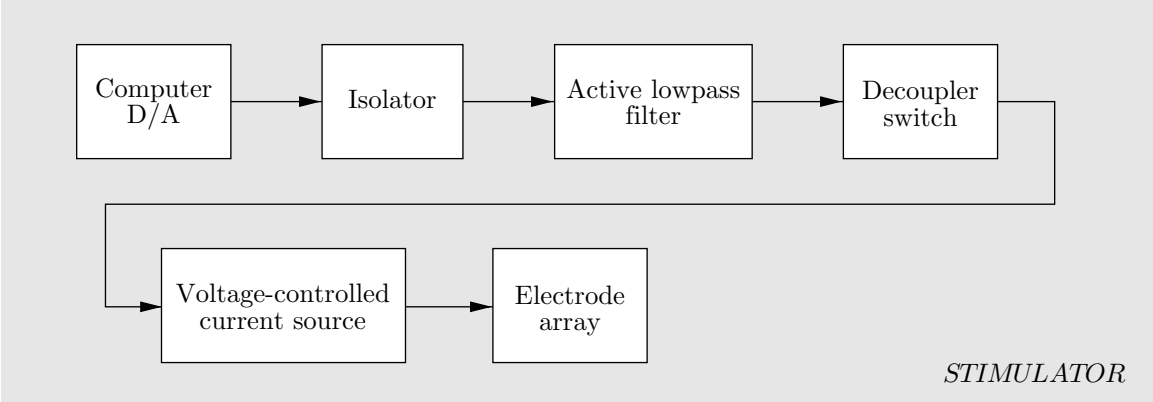

Figure B.2: Block diagram of the stimulator.

ISOLATOR

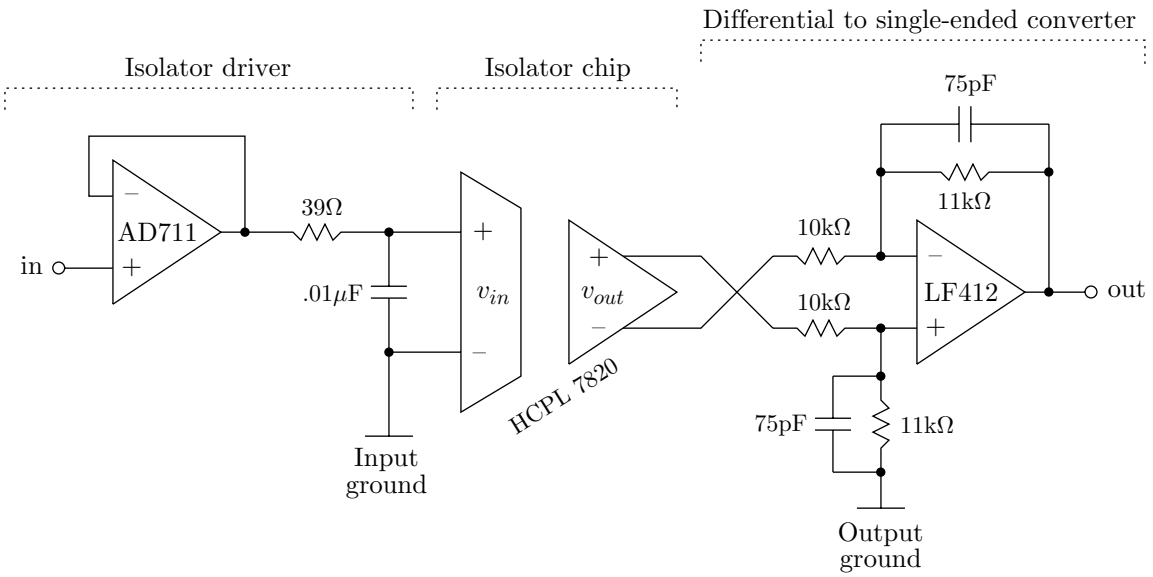

Figure B.3: Schematic diagram of isolator driver, isolator, and differential to single-ended converter.

no electric current will flow in loops passing through the isolation barrier, so that the stimulator output can be treated as a floating source.

The stimulator command voltage generated by the computer is coupled through a 50:1 resistor divider to the isolator circuit illustrated in Figure B.3 (the resistor divider is not shown in the Figure). The first section of the circuit, labeled Isolator driver, consists of an op-amp buffer and a passive lowpass filter. The filter, used on the suggestion of the 7820 data sheets, stabilizes the switched-capacitor filters at the input of the chip, as well as acting as an anti-aliasing filter. Referring to second section of Figure B.3, labeled Isolator chip, the HCPL-7820 has the following characteristic

$$v_{out} = 8v_{in}; \qquad -200\text{mV} \leq v_{in} \leq +200\text{mV}.$$

Within the indicated range of input voltages, Hewlett-Packard guarantees the differential gain of 8 to within 3%. The resistor divider mentioned above (not shown in Figure B.3) scales the ±10 volt output range of the computer's D/A board to the acceptable HCPL-7820 input range. The third section of the isolator circuit converts

the differential output of the HCPL-7820 to a single-ended signal. The differential to single-ended converter has a low frequency gain of 11/10 which rolls off above 200kHz.

B.2.2 Lowpass filters

The output of the 7820 is substantially contaminated with noise, primarily near 500 kHz, which is generated by a chopper-stabilized amplifier inside the chip. Unfiltered, this noise is roughly 100mV peak-to-peak at the output, or 12.5 mV peak-to-peak referred to input. Considering the peak allowable input voltage of 200 mV, this noise represents a severe limitation on the useful range of signals which can be passed through the 7820.

Since this noise is in a slightly higher band than frequencies of interest (stimulation pulse widths no shorter than 20μs are anticipated), it can be substantially filtered out with four poles of lowpass in the 100kHz to 200kHz range. The first pole is provided by the differential to single-ended conversion circuit of Figure B.3. The fourth pole is provided by a passive RC formed through the analog switch in the decoupler circuit (see Figure B.5) by the 1kΩ resistor and the 680pF capacitor.

The second and third poles are provided by an active, lowpass, two-pole Bessel filter. The filter is implemented using the circuit of Figure B.4 with R_1=13.3kΩ, C_1=47pF, R=37.4kΩ, and K=1.267. A Bessel-type filter provides a compromise between a steep pass-band (to reject the isolator noise) and good time domain performance (preserving the shape of rectangular current pulses). The 3dB cutoff frequency of the filter is given by $f_c = 1/2\pi R_1 C_1 f_n$, where $f_n = 1.272$ (Horowitz and Hill, 1989), yielding a cutoff of 200kHz.

The input-referred isolator noise is reduced by the lowpass filters to 1.25mV pk-pk. Referenced to the input of the stimulator (i.e. to the input of the resistor divider preceding the isolator section), this noise is about 63mV pk-pk.

B.2.3 Decoupler circuit

Even with the reductions provided by the lowpass filters discussed above, an appreciable amount of noise is still present in the signal driving the controlled current source. Out of concern that this noise might distort the recorded neural signals, a means was provided to decouple the noisy isolator output from the current source input when not passing stimulation current. This decoupler circuit is illustrated in Figure B.5.

An analog switch (MC14066) is used to either connect or disconnect the active filter output from the voltage-controlled current source. When passing stimulation current, the switch is closed by applying a logic HIGH (5V) to the On/Off terminal of the stimulator. Conversely, the switch is opened when no stimulation current is desired by applying a logic LOW (0V) to the ON/OFF terminal.

The switch control signal, provided by the computer, is isolated from the controlled current source ground using the NEC2501 light-emitting diode/phototransistor pair.

ACTIVE LOWPASS FILTER

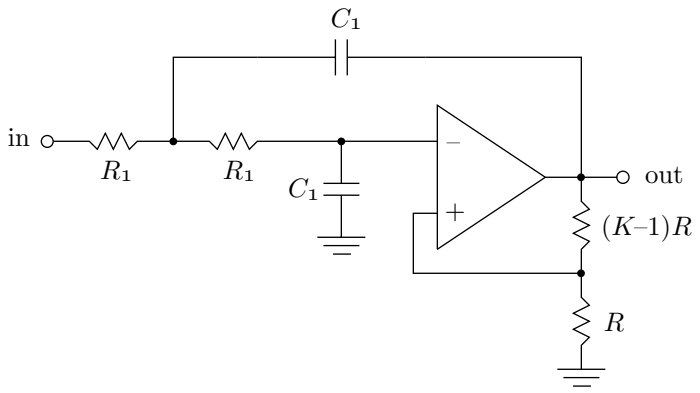

Figure B.4: Schematic diagram of a generic 2-pole active lowpass filter.

A more complex isolation amplifier such as the HCPL-7820 is not needed in this case since the signal to be isolated is digital. The ECL inverter formed by Q1 and Q6 supplies about 4mA to the NEC2501 input when the ON/OFF terminal is at 5 volts*, which in turn gets transferred to the output with a (measured) ratio of about two. To keep the switching speed as fast as possible, a relatively low 100Ω resistor is placed on the 2501's output. Multiplied by a current step of about 8mA, this resistance provides a total voltage change of just under 1V at the 2501's output during a logic transition. This small excursion is converted to a rail-to-rail transition (needed to drive the analog switch) using the emitter-coupled logic gate formed by Q3 and Q4 and an RTL inverter (Q5).

A 680pF capacitor is placed at the output of the analog switch in order to minimize the voltage "glitching" generated by charge dump accompanying logic transitions at the switch control input. This capacitor also forms a passive lowpass filter with the switch resistance, helping to reject isolator noise as mentioned in Section B.2.2. The 10kΩ resistor in parallel with the capacitor is used to hold the positive input of the VCCS op-amp near zero when the analog switch is open. With the switch closed, the cutoff frequency of the passive filter is 232kHz, assuming the "typical" switch resistance of 120Ω.

*An ECL inverter is used here rather than a simpler RTL inverter to avoid large changes in the total current demand on the power supply, averting possible stimulus artifact contributions via power supply coupling.

DECOUPLER

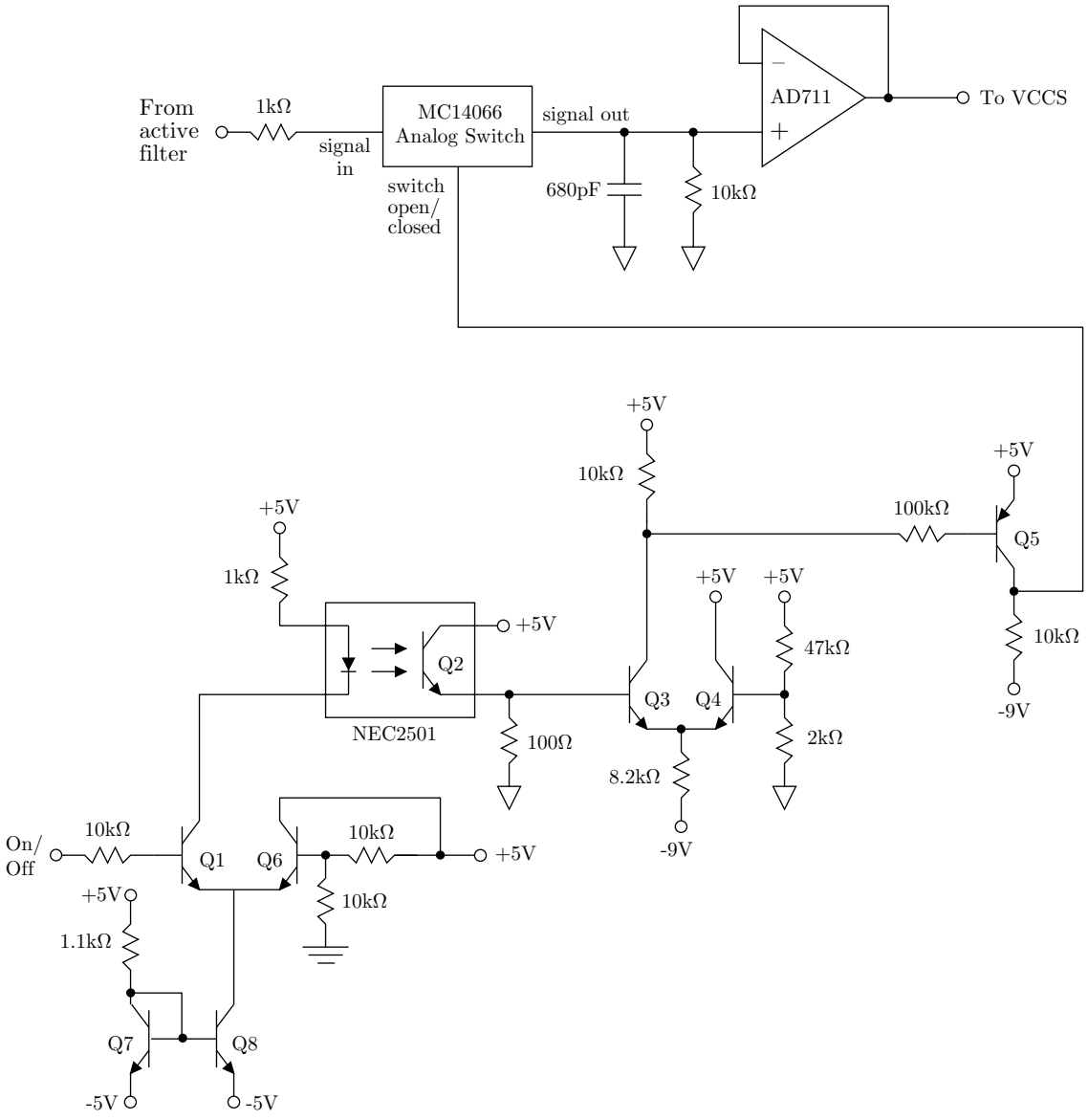

Figure B.5: Schematic diagram of circuit used to decouple the stimulator from the noisy isolator output.

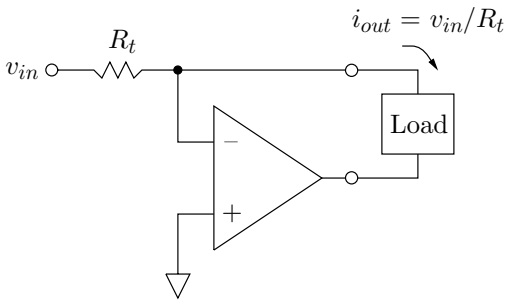

Figure B.6: Voltage-controlled current source topology.

Finally, to help minimize transients at the current source output upon switch opening or closing, two offset-trimming potentiometers are provided (not shown in the Figures). With the decoupler opened, the offset of the VCCS op-amp (AD711 in Figure B.7) is first zeroed using a trimpot connected directly to that op-amp. Then the switch is closed, and the offsets associated with the preceding amplifier and filter stages are zeroed by adjusting the trimpot connected to the isolator driver buffer (see Figure B.3). This procedure ensures that turning the switch on and off does not produce steps in the stimulation current when it is set to zero.

B.2.4 Current source

Essential topology

In its simplest form, the voltage-controlled current source (VCCS) used in the stimulator circuit may be drawn as in Figure B.6. If the operational amplifier output is not saturated or slewing, the current i_{out} through the load is

$$i_{out} = v_{in}/R_t.$$

The resistor R_t (the $_t$ is for *transconductance*) sets the ratio of input voltage to output current. One of three different values of R_t—10kΩ, 100kΩ, and 1MΩ–is selected by shorting together an appropriate pair of jumper posts on the stimulator circuit board.

Output circuit

A collection of resistors and capacitors are connected between the VCCS output and the stimulator output terminals. The significance of these elements, which are shown

VCCS

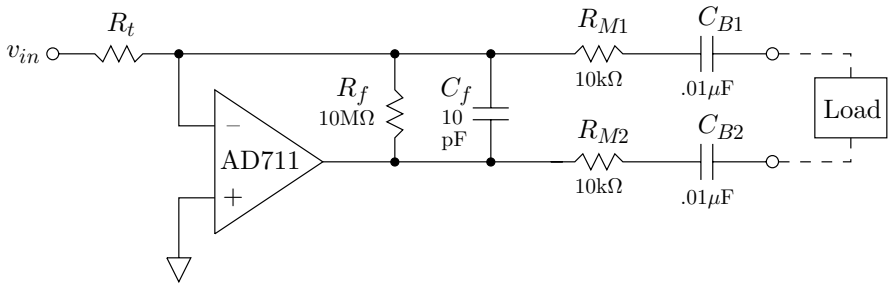

Figure B.7: Voltage-controlled current source and output network.

in Figure B.7, are now considered.

R_f and the C_B's

The capacitors C_{B1} and C_{B2} block DC and low-frequency currents from flowing through the electrodes. These are needed because sustained current can cause irreversible chemical reactions capable of destroying the electrodes or damaging the retina (Robblee and Rose, 1990). The total amount of unbalanced charge deliverable to the electrodes is approximated from the value of the capacitors and from the supply levels used to power the operational amplifier in Figure B.7. For example, if $C_{B1} = C_{B2} = .01\mu$F, and if the op-amp is powered by ± 9 volts, then at most the op-amp can deliver

$$\mathrm{Q} = \pm\frac{1}{2} \times .01\mu\mathrm{F} \times 9\mathrm{V} = \pm 45\mathrm{nC}$$

of unbalanced charge before it saturates. This charge is equivalent to a 1ms long pulse of 45μA, or a 10ms long pulse of 4.5μA.

The large resistor R_f provides feedback to stabilize the operational amplifier at DC. The value of R_f was chosen to be large enough to minimize shunt current away from the stimulating electrodes[†], but small enough that the DC gain ($-R_f/R_t$) provides reasonable stability in the face of the nonzero, drift-prone input offset voltage of the op-amp.

[†]The impedance of 10μm-diameter disks plated with platinum black, at time scales comparable with stimulation pulse widths, has a magnitude on the order of 100kΩ and a slight negative phase shift (see Figure B.23).

The output network will only deliver currents lasting less than about $R_f C_{B1}$ seconds (see section B.6). Given R_f, the value for the C_B's was chosen to keep the $R_f C_B$ product about two orders of magnitude above the width of the longest anticipated stimulation pulses (about 1ms duration).

The R_M's

The resistors R_{M1} and R_{M2} are used to measure the stimulation current flowing through the load. Since the voltage across these resistors is $i_{out} R_M$ when the load current is i_{out}, we can measure the voltage across the resistors to determine i_{out}. This provides a means to verify that the load is actually receiving the desired current. Measuring the voltage across *both* terminals of the current source provides a way to verify if and when it is behaving as an ideal two-terminal circuit element (see section B.5.2).

C_f

Placing the capacitor C_f as shown in Figure B.7 was found experimentally to eliminate a slight "jaggedness" appearing in the step response of the load current. The feedback provided by C_f apparently stabilizes the network at high frequency. The addition of C_f also increases the rise-time of the load current (see section B.6).

B.2.5 Performance specifications

Description	Value	Units	Note
Noise floor	∼63	mV	1
Maximum input	±10	V	2
Output Current to Input Voltage ratio	.2, 2, 20	μA/V	3
10% - 90% Rise time	2-7	μs	4
Output Voltage Limits	∼-7.3 and +7.9	V	5

Notes:

1. Measured at the input of the voltage-controlled current source, and referred to the stimulator input (i.e. the input to the voltage divider driving the isolator section).

2. The HCPL-7820 isolator gain is guaranteed to within 3% for input voltages between -200mV and +200mV. Since the stimulator input is divided down by

a factor of 50 before delivery to the isolator, as much as 10 volts positive or negative can be applied without compromising accuracy. Somewhat larger signals can be applied without damaging the isolator (see HCPL-7820 data sheets, from Hewlett-Packard). However, the isolator output will begin to clip when its input magnitude rises above 320mV.

3. The output current to input voltage ratio is set by a jumper labeled R_t which is located on top of the circuit board holding the stimulator.

   For a particular value of R_t, this ratio is calculated by multiplying $1/R_t$ and the product of the attenuator ratio (1/50), the isolator gain (8), the gain of the differential to single-ended converter (11/10), the gain of the Bessel filter (1.267), and the attenuation of the final lowpass filter which includes the switch (about 10/11).

4. The 10% - 90% rise time was determined by examining the voltage transient across R_{M2}. A 220 kΩ resistor was used as the load. The rise time varied with choice of R_t as follows. For R_t=10kΩ, the rise time was 7μs; for R_t=100kΩ, the rise time was 5.8μs; and for R_t=1MΩ, the rise time was under 2μs.

5. The output voltage limits of the current source are determined by the supply levels used to power the AD711 op-amp which implements the current source, and by the extent to which the AD711 can bring its output to these supply levels. According to the data sheets, for ±15 volt supplies, a typical AD711 can bring its output as high as +13.9V (1.1V below its positive supply) and as low as -13.3V (1.7V above its negative supply). Since the supply rails for this circuit are nominally ±9V, the output voltage limits are estimated as +7.9V and -7.3V (i.e. 1.1V below the positive supply and 1.7V above the negative supply, respectively). It is important to note, however, that the current source is powered by 9V alkaline batteries, whose terminal voltages may start slightly above 9V and will fall below 9V with time and use.

B.3 Stimulus monitor amplifier design

Two nearly identical amplifiers were built to monitor stimuli as they were delivered to the array. One of these monitors amplifies the voltage across a 10kΩ resistor in series with the load (labeled R_{M1} in Figure B.7), providing a measure of the current. The other monitor was usually used to track the voltage output of the current source op-amp (AD711 in Figure B.7). This voltage is dominated by the drop across the stimulating electrodes. In a few instances (see section B.5.2) the second monitor was used to measure the voltage drop across R_{M2}, allowing for simultaneous measurement of both current source branch currents.

A block diagram for one stimulus monitor is shown in Figure B.8. The monitor

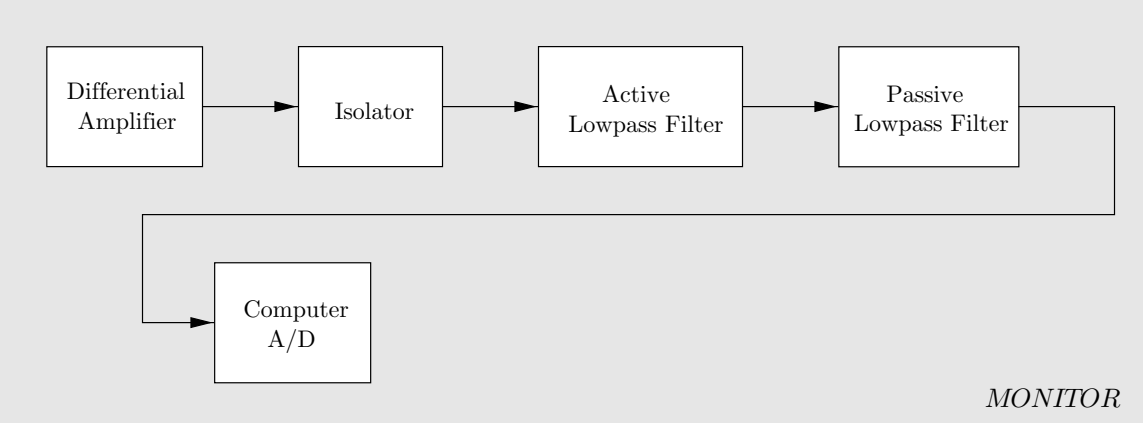

Figure B.8: Block diagram of one stimulus monitor.

circuit consists of a differential amplifier, an isolation network identical to that used in the stimulator circuit, an active lowpass filter, and a passive lowpass filter.

B.3.1 Differential amplifier

A schematic diagram of the differential amplifier at the stimulus monitor input is shown in Figure B.9. Op-amps TCL274A and TLC274B provide a differential gain of $[2(R_A/R_B) + 1]$. For measuring current I used $R_A = 23.7\text{k}\Omega$ and $R_B = 2.49\text{k}\Omega$ yielding a gain of 20.04; for measuring voltage I short-circuited R_A and open-circuited R_B for a gain of 1. Op-amp TLC274C converts the differential signal to single-ended with a gain of 1. A jumper, labeled "÷N", provided attenuation of monitor signals to avoid saturating the subsequent isolator circuit. For measuring current I set N=10 to provide optional 1/10 attenuation; For measuring voltage I set N=20 and always shorted the jumper terminals.

The TLC274 op-amps have high impedance MOSFET inputs, and were used to minimize the the amount of current shunted away from the stimulating electrodes by the monitor amplifiers. The three op-amp differential amplifier topology was chosen for its ability to completely reject common-mode steps at its inputs.

No special precautions were taken to minimize the offset voltages of the monitor amplifiers. The input offset voltages for the TLC274 op-amps can be as high as 10mV. In a worst case scenario, this would lead to a differential input offset voltage of 20mV, which in turn would yield 4V at the output of the current monitor. Luckily, the measured offset voltages are much smaller (see below). Perhaps we can assume from this that the input offset voltages of the op-amps within the TLC274 quad package are fairly well matched. In any event, the offsets are tolerable, so the design

DIFFERENTIAL AMPLIFIER

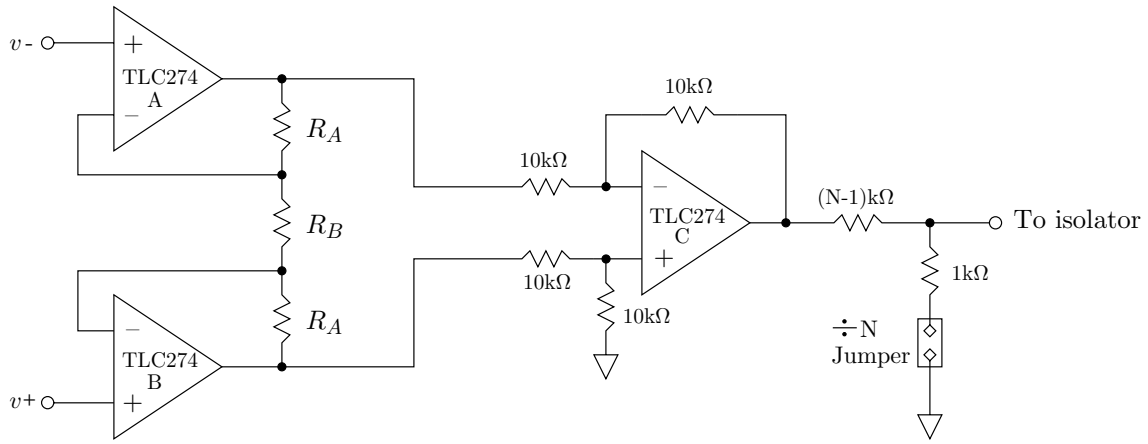

Figure B.9: Schematic diagram of the differential amplifier at the input of the stimulus monitor.

will be accepted as it is.

B.3.2 Isolation and filters

An isolation circuit, identical to that shown in Figure B.3 was used to isolate the differential amplifier ground (which is the same as the ground used for the voltage-controlled current source) from the computer A/D ground.

All of the comments made with regard to the use of the HCPL-7820 isolation amplifier in section B.2.1 are applicable here as well. The isolation amplifier is preceded by a buffer/drive and followed by 4 poles of lowpass filtering. The first of these poles is provided by the differential to single-ended converter (Figure B.3), the second and third poles by a Bessel filter (Figure B.4), and the fourth pole by a passive RC filter.

B.3.3 Performance Specifications

Monitor	÷N Jumper	Output/Input Ratio[1]	Output Offset[2]	Maximum Input[3]	10% - 90% Rise Time
1	ON	-.5 V/V	+12 mV	4 V	5 μs
2	ON	.2 V/μA	0 mV	10 μA	6 μs
2	OFF	2 V/μA	-110 mV	1 μA	6 μs

Notes:

1. The output to input ratio is set by a jumper labeled ÷N, where N=10 or N=20, on the circuit board holding the monitors.

   The ratio is calculated by taking the product of the measurement resistance (10kΩ), the differential gain (20), the attenuation (1/N), the isolator gain (8), and the Bessel filter gain (1.267).

2. The output offset voltage was measured with the monitor input terminals grounded.

3. The maximum input current is determined primarily by the limitation on the magnitude of the input to the HCPL-7820.

4. The monitors were driven with common mode steps of a few hundred mV, and no sign of these was observed on the outputs.

B.4 Nerve response amplifier design

In order to record from a large number of sites while maintaining reasonable hardware complexity, I built 8 amplifiers which can be electronically switched between each of 8 electrodes. This situation is depicted schematically in Figure B.10. To simplify the description of this design, a block diagram is shown in Figure B.11. The response amplifier circuit consists of several subcircuits. These include a multiplexer which connects one of 8 electrodes to the input of the amplifier cascade, a gain 10 preamplifier, an sample and hold circuit (to reduce stimulus artifacts), a two-pole active lowpass filter, and a high-gain amplifier.

B.4.1 Multiplexer

A schematic diagram of the multiplexer circuit for one amplifier channel is shown in Figure B.12. This circuit connects the preamplifier input to eight electrodes in parallel through electro-mechanical reed relays An analog multiplexer (ADG408) controls the flow of coil current such that only one relay is in the closed position at

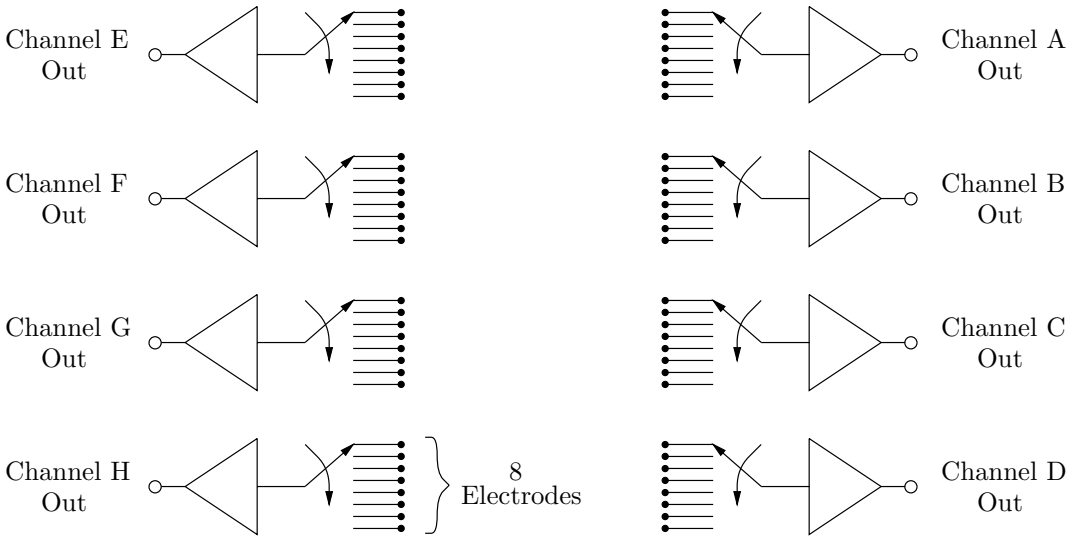

Figure B.10: Eight-channel nerve response recording system.

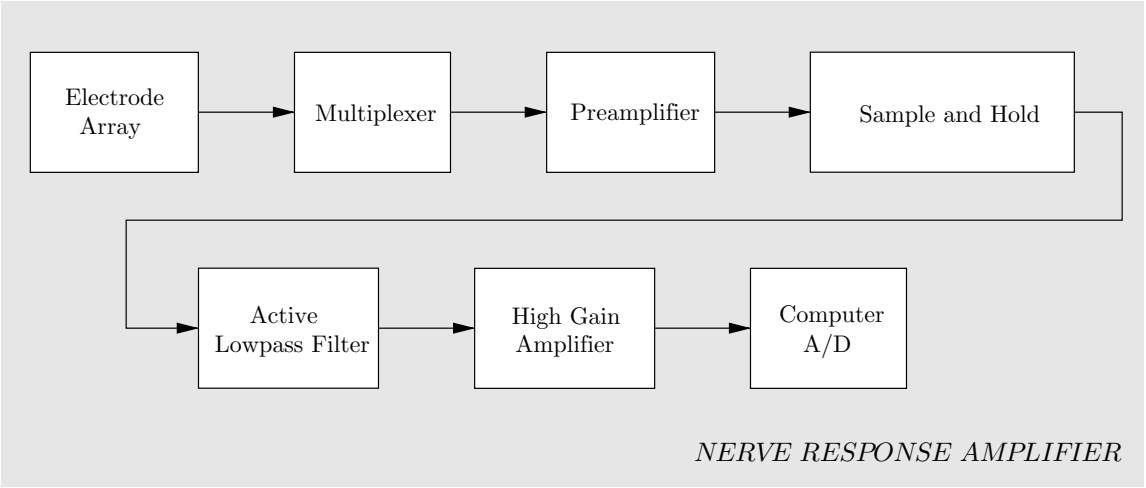

Figure B.11: Block diagram of one nerve response amplifier.

MULTIPLEXER

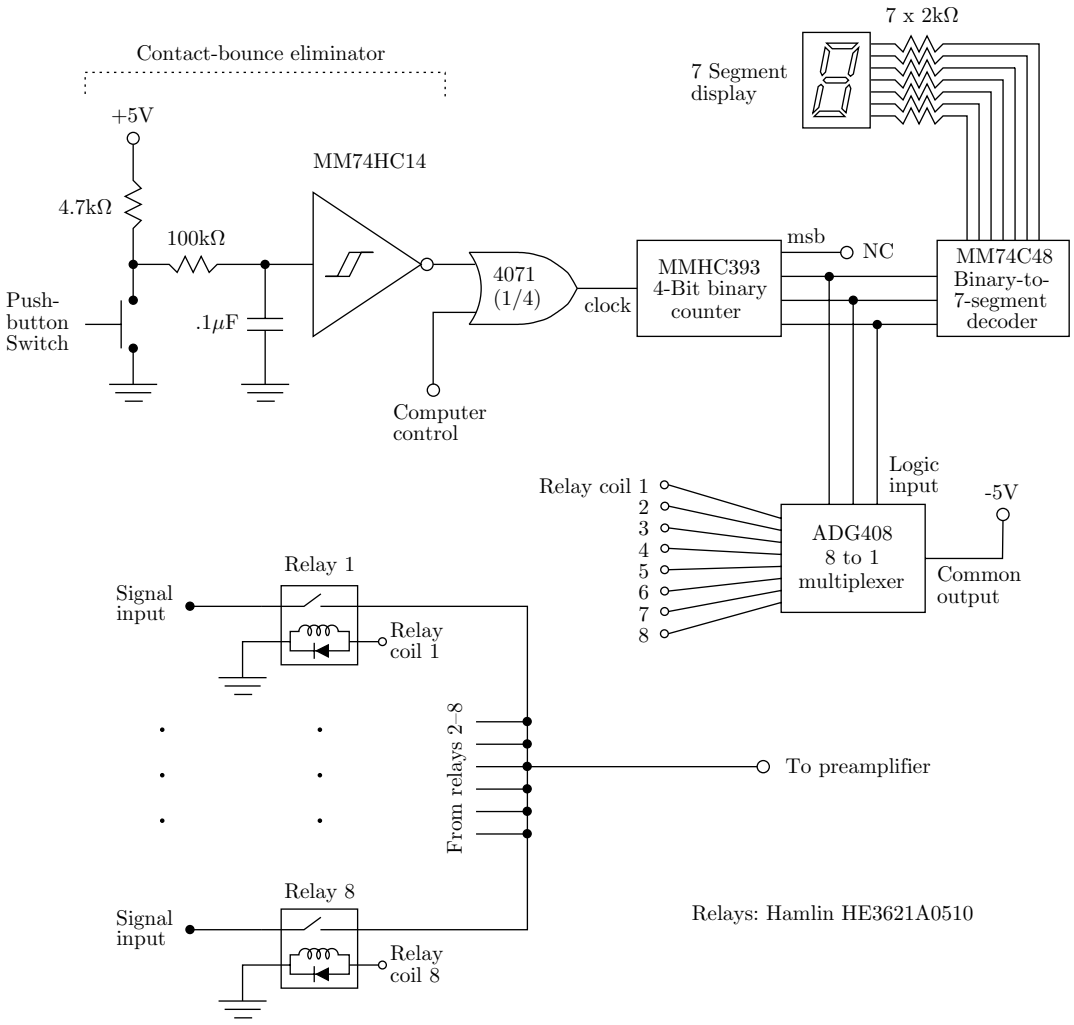

Figure B.12: Schematic diagram of multiplexer circuit for electrode selection.

PREAMP

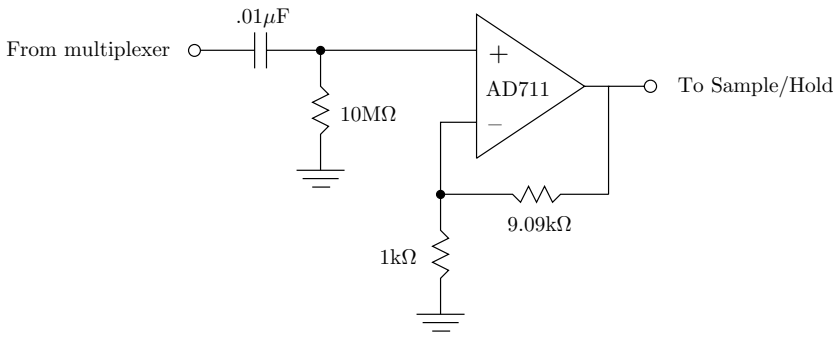

Figure B.13: Schematic diagram of the preamplifier circuit.

a time. The experimenter advances the multiplexer state to select a new electrode using a pushbutton on the front of the instrument panel. The state of the multiplexer is displayed as a digit between zero and seven with a seven-segment LED located on the front of the instrument panel. In addition, the multiplexers may be advanced under computer control.

B.4.2 Preamplifier

A schematic diagram of the preamplifier circuit is shown in Figure B.13. The multiplexer output is coupled to a standard non-inverting amplifier through a .01μF capacitor. This capacitor prevents the AD711 op-amp from drawing DC bias current through the electrodes. Instead, bias currents are provided by a 10MΩ resistor. The non-inverting amplifier provides a gain of (1 + 1kΩ/9.09kΩ) = 10.09. This provides a modest increase in signal level and a low-impedance driver for the long wires separating the preamplifier output (located near the retina) and the input of the sample and hold circuit (located in an instrument chassis a few feet away, in an equipment rack). The gain was kept small to reduce the likelihood of stimulation artifacts saturating the preamplifier.

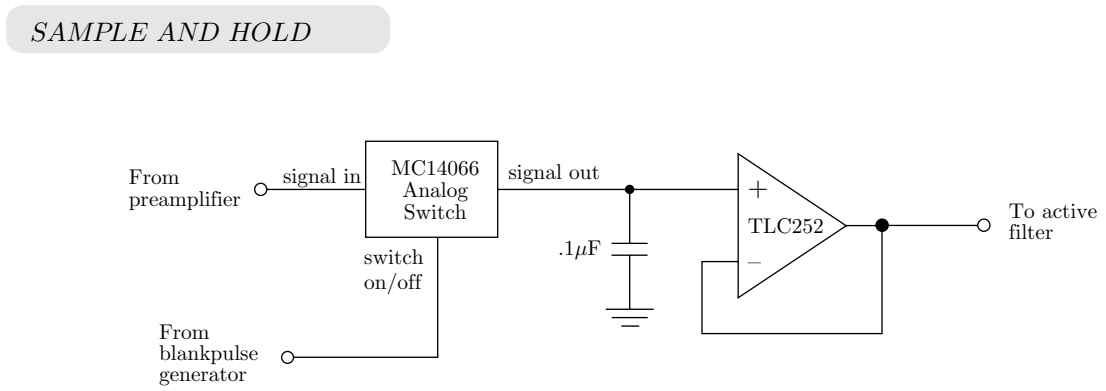

Figure B.14: Schematic diagram of the sample and hold circuit.

B.4.3 Sample and hold

A sample and hold circuit is placed between the preamplifier and the subsequent circuits in order to block transmission of artifacts during stimulus application. A schematic of the circuit is given in Figure B.14.

Normally the analog switch (MC14066), placed between the preamp output and a .1μF sampling capacitor, is closed. A logic pulse accompanying stimulation opens the switch for a brief interval. A special circuit shown in Figure B.15 generates a blanking pulse which starts before and ends after the current control waveform is coupled to the stimulator. This helps to ensure minimal coupling of the stimulus to the amplifier output.

The sampling capacitance was made as large as possible to minimize switch artifact (due to charge dump accompanying large voltage swings at the control input of the MC14066), but not so large that RC delays associated with the switch resistance could severely attenuate action potentials. The typical ON resistance of the MC14066 at room temperature is 120Ω (assuming 10V across the power rails). For C=.1μF, the 3dB cutoff frequency is 13.3kHz, which is about where we want it. The maximum ON resistance is 500Ω, which yields a somewhat low but tolerable 3dB cutoff of 3.2kHz. The measured resistance for the 4066 chip used for channels C and D is 88Ω (3dB cutoff at 18kHz).

The sampled voltage on the .1μF capacitor is buffered using a TLC252 MOSFET-input op-amp.

BLANKPULSE GENERATOR

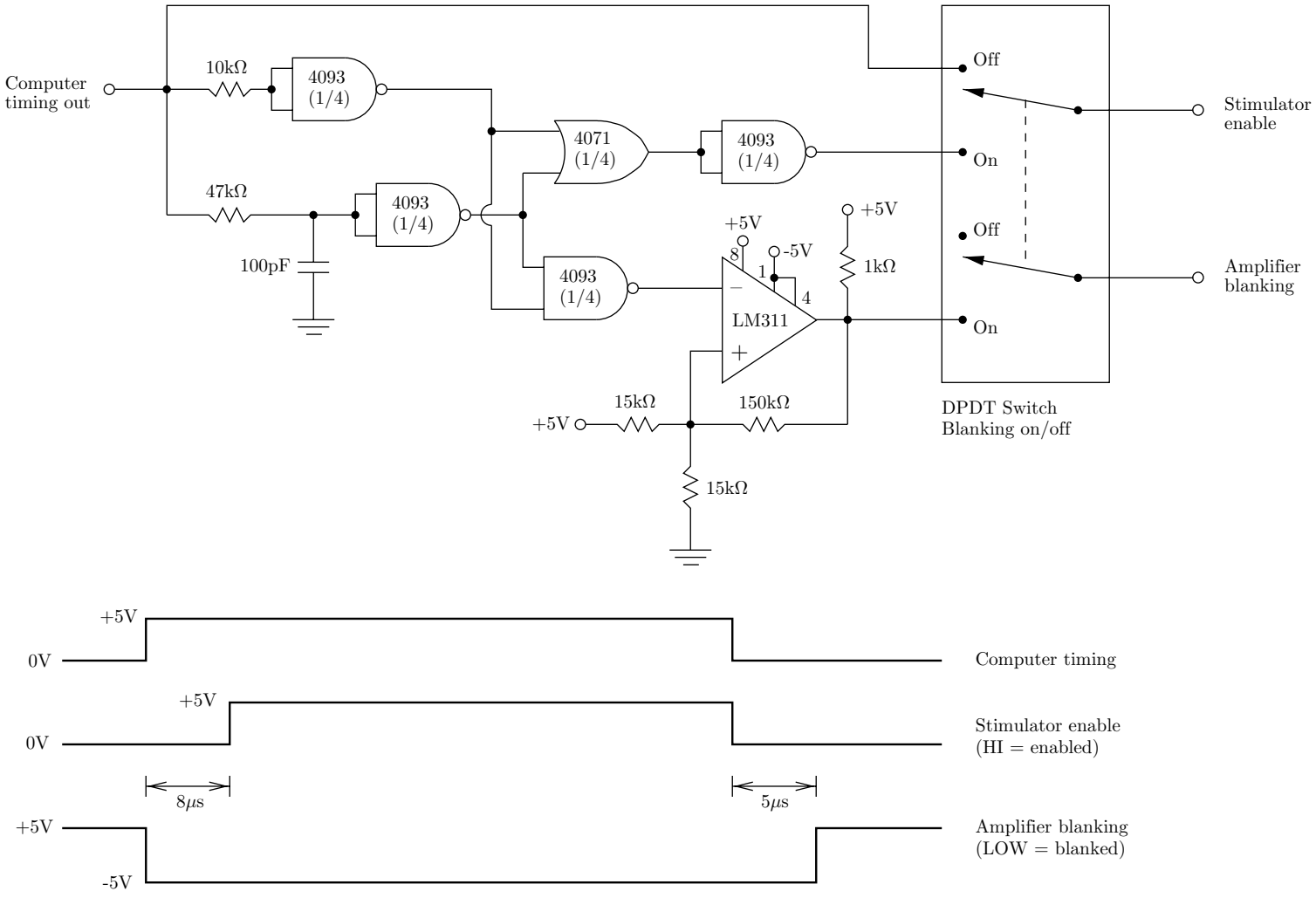

Figure B.15: Circuit for generating blanking pulses.

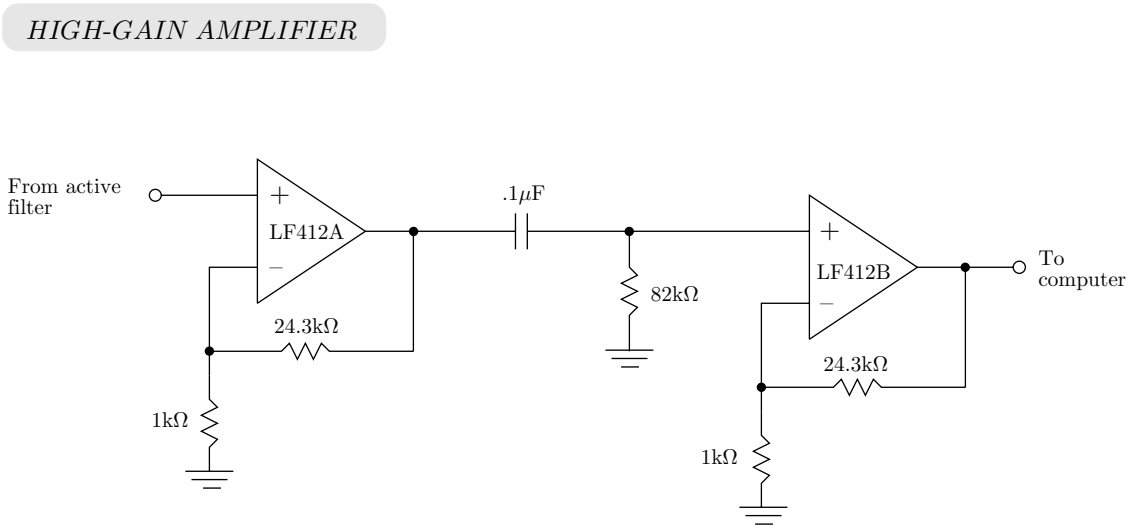

Figure B.16: Schematic diagram of the high gain amplifier.

B.4.4 Active lowpass filter

An active lowpass filter is used to reduce noise components which are outside of frequency ranges of interest. The filter is a second-order Butterworth type, and is used for its ability to provide a relatively sharp transition band while maintaining flat gain in the pass band. To implement the filter, the general active lowpass filter circuit of Figure B.4 is used with R_1=15.2kΩ, C_1=.001μF, R=100kΩ, and K=1.59. The calculated 3B-cutoff of the filter is 10.5kHz, and the low frequency gain is 1.59.

B.4.5 High-gain amplifier

Having been selected, preamplified, sampled and held, and filtered, the signal is finally fed to a high gain circuit. A schematic diagram of this circuit is shown in Figure B.16.

The gain of each of the non-inverting stages is (1 + 24.3kΩ/1kΩ) = 25.3. The passive high-pass filter formed by the .1μF and 82kΩ resistor placed between the two stages removes DC offset at the output of first non-inverting amplifier. The cutoff of the highpass is 19.4Hz, well below frequencies associated with extracellular action potentials.

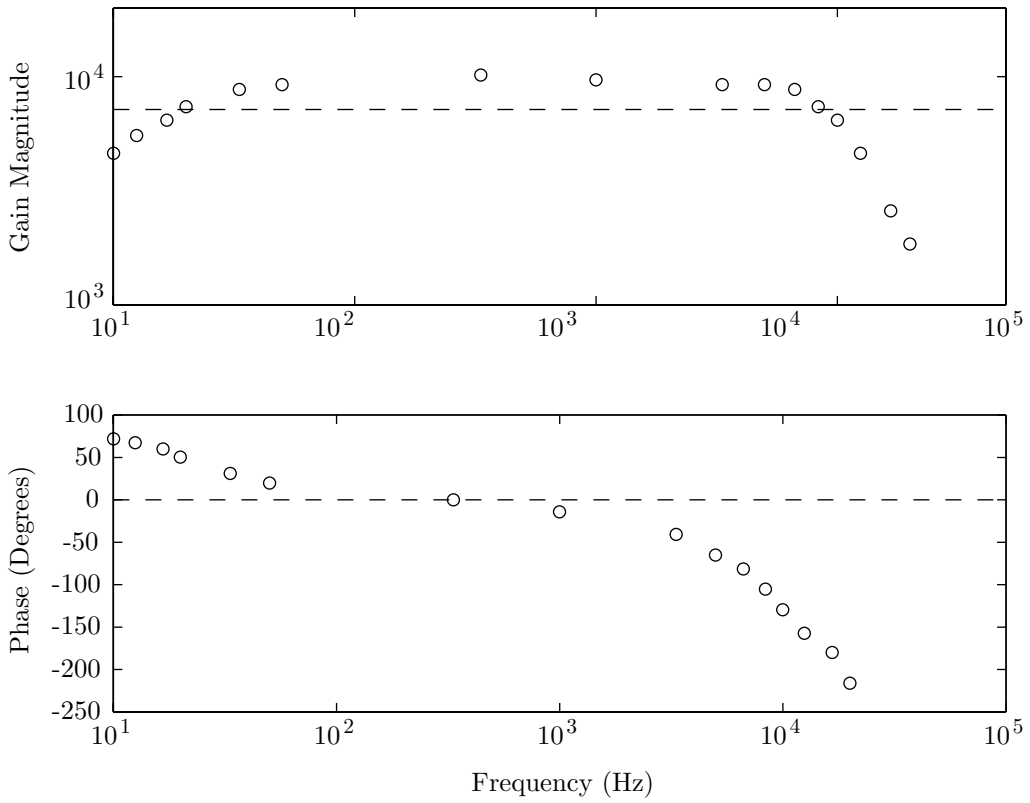

Figure B.17: Gain and phase plots for nerve response amplifier A. The dashed line in the gain plot is 3dB down from the midband gain.

B.4.6 Bode plot

A Bode plot of amplifier "A" is shown in Figure B.17. The measured gain of the amplifier is near 10,000, which is consistent with the calculated value of 10,177. This is found by taking the product of the preamplifier gain (10), the Butterworth filter gain (1.59), and the high-gain amplifier gain (25.3×25.3). The lower 3dB cutoff occurs near 20Hz, as predicted from the highpass cutoff of the passive RC in the high gain amplifier. The upper 3dB cutoff is at approximately 10kHz and the roll-off is steep, as we would expect from two poles in the active filter and the passive pole through the switch in the decoupler circuit.

B.5 System considerations

Three aspects of the circuits described above become most significant when the entire system is connected. These are noise, shunting of stimulator current, and stimulus artifacts. The first two topics are considered below, with another chapter devoted to the somewhat more involved third topic.

B.5.1 Noise

Ideally, when there is no cell activity, there will be no signal at the output of the nerve response amplifiers. In practice, this is not the case. Several sources may contribute noise at the output of the amplifiers, including pickup through the bath of noise generated by the stimulator, electrostatic pickup of noise generated by sources near the amplifier, ground loop pickup of noise generated by sources near the amplifier, and noise generated in the electronic components which are used to provide amplification.

Figure B.18 is a representation of the electronic instruments connected in a realistic configuration. The stimulator and nerve response amplifier are connected to electrodes in a salt water bath. The computer's analog output is connected to the stimulator, which is represented in the Figure as a voltage-controlled current source. The output of the nerve response amplifier is connected to an oscilloscope. Note that the nerve response amplifier and non-isolated side of the stimulator (to the left of the isolation barrier) are powered by different supplies than the isolated side of the stimulator (right side of the isolation barrier). Each set of supplies has its own common, or ground, node: the non-isolated ground is called "com1" in Figure B.18 and the isolated ground is called "com2". Note also that the wired connection labeled $\boxed{1}$ is made, so that "com1" is the same as "earth"[‡] The significance of labeled branches $\boxed{2}$ and $\boxed{3}$ will be considered below in the sections on electrostatic and ground loop pickup. Branch $\boxed{3}$ is shown as a dashed line because it is normally open-circuited.

With the configuration of Figure B.18 and no retina in the salt water, a measurement of the noise was made, sampling every 2μs for 10,000 counts. After subtracting off the absolute value (due to offsets in the amplifier cascade), the output noise amplitude is 52mV rms.

Stimulator-generated noise

Recall from section B.2.3 that the output of the HCPL-7820 isolator is somewhat noisy, and that an electronic switch was added to decouple the isolator from the bath during periods when the stimulator is not in use. Closing the switch was sometimes found to increase the noise on a recording electrode by as much as a factor of ten,

[‡]As it turns out, the ground provided by the plug-in supply which provides power to the non-isolated side (Va and Vb in the Figure) is not equal to the earth potential, so this connection must be made explicitly in order to use a computer or oscilloscope to make single-ended measurements of the amplifier output.

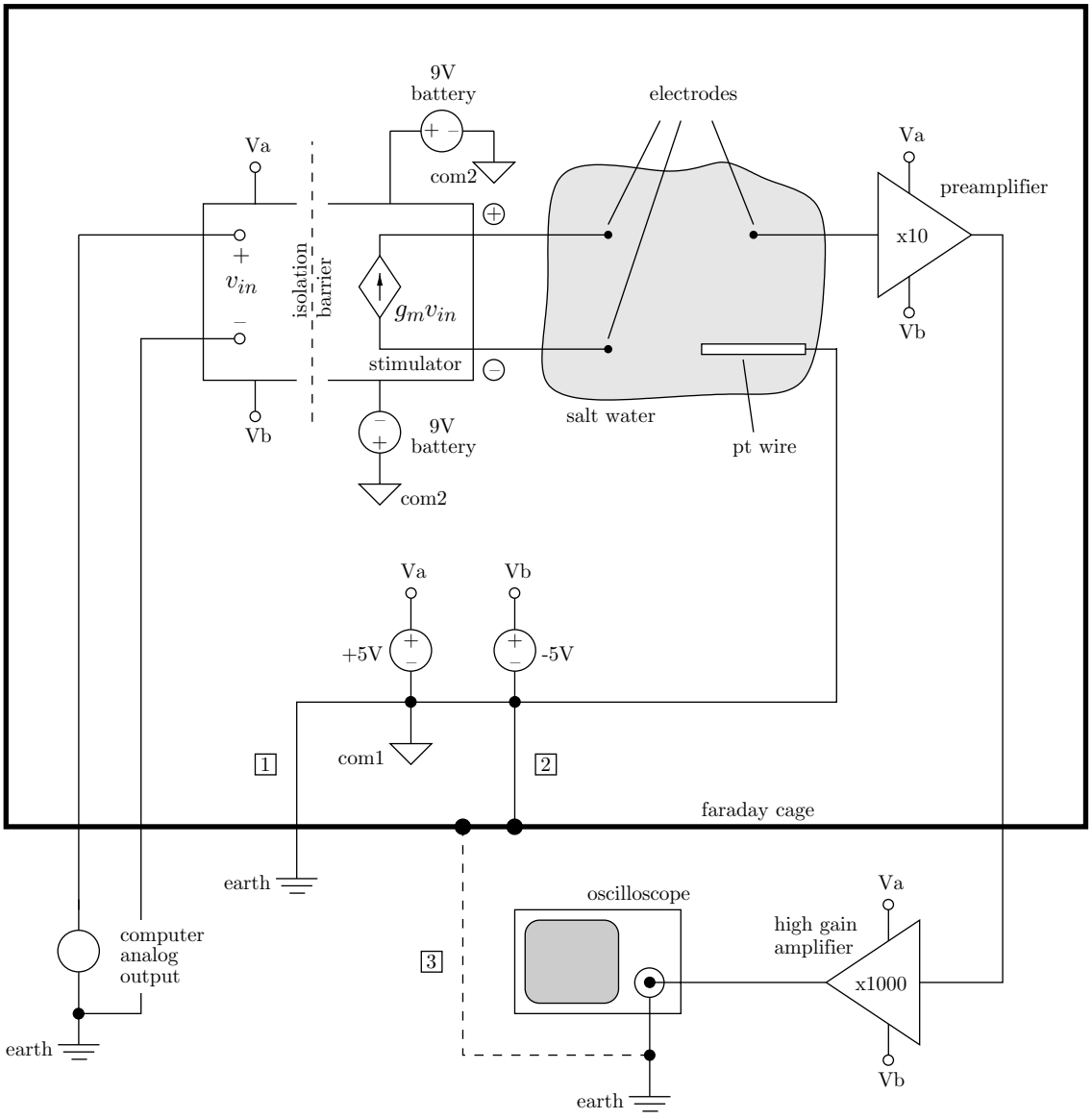

Figure B.18: Schematic diagram of the connected instruments. The current monitor amplifiers are not shown.

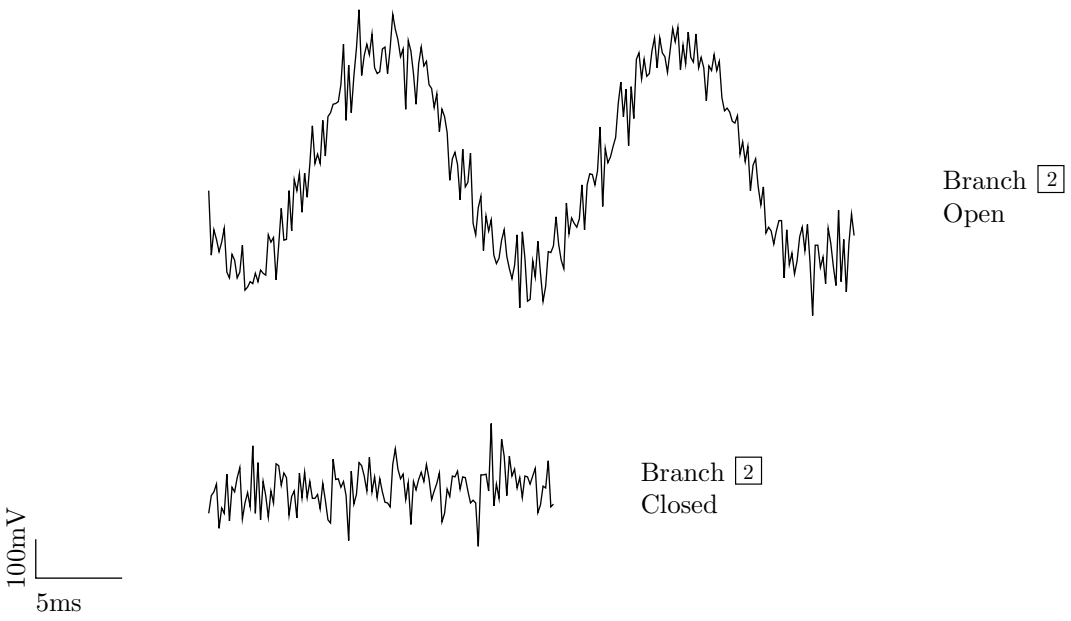

Figure B.19: Noise voltage measured at the amplifier output with branch 2 (Figure B.18) open and closed.

depending on the quality of insulation used and the relative positions of stimulating and recording electrodes. Thus for noise reduction it is advantageous to keep the switch open whenever the stimulator is not in use.

Electrostatic pickup

The input to the high gain amplifier has a very high impedance to ground, even when coupled to earth through the salt water bath. This makes the input node susceptible to capacitive coupling of noise sources in the environment. A Faraday cage, connected to the signal reference potential near the point of signal origination, should eliminate any capacitive coupling (Morrison, 1986). This notion can easily be checked by open-circuiting branch 2 (Figure B.18). Indeed, there is substantial pickup of 60Hz noise, as shown in Figure B.19.

Ground loop pickup

Noise can also be picked up via magnetic interactions when there are ground loops linking flux from a source near the amplifier. Closing branch 3 (Figure B.18), for example, generates such a loop. The path of the loop is illustrated in Figure B.20, which portrays a realistic layout of the ground connections initially used. The ground loop begins at the earth connection in the computer D/A, runs through the "common" node of the nerve response amplifier and through the Faraday cage, and then through the outer shell of the oscilloscope connector back to earth. Figure B.21 shows that under these conditions there is pickup of high frequency noise, which turns out to be near 30kHz. The total noise amplitude is not dramatically increased by the ground loop noise, though the root-mean-square magnitude rises from 52mV to 82mV.

This noise is apparently generated by the nearby computer monitor, since, even with branch 3 closed, the noise disappears when the computer monitor is turned off. With the monitor turned on and branch 3 closed, furthermore, the noise is reduced if physical wire constituting branch 3 is moved far from the monitor. In any event, the magnetic pickup in this case is eliminated easily enough by open-circuiting branch 3.

Noise generated by electronic components in the amplifier cascade[§]

The electronic devices used to build the nerve response amplifiers will also contribute to noise at the output. Unlike the sources discussed above, these sources are intrinsic to the amplifier and essentially inescapable[¶].

Device noise can be estimated from the equivalent input voltage noise e_n ($V/\sqrt{Hz}$) of the source in question, the gain applied between the source and the amplifier output, and the bandwidth over which the gain is large. Table B.1 summarizes estimates for the dominant contributors of device noise. For each of the operational amplifiers, the equivalent input voltage noise at 1kHz, e_n, was taken from the data sheets and assumed to be constant over the appropriate bandwidth.

We can make an estimate of the contribution of device noise if we assume that the noise sources in the Table are independent of one another. In this case the noise is the square root of the sum of the squares of the individual contributions. This value turns out to be 25.9mV rms, or roughly half of the measured value of 52mV rms. Thus, device noise, as estimated here, cannot be the dominant noise source.

As a check on our logic, note that we can connect the preamplifier input to earth without affecting the validity of our estimate for device noise. Under this condition,

[§]These measuresuments and calculations were performed during an earlier revision of the circuit in which the 3dB-bandwidth was 15kHz rather than 10kHz. Though the numbers would be slightly different for the present system, the main message of the section remains the same.

[¶]Of course, "low-noise" and "very low noise" circuit components are usually available. We will see, however, that the dominant noise source in the instrument is not the purchased components, but the electrode-electrolyte interface. This source will be discussed shortly.

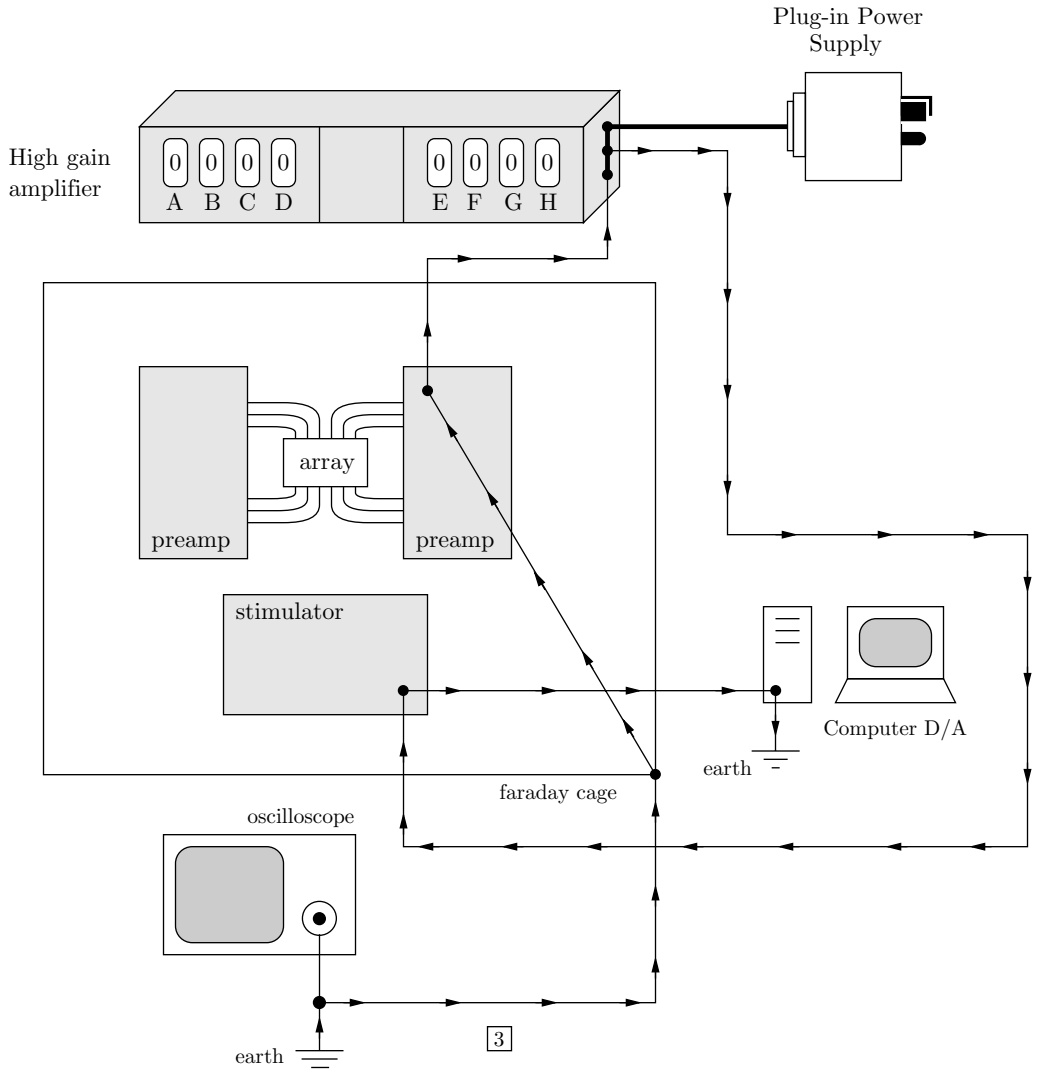

Figure B.20: Schematic diagram of ground connections leading to ground loop pickup from the computer monitor. Closing branch 3 between the oscilloscope BNC shell and the Faraday cage creates a ground loop (arrows) which links magnetic flux generated by the computer monitor.

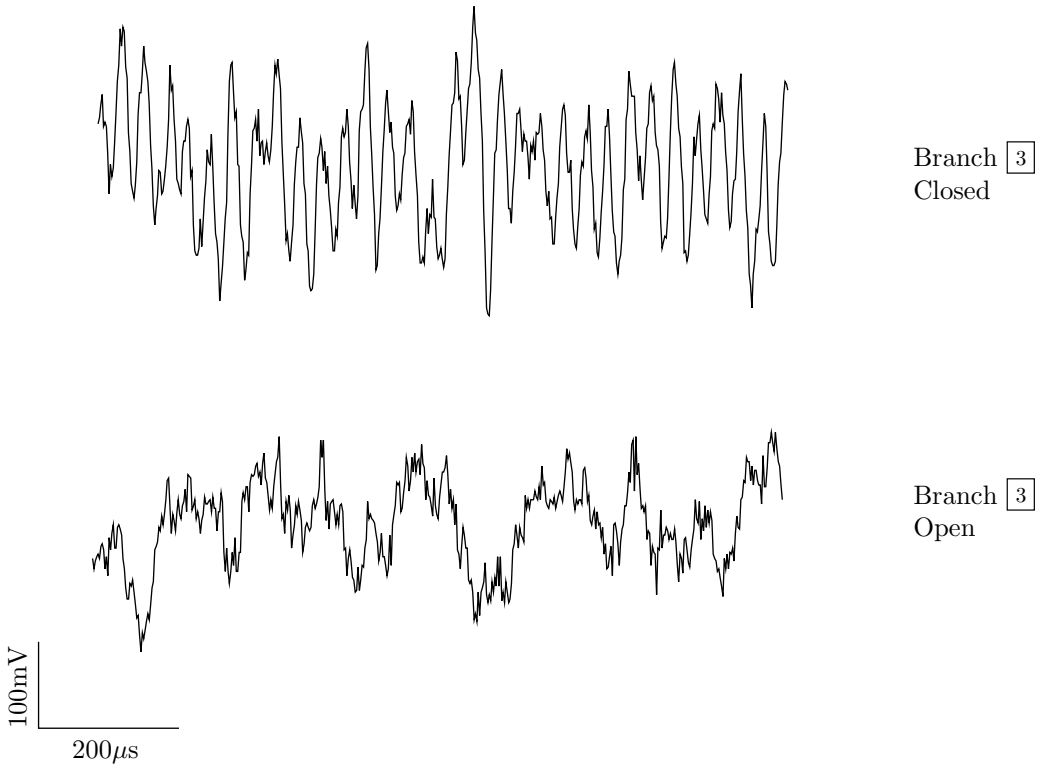

Figure B.21: Noise voltage measured at the amplifier output with branch 3 open and closed.

Source	Circuit Element	e_n (nV/$\sqrt{\text{Hz}}$)	$\sqrt{\text{Hz}}$	Gain	Output Noise at Voltage (mV rms)
1	AD711JN (Figure B.13)	18	$\sqrt{15\times10^3}$	10000	22
2	LF411 (Figure B.4)	30	$\sqrt{4\times10^6/25.3}$	1000	12
3	LF412A (Figure B.16)	25	$\sqrt{4\times10^6/25.3}$	640	6.4

Table B.1: Estimated contributions from major sources of noise in amplifier cascade.

the noise at the amplifier output is reduced to 31mV rms. This value is in reasonable agreement with our estimate of device noise.

Noise generated at the electrode-electrolyte interface

Electronic devices in the amplifier cascade generate a significant, but not dominant, fraction of the total observed noise. Some other source must therefore be responsible for most of the noise. Assuming this source is independent of those associated with the op-amps, its magnitude (integrated over the bandwidth of and multiplied by the gain of the amplifier) should be 41.7mV rms.

It seems most likely that the source of this noise is the electrode-electrolyte interface, since this component is eliminated when the interface is shorted out by earthing the preamp input terminal. A circuit model of the preamplifier input section is shown in Figure B.22. If we model the interfacial impedance Z_E as a resistor generating primarily Johnson noise, we would need $Z_E = 71\text{k}\Omega$ to generate the requisite 41.7mV rms. Measurements of the electrode impedance (see Figure B.23) reveal a complex impedance whose magnitude is in this range, but which has nonzero phase.

Further exploration of the interface noise might elucidate its mechanism, and possibly suggests ways to reduce it. At this point, however, it is worth noting that the total noise, referred to input, is about 5μV rms. In contrast, extracellular spike amplitudes are often 100μV or more, twenty times larger than the noise. Since the expected signal-to-noise ratio is quite good, the subject of noise will not be pursued further.

B.5.2 Current shunting

In Chapter 3 the field distribution in the tissue was controlled through a choice of stimulator connections to the electrode array. Even though the exact field distribution

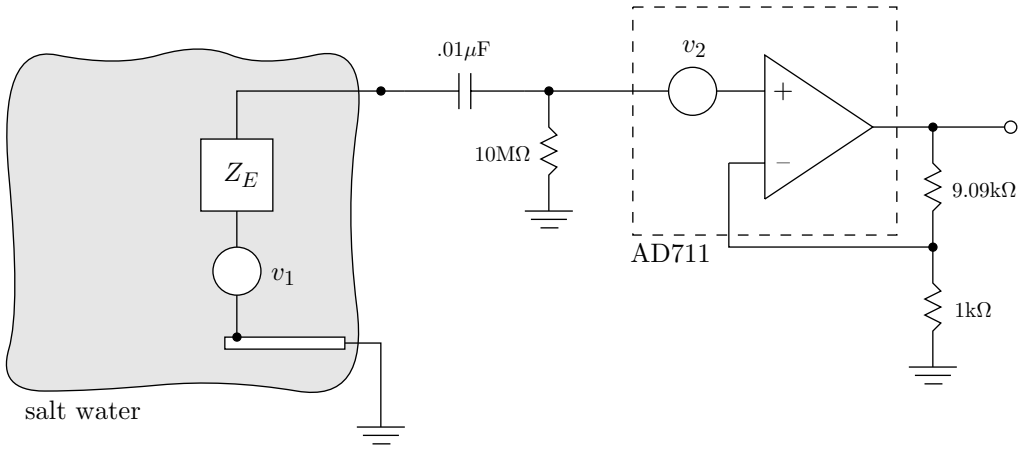

Figure B.22: Circuit model of the input region of the preamplifier. The interface impedance is Z_E, and the associated noise source has magnitude v_1. The equivalent input noise of the AD711 is in series with the + input terminal of the op-amp, and has magnitude v_2.

was unknown, a rough sense was obtained by assuming that current flowed only between the two conductors connected to the stimulator, and that the only available path was through the tissue. Initial instrument designs revealed conditions under which substantial shunt paths were available, weakening the above assumption. This section describes the nature of these paths and steps that were taken to reduce the amount of current flowing through them.

A generalized schematic of the instruments and possible shunt paths is shown in Figure B.24. For present purposes the nerve response amplifiers can be lumped together in a single box and only the output op-amp of the stimulator need be considered. The stimulator is connected between two electrodes, labeled p and n, through which currents i_+ and i_- flow. Three possible current paths, each a bold line ending in an arrow point, are depicted in the Figure. The box labeled Z represents pathways linking a node or nodes in the response amplifiers with the stimulator ground. The path labeled i_n passes through just the salt water (and tissue, if present) and represents the nominal or intended path for current flow. Hence in the ideal case $i_+ = i_- = i_n$.

The other two current paths, i_{sc} and i_{sd} are shunt paths. Let's consider first how current might flow in the i_{sc} path. Recall that if the stimulator op-amp is not saturated or slewing, the feedback requires that $i_- = -v_{in}/R_t$ and that electrode n is

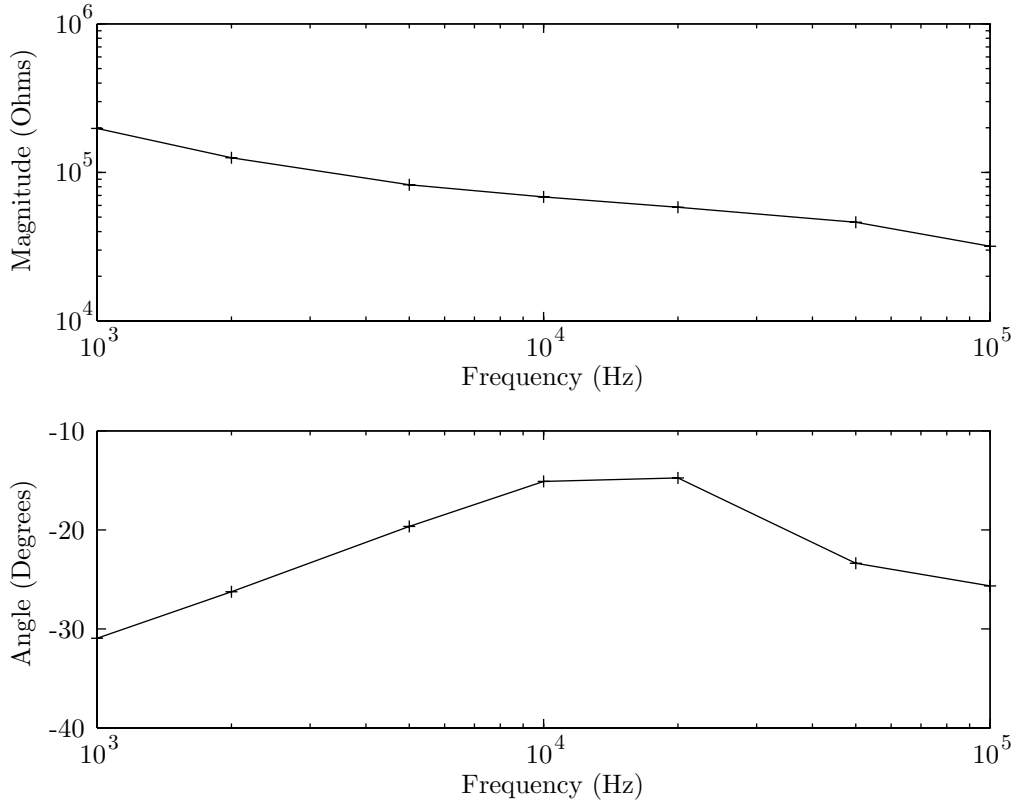

Figure B.23: Impedance magnitude and phase of electrode D0 on array AEG2. Electrode D0 is a 10μm diameter disk of indium-tin-oxide plated with platinum black at .3μA for about five seconds.

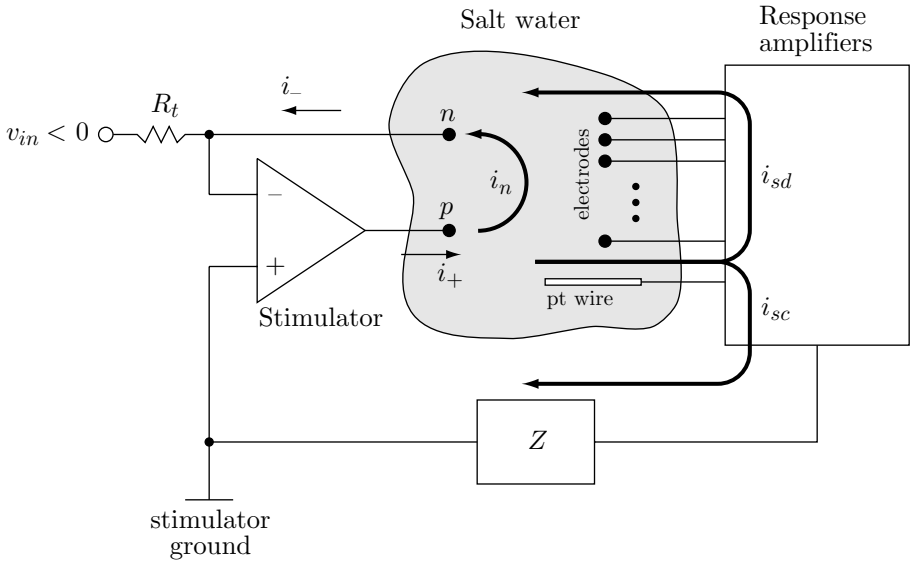

Figure B.24: Possible paths for stimulation current. i_n is the intended path; i_{sc} and i_{sd} are shunt paths.

at the stimulator ground potential. When $v_{in} < 0$, i_- and i_+ will be positive, raising the potential everywhere in the bath (relative to the stimulator ground) except at electrode n. This rise in potential may cause a current i_{sc} to flow if a sufficiently low impedance path between the amplifier and stimulator ground is available. The simplest such case would occur if the stimulator and recording amplifiers shared the same ground and if the recording amplifiers were configured for single-ended measurements. In this case the platinum wire would provide a direct connection to the stimulator ground.

In anticipation this outcome, the response amplifiers were initially configured for differential recording, with the platinum wire—which served as a common reference for all electrodes—connected to a high impedance op-amp input. Substantial shunt currents in the i_{sc} path were discovered in spite of this precaution. These were revealed when simultaneous measurements of the stimulator branch currents showed a transient period where $i_+ > i_-$. In this early version of the instrument, the stimulator and recording amplifiers shared the same ground, and analog multiplexers were used to select amplifier inputs as shown in Figure B.25a. The channel capacitances in the analog multiplexers provided low impedance paths to ground. All 64 such capacitances (8 multiplexers $\times$ 8 channels each) in parallel resulted in a significant shunt current, which appeared as an overshoot in the i_+ waveform. Consistent with this model, the overshoot systematically decreased as multiplexers were each replaced by

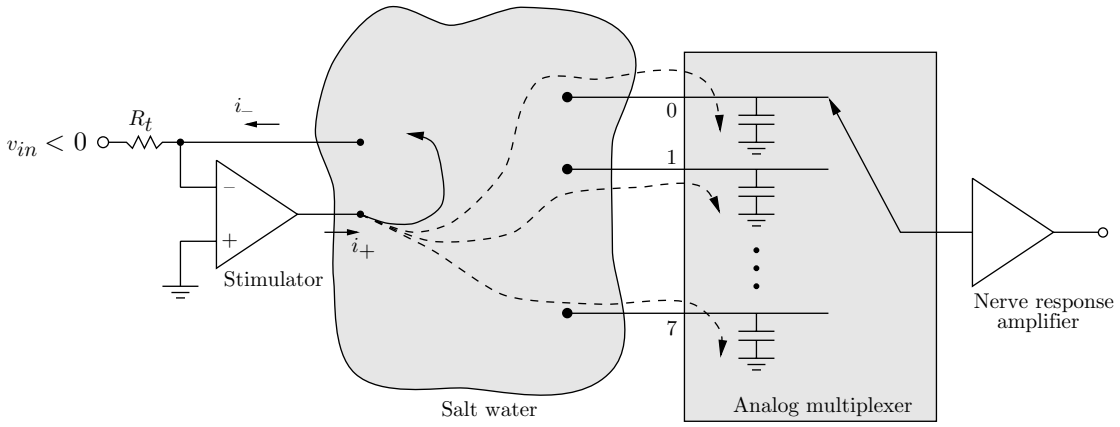

(a)

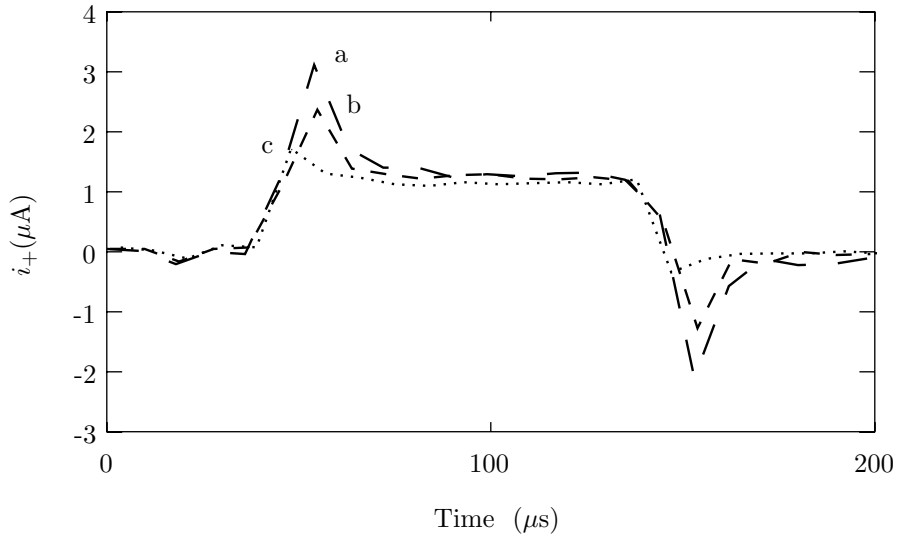

(b)

Figure B.25: Shunt currents with differential recording but a shared ground. (a) Schematic diagram of the instruments. The solid line represents the intended stimulation current, the dashed line is the shunt current. The capacitors represent parasitic channel capacitances to ground in the analog multiplexer. (b) Plot illustrating the dependence of the measured i_+ current on the number of multiplexers connected to the bath. The peak overshoots for three cases are labeled: a - four multiplexers; b - 2 multiplexers; c - no multiplexers.

a wired connection from one electrode to the preamplifier input. This is shown in Figure B.25b.

Isolating the stimulator from the response amplifiers, so that the two use separate grounds, reduces if not abolishes the i_{sc} component. Even with all eight multiplexers connected, the measured i_- and i_+ current components were equal. This approach required that care be taken to keep the two grounds physically separate to reduce parasitic capacitance between them. In the physical arrangement of the circuits, the stimulator was placed atop an insulating platform, several centimeters above the recording ground plane.

The second path for shunt current, labeled i_{sd} in Figure B.24, is more subtle. This path is taken by current which flows into the response amplifier through some electrodes and back out through others. The shunting cannot be detected from measurements of the stimulator branch currents since isolation ensures that the branch currents are equal. However, the relatively large channel capacitances in the analog multiplexer might be expected to provide viable paths as they did in Figure B.25, but instead joining different electrodes via the recording ground. The electro-mechanical relays in Figure B.12 were introduced for this reason. The parasitic capacitances to ground associated with these were measured at 1-2pF, as opposed to several tens of pF for the analog multiplexers.

B.5.3 Summary of ground connections

The observations of Section B.5.1 suggest using the ground connection scheme illustrated in Figure B.26. To eliminate electrostatic pickup, the Faraday cage is connected to the shield around the power supply wires, which is in turn connected to earth. As mentioned at the beginning of section B.5.1, the power supply ground "com1" is connected to earth. To minimize the potential for ground loop pickup, the earth-connections from the computer D/A and plug-in power supply will be kept in close proximity to one another, as shown in the Figure. Finally, a branched ground connection is used, wherein all grounds are established at a central "hub".

B.6 Dynamic response of current source output network

The stimulator current source and output network are redrawn in Figure B.27, with the op-amp circuit replaced with an ideal current source. To simplify analysis, the electrodes have been modeled with a resistor R_L.

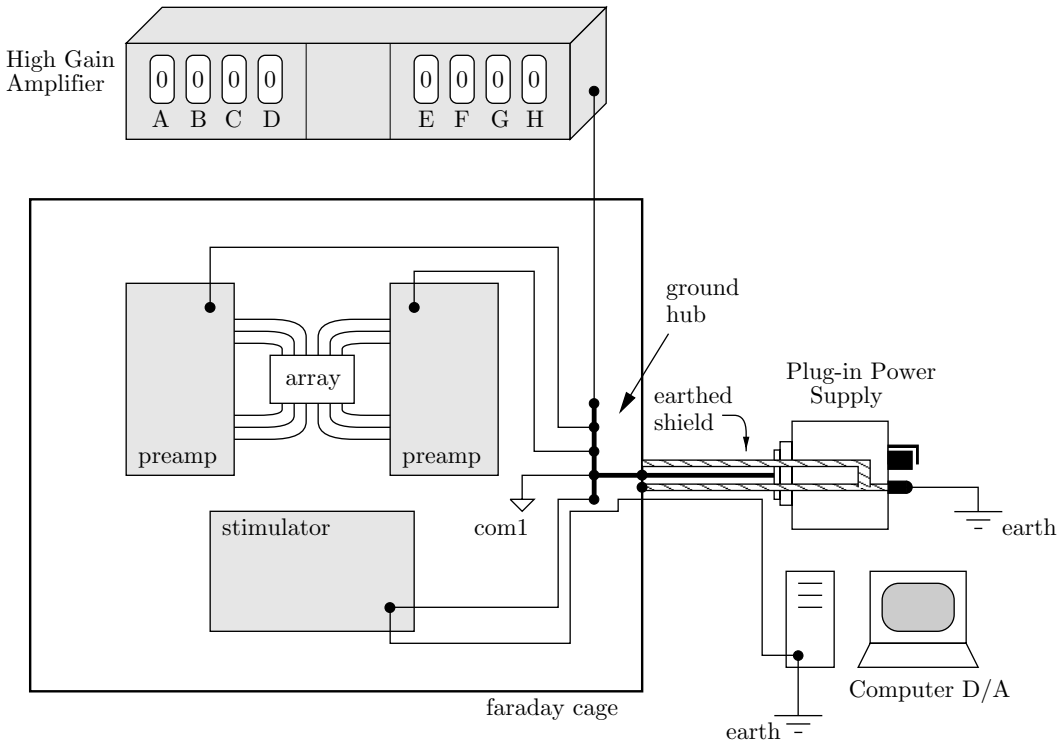

Figure B.26: The ground connection scheme used.

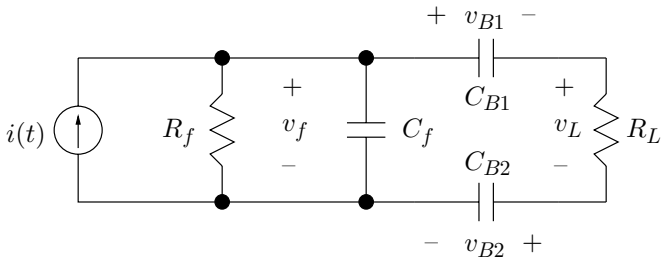

Figure B.27: Ideal current source and output network.

B.6.1 Derivation of transfer function and natural frequencies

Here are the fundamental circuit equations for the network:

$$i(t) = \frac{v_f}{R_f} + C_f \frac{dv_f}{dt} + C_B \frac{dv_{B1}}{dt},$$

$$\frac{v_L}{R_L} = C_B \frac{dv_{B1}}{dt} = C_B \frac{dv_{B2}}{dt},$$

$$v_f = v_L + v_{B1} + v_{B2}.$$

Taking the derivative of the first equation and solving the system for d_i/dt yields

$$\frac{di}{dt} = (C_f)\,\frac{d^2 v_L}{dt^2} + \left(\frac{1}{R_L \| R_f} + \frac{2C_f}{R_L C_B}\right)\frac{dv_L}{dt} + \left(\frac{2}{R_f R_L C_B}\right) v_L.$$

Converting to the frequency domain, and noting that the load current i_L is the quotient of the load voltage v_L and load resistance R_L, we find that the transfer function from stimulation current to load current is

$$\frac{I_L(s)}{I(s)} = \frac{s/R_L C_f}{s^2 + \left(\frac{1/C_f}{R_L \| R_f} + \frac{2}{R_L C_B}\right) s + \frac{2}{R_f C_f R_L C_B}}$$

The natural frequencies of this circuit are the roots of the characteristic equation,

$$s^2 + \left(\frac{1/C_f}{R_L \| R_f} + \frac{2}{R_L C_B}\right) s + \frac{2}{R_f C_f R_L C_B} = 0.$$

These roots are

$$s = -\left[\frac{1/2}{(R_L \| R_f) C_f} + \frac{1}{R_L C_B}\right] \pm \sqrt{\left[\frac{1/2}{(R_L \| R_f) C_f} + \frac{1}{R_L C_B}\right]^2 - \frac{2}{R_f C_f R_L C_B}}.$$

The resistance R_L represents the series combination of two electrodes and the bath. This should be somewhere between 100 kΩ and 1 MΩ. The feedback resistor R_f is 10 MΩ. If we approximate $R_L \ll R_f$, the roots of the characteristic equation can be written

$$s \approx -\left(\frac{1/2}{R_L C_f} + \frac{1}{R_L C_B}\right)\left[1 \pm \sqrt{1 - \frac{2}{\left(\frac{R_f C_B}{R_L C_f}\right)\left(\frac{1}{2} + \frac{C_f}{C_B}\right)^2}}\right].$$

Noting further that C_f is 10pF and C_B is 10nF, we see that $C_f \ll C_B$. This being the case, the term under the radical in the expression above is very close to 1. Taking a first order approximation of the square root yields,

$$s \approx -\left(\frac{1/2}{R_L C_f} + \frac{1}{R_L C_B}\right)\left[2 - \frac{1}{\left(\frac{R_f C_B}{R_L C_f}\right)\left(\frac{1}{2} + \frac{C_f}{C_B}\right)^2}\right]$$

$$\text{OR} \quad -\left(\frac{1/2}{R_L C_f} + \frac{1}{R_L C_B}\right)\left[\frac{1}{\left(\frac{R_f C_B}{R_L C_f}\right)\left(\frac{1}{2} + \frac{C_f}{C_B}\right)^2}\right]$$

Finally, making use again of the approximations $R_L \ll R_f$ and $C_f \ll C_B$, we get

$$-\frac{1}{\tau_1} = s \approx -\frac{1}{R_L C_f} \qquad \text{OR} \quad -\frac{1}{\tau_2} = s \approx -\frac{2}{R_f C_B}$$

Fast Response Slow Response

B.6.2 Interpretation of circuit natural frequencies

The retina is stimulated using rectangular current pulses, so it is useful now to consider the step response of the load current. Rather than doing a full solution, a bit of circuit intuition will be used to predict the answer, and then comparisons with measurements made to check the reasoning.

Fast natural frequency

First, consider the "fast" response, where the dynamics are governed by the time constant $\tau_1 = R_L C_f$. On these time scales, the larger blocking capacitors C_B are essentially short circuits, and the current is used to charge up C_f. The (now) parallel combination of R_L and R_f is dominated by the smaller R_L, so the dynamics are essentially those of the simplified circuit of Figure B.28a. The step response of the current $i_L(t)$ is given by

$$i_L(t) = \mathrm{I}\left(1 - e^{-t/R_L C_f}\right)$$

This response is drawn in Figure B.28b. Part c of the Figure illustrates the relatively good agreement between predicted and measured responses for R_L=240kΩ and C_f=100pF.

Note that a larger capacitor C_f was used for this measurement than the normal value of 10pF (see Figure B.7). For C_f=10pF, the step response of the current does not resemble an exponential function, but instead exhibits a rapid rise time (less than half a microsecond) and a 20% overshoot. A second, and perhaps related, discrepancy is evident in the table of stimulator performance specifications given at the beginning of section B.2.5. Below the table, it is noted that the 10%-90% rise time was found to vary with the transconductance-setting resistor R_t. Neither the non-exponential step response nor the variation of rise time with R_t is predicted by the model of Figure B.27. This is most likely because for small feedback capacitances the operational amplifier circuit is not well-modeled by an ideal current source.

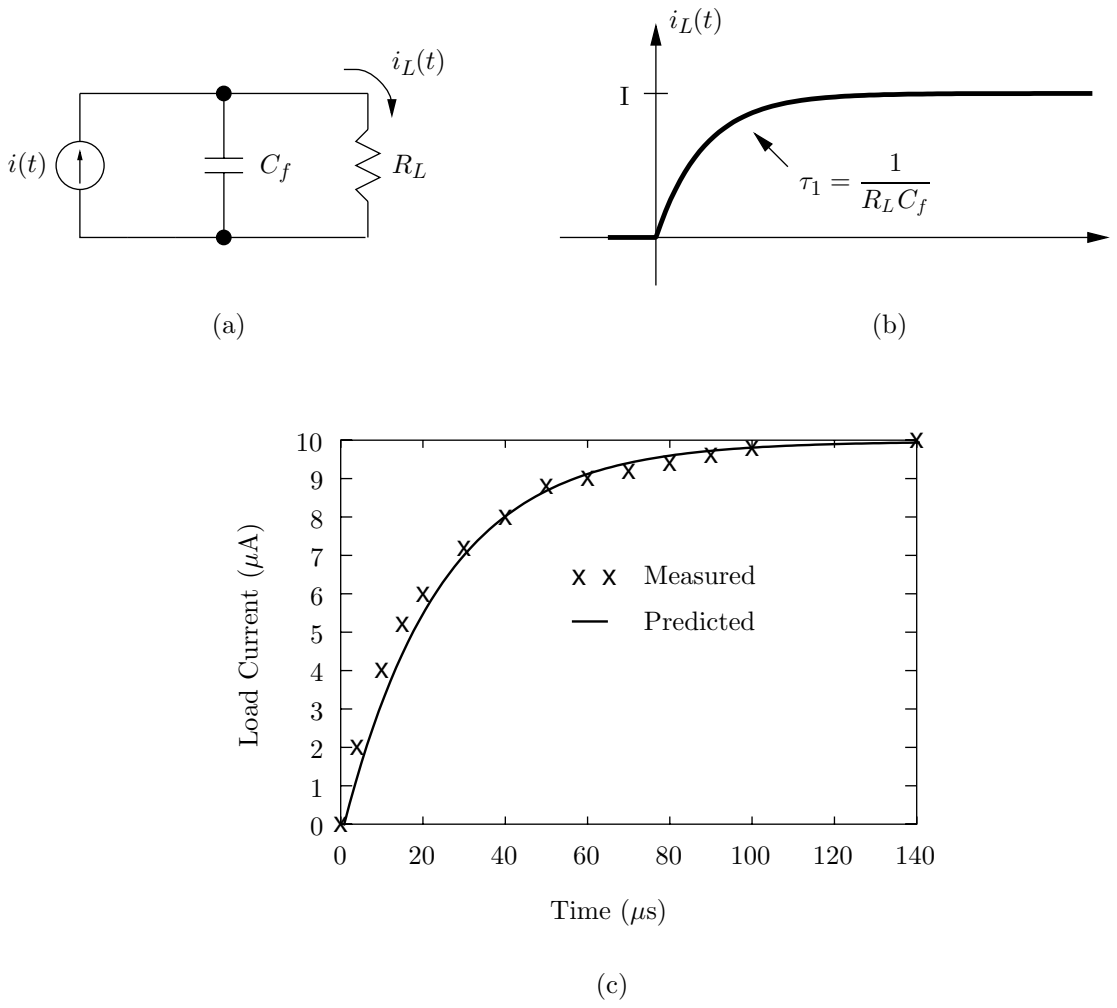

Figure B.28: Fast natural frequency: (a) circuit; (b) predicted step response; (c) and comparison of predicted and measured step responses.

Slow natural frequency

Now consider the "slow" response, where the dynamics are governed by the time constant $\tau_2 = \frac{1}{2}R_f C_B$. Looking at the circuit containing the ideal source and full output network, we recognize that, at DC, the load current must be zero since the blocking capacitors look like open circuits. We associate this second time constant with the slower discharging of the C_B's when the total charge delivered by a stimulation waveform is nonzero. In this case, C_f can be assumed to always be at its "final" voltage, since its dynamics are very fast on the time scale of interest here. We can therefore use a *quasistatic model* and treat C_f as an open circuit. Combining the two series C_B's, we redraw an approximate circuit in Figure B.29a.

The load current $i_L(t)$ is given by

$$i_L(t) = I_o e^{-t/\frac{1}{2}(R_f+R_L)C_B}$$

or, if we invoke the approximation $R_L \ll R_f$,

$$i_L(t) \approx I_o e^{-t/\frac{1}{2}R_f C_B}$$

where

$$I_o = \frac{2\mathrm{Q}}{(R_f + R_L)}$$

and Q denotes the amount of leftover charge delivered by the stimulus. This approximate response is shown in Figure B.29b.

Figure B.29c compares the measured (black) and predicted (superimposed white) responses of the load current when an unbalanced charge Q=9nF is delivered by a brief pulse of 10μA current. Again, the agreement between the theoretical and measured responses is satisfactory.

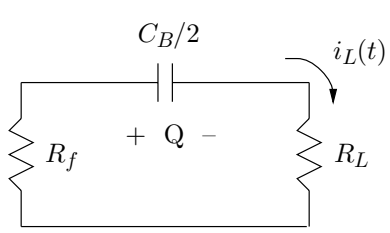

(a)

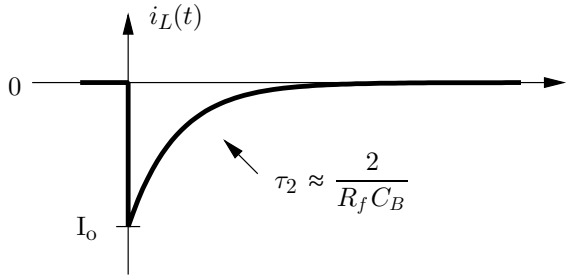

(b)

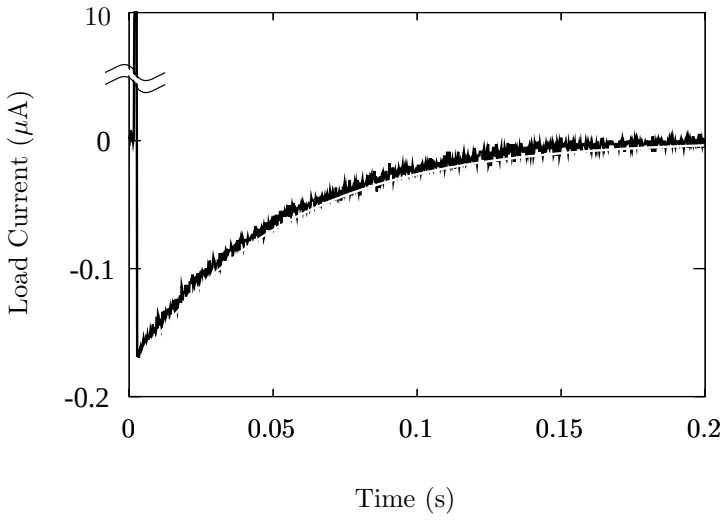

(c)

Figure B.29: Slow natural frequency: (a) approximate circuit; (b) step response; (c) comparison of predicted and measured step responses. In (c), the measured step response for R_L=240kΩ, $C_B = .01\mu$F is drawn in black and the predicted response is superimposed in white.

Appendix C

Investigations of Stimulus Artifact

C.1 Introduction

All experiments involving electric stimulation and recording suffer to some degree from stimulus-induced distortion of the response signal. The distortion is called the *stimulus artifact*, and is alternately referred to as the stimulus artefact or shock artifact.

Stimulus artifacts make it difficult if not impossible to study neural responses to electric stimulation. Consider for example Figure C.1, which depicts a recording that was taken early in the experimental work of this thesis. The artifact is large compared to a typical action potential, and substantially outlasts the stimulus. The artifact is large enough and long enough, in fact, that the amplifier is saturated during the interval where neural responses are expected to occur*. Thus no useful data can be obtained from this recording.

Stimulus artifacts can arise from any of a large number of sources. This chapter details efforts to identify these sources in the instrument system (see Chapter 2 and Appendix B) and to reduce their impact. An alternate approach, wherein signal processing is employed to discover response signals in artifact-contaminated recordings, was not pursued due to the not infrequent occurrence of amplifier saturation.

The material is presented in more or less the order in which the different approaches were tried. These efforts were not exhaustive, and many did not lead to a significant improvement in signal quality, but they did, along with a sampling of the relevant literature, help me to formulate a fairly broad view of the problem. This view is presented at the end of the chapter.

*Unlike light-generated ganglion cell responses (which lag the stimulus onset by tens to hundreds of milliseconds), electrically generated ganglion cell responses can be initiated within a millisecond.

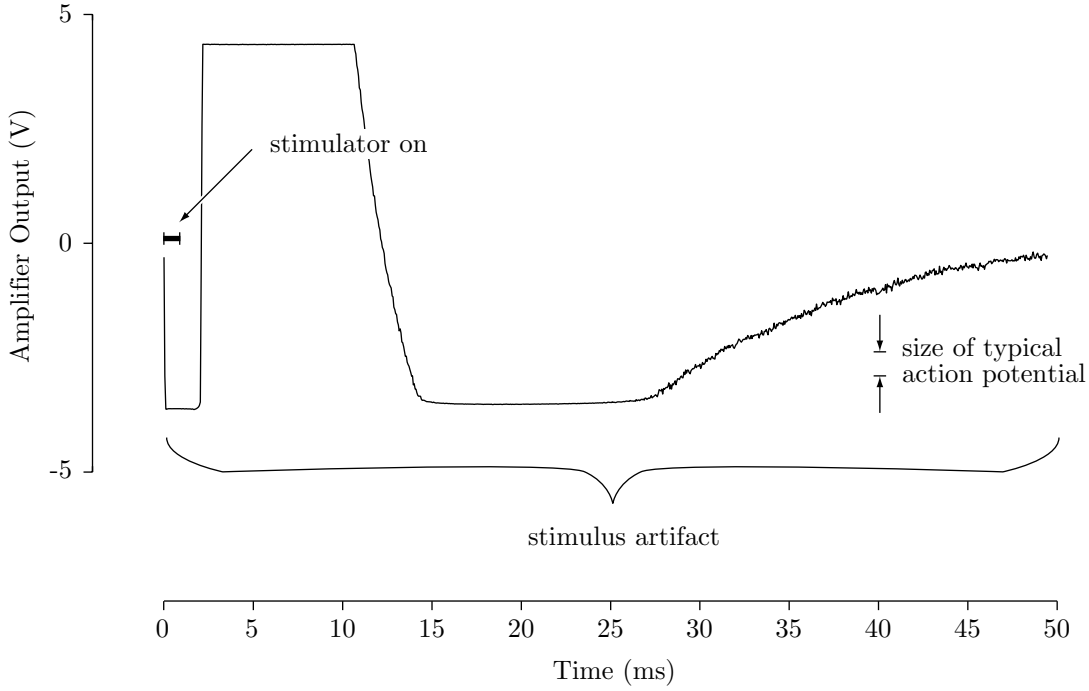

Figure C.1: Example stimulus artifact.

C.2 Response amplifier considerations

C.2.1 Saturation and filters

The potential changes produced at the response amplifier input by electric stimulation are often vastly larger than the expected response signal. These unusually large inputs drive the response amplifier into saturation, where the amplifier's behavior can be unpredictable. The suggestion arises that substantial length is added to the artifact by the amplifier circuit, as a result of being driven so far beyond its dynamic range (Freeman, 1971; McGill et al., 1982; Ranck, 1981; Sherman-Gold, 1993). The additional length might be attributed to erratic saturation behavior of individual op-amp chips or to slow discharging of high pass filter capacitors.

To see how high pass filters can add length to stimulus artifacts, consider the amplifier topology used for this thesis. A passive high-pass filter is placed prior to the final stage of x25.4 gain to block DC offsets from earlier stages, as shown in Figure B.16. Suppose now that a stimulus lasting 300μsec is applied, and that it is sufficient to saturate the input to the high-pass filter for the entire duration of

the stimulus. The saturation voltage driving the high-pass filter is roughly 5 volts (i.e. the positive supply rail). Since the time constant of the high-pass filter is much larger than than the interval of interest (8.2msec compared with 300μsec), the charge deposited on the capacitor will be approximately

$$Q = \frac{5\text{V}}{82\text{k}\Omega} \times 300\mu\text{sec} = 18.3\text{nC}.$$

If, when the stimulus is over, the output of the early gain stages returns immediately to zero, the charge on .1μF capacitor will result in a voltage

$$V = \frac{\text{Q}}{\text{C}} = \frac{18.3\text{nC}}{0.1\mu\text{F}} = 0.183\text{V}.$$

This voltage is sufficient to saturate the final gain stage, and decays with a very slow time constant of 8.2ms.

Note that the same principle could be applied to low-pass filters in the circuit, though in practice the time constants associated with such filters are usually fast enough to be of no consequence.

C.2.2 Sample and hold

Saturation problems and filter transients can sometimes be eliminated by inserting a sample and hold into the amplifier circuit (Freeman, 1971; Roby and Lettich, 1975; Sherman-Gold, 1993). Such a circuit is switched into "hold" mode just before stimulation, to store the baseline voltage and prevent large signals from being passed to later filters and stages of gain. When the stimulus is over, the circuit is switched back to "sample" mode, hopefully allowing the neural response signals to pass undistorted.

The amplifiers used in this thesis contain a sample and hold circuit, placed at the output of the x10 pre-amplifier (see Figure B.11 and Section B.4.3). Measurements such as that shown in Figure C.2 revealed that the artifact persisted even when the sample and hold circuit was used. Thus the artifact must have been present at the input to the sample and hold circuit, and cannot be attributed to filter transients or saturation of op-amps in the higher gain stages.

Incidentally, sample and hold circuits are sometimes employed even when the artifact ends promptly with the stimulus. The reason is that it eliminates transients from the signal which might be misinterpreted as physiologic signals by systems using automated event extraction schemes (Freeman, 1971; Minzly et al., 1993; Roby and Lettich, 1975).

C.2.3 Preamplifier input

The measurements above do not rule out the possibility that artifacts were generated in the pre-amplifier which precedes the sample and hold circuit. Direct examination

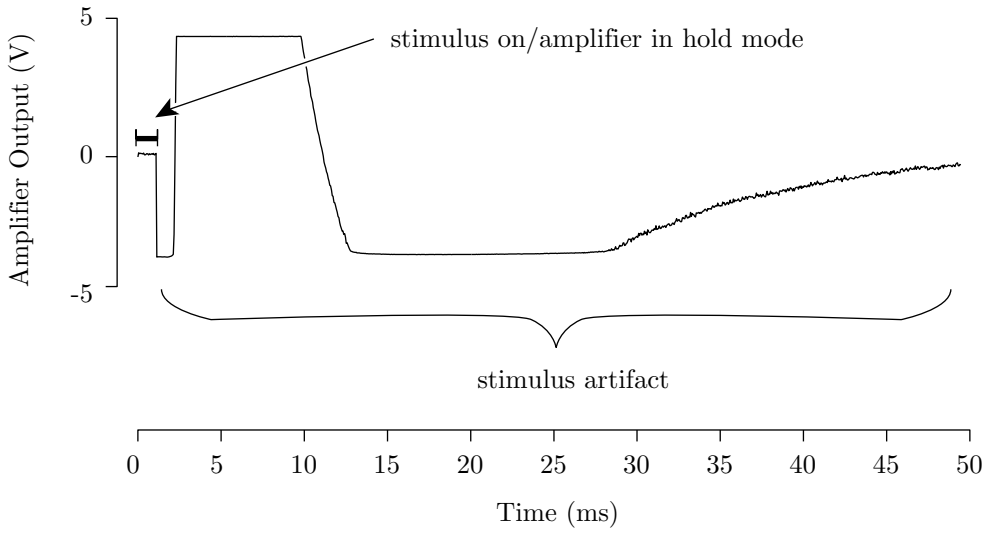

Figure C.2: Stimulus artifact, with sample and hold circuit activated.

of the preamplifier outputs, however, revealed that the preamplifiers did not saturate even when long stimulus artifacts were observed. Hence the long artifact must have been present at the preamplifier input.

Each preamplifier has a .01μF capacitor at its input (see Figure B.13) which might contribute to the artifact. These capacitors prevent DC bias currents—needed by the AD711 op-amps' JFET inputs–from flowing through the electrodes, and also to minimize offset drift. In a few tests a MOSFET input device (LMC6081) was used instead of the AD711, and a direct connection was made from the recording electrode to the op-amp input. Stimulus artifacts were not substantially reduced, indicating that the input capacitor was not a primary contributor.

C.3 Stimulator-amplifier coupling

Stimulators are used to create electric fields in biological tissues, typically with the intention to alter the membrane potentials of neurons. But these fields also produce voltage drops across the inputs to neural response amplifiers, even when the stimulator and amplifier are powered from isolated supplies. This unintended and undesirable effect provides the simplest explanation for stimulus artifacts.

Artifacts can also be caused by currents flowing in parasitic coupling paths be-

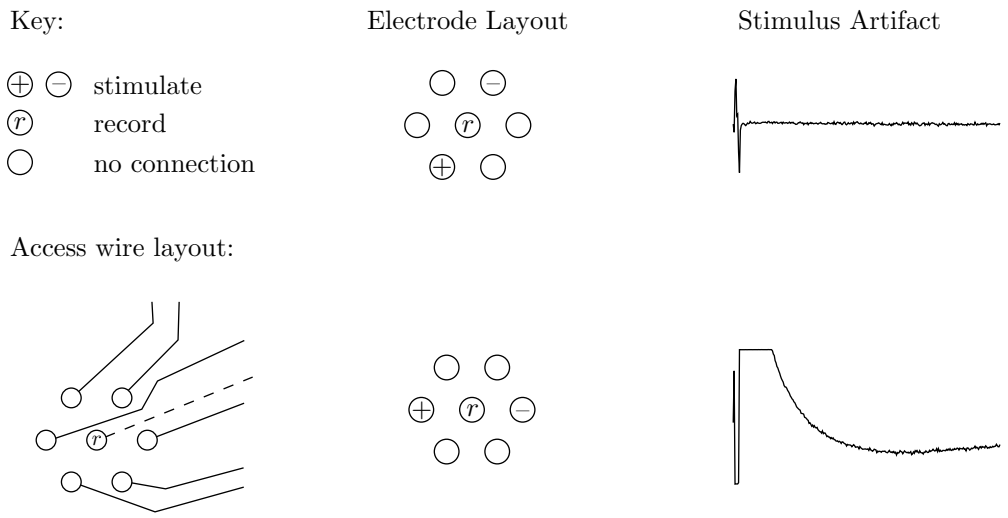

Figure C.3: Stimulus artifacts (right column) for two bipolar stimulating pairs symmetrically arranged with respect the the recording electrode (middle column). The horizontal and vertical scales are the same for the two artifacts, which were both recorded at electrode r.

tween the stimulating and recording circuits (McGill et al., 1982; Ranck, 1981), as appears to have been the case in the measurements of Figure C.3. The Figure depicts two measurements of the stimulus artifact, each using a unique pair of stimulating electrodes. The stimulus artifacts recorded at electrode r (measured with respect to a distant ground) were substantially different despite the symmetric layout of the stimulating bipolar electrode pairs with respect to the recording electrode.

Though the exposed electrodes were laid out symmetrically, the wires which provided access to them were not. As shown in the lower left of Figure C.3, some stimulating electrode access wires (solid) were closer to the recording electrode wire (dashed) than others. When the artifact was largest, the stimulating electrode wires were closest to the recording electrode wire.

This observation gave rise to the hypothesis that stimulus artifacts were produced by leakage currents flowing between the stimulating and recording electrode wires. Additional measurements supported this hypothesis. For example, shielding a recording electrode's access wires led to a dramatic reduction in the strength of the artifact. This shielding experiment is described in Figure C.4. Also, a SPICE model incorpo-

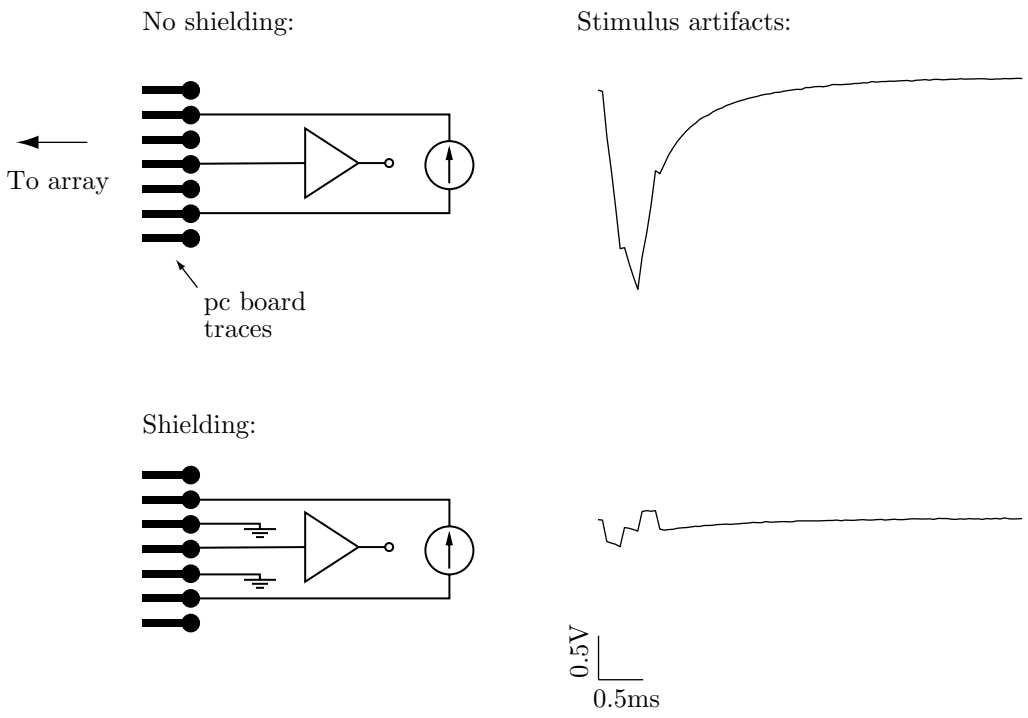

Figure C.4: Stimulus artifacts with and without shielding of the recording electrode. Shielding was achieved by connecting the PC board wires adjacent to the recording electrode wire to the recording ground (earth). These PC board wires map to wires on the electrode array as described in Section 2.3.3. Note that the shielding could have also altered the field distribution in the medium, though this effect should have been limited since the stimulator was isolated from the recording ground.

rating the hypothesized leakage pathways provided a reasonably accurate prediction of the measured artifact, as shown in Figure C.5b. The simulated artifact tracks the measured artifact quite well during the stimulus—a 200μs per phase biphasic pulse pair with an intra-phase delay of 200μs (not shown)—but overshoots the baseline (and perhaps decays back to zero) more rapidly than the measured artifact during the 1-5ms interval.

The general layout of the circuit model appears in Figure C.5a. The parasitic leakage paths between wires for each of the stimulating electrodes (B5 and A2 in the Figure) and the recording electrode (B6) were characterized by placing a drop of medium on the polyimide above the wires, being careful not to immerse the exposed electrode surfaces. Small sinewaves between 1kHz and 100kHz were applied, and the resulting data qualitatively fit to a parallel RC model for the wet polyimide. The bathing medium assumed to be isopotential.

Each electrode impedance was modeled by an access resistance in series with a parallel RC representing the electrode-electrolyte interface. The component values were determined by measuring the load voltage as a 2ms step of current was injected through a pair of electrodes. A full schematic of the SPICE model circuit, incorporating the electrode impedances and the current source output network (see Figure B.7) is shown in Figure C.6.

It is interesting to note that the circuit topology of Figure C.5a will produce no artifact if the leak impedances at the top and bottom of the circuit are equal. This a consequence of the symmetry of the circuit: if leak impedances are equal and the B5 and A2 impedances are equal, then no potential drop will be produced across the B6 impedance. One might be able to make practical use of this observation if equal electrode and leakage impedances could be assured, and if the shunt currents in the leak paths were acceptably low. I did not attempt this approach, since there was a straightforward way to raise the leak impedances.

The arrays used in the measurements above had a 1μm thick layer of polyimide insulation. This thickness was raised to 10μm to decrease the capacitance of the insulating layer. Furthermore a silicon nitride layer was added (see Figure 2.4) to provide a barrier to ionic (resistive) current flow. These changes substantially raised the leak impedances, which were so large as to be indistinguishable from the driving impedance of the dry array (i.e. no fluid to provide a leak path) in parallel with a 10x scope probe (9MΩ || 20pF). More importantly, the changes led to a substantial decrease in the artifact duration, as illustrated in Figure C.7.

With the improved isolation, stimulus artifacts usually ended abruptly when the stimulus was over. At least in salt water. Unfortunately, the artifacts grew again when a retina was placed on the array. To further reduce coupling in the tissue, the electrodes were divided into separate clusters for stimulation and recording which were spaced several hundred microns apart (see Figure 2.2). Care was also taken to run the access wires for stimulation and recording to opposite edges of the array, to reduce the chances for any additional leakage currents to flow between these.

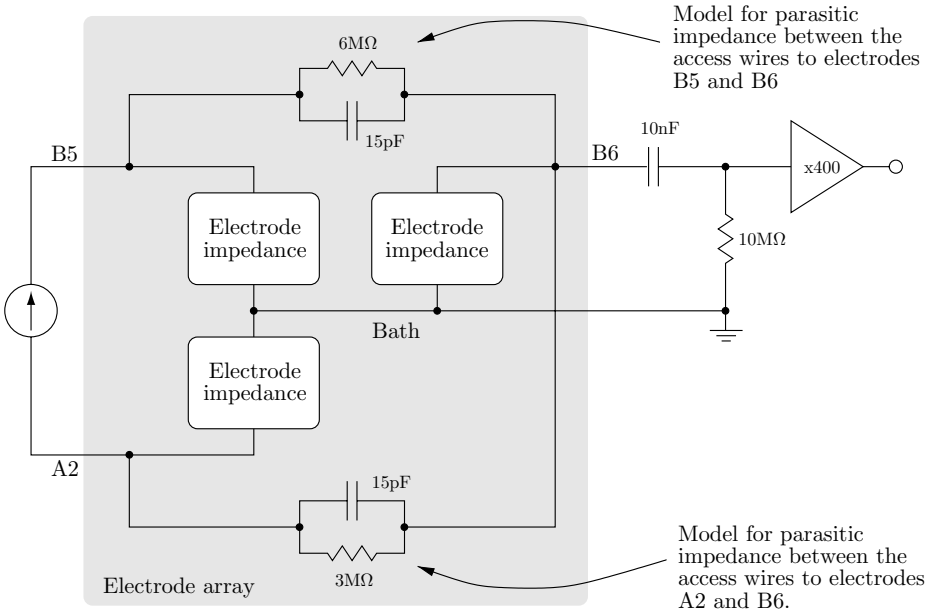

(a)

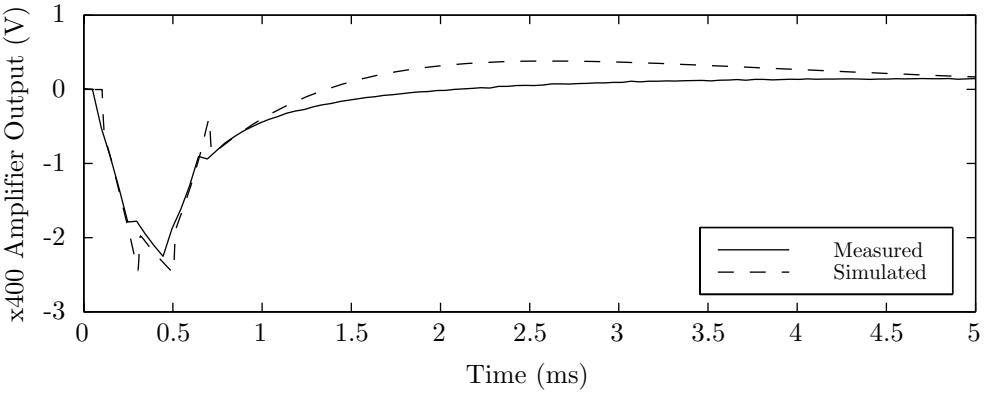

(b)

Figure C.5: A SPICE simulation reproduces the stimulus artifact to a fair degree. (a) Simplified circuit; (b) Comparison of simulated and measured artifacts. For these measurements the signal was examined prior to the final high pass filter and 25.4x gain (see Figure B.16), to avoid artifact contributions from amplifier saturation or filter transients.

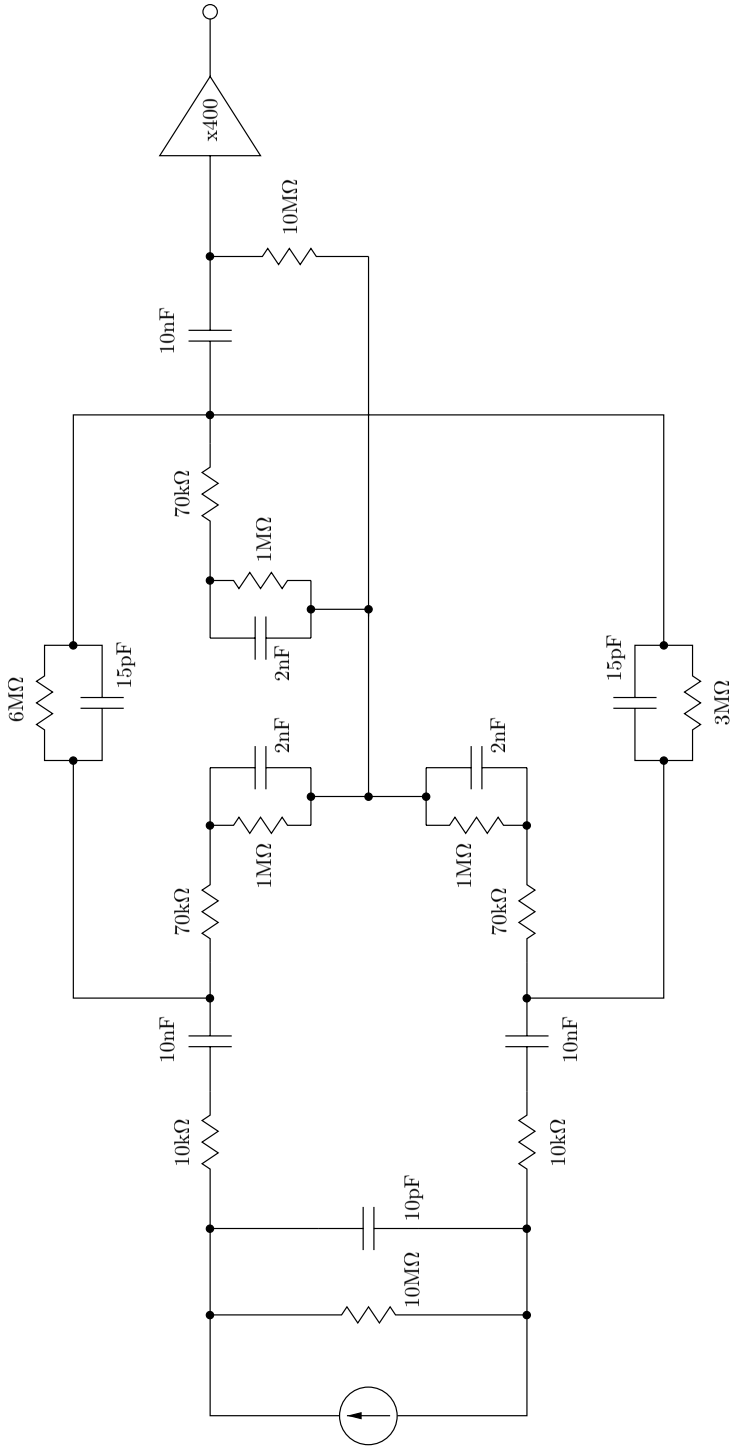

Figure C.6: Spice model for stimulus artifacts.

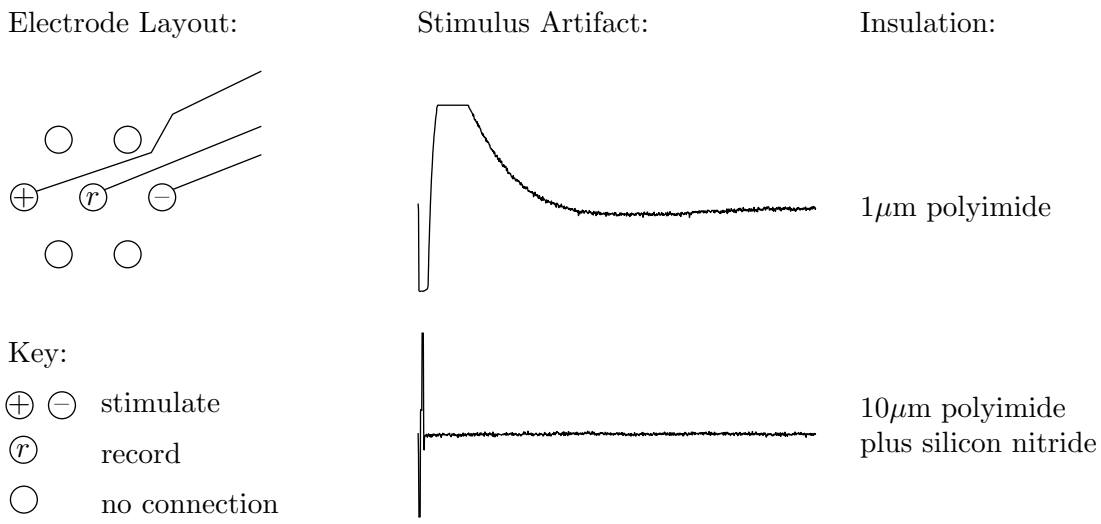

Figure C.7: Stimulus artifacts with old and new array insulation.

C.4 Stimulator considerations

C.4.1 Offsets and supply coupling

A simple control measurement was often performed, wherein artifacts were measured while applying a zero-amplitude stimulus. Sometimes, surprisingly, substantial artifacts were recorded under these conditions. Two remedies helped reduce artifacts in these cases. First, offsets in the current source—which can result in steps of stimulation current when the stimulation waveform is set to zero—were nulled using the potentiometers on the stimulator (see Section B.2.3). Second, these artifacts could sometimes be reduced by running the preamplifiers from a different power supply from the one used to for the remaining non-isolated instruments (i.e. the response amplifier and the non-isolated side of the stimulator). Though both supplies shared a common ground, it is possible that the change reduced coupling through positive and/or negative supply rails.

C.4.2 Series coupling capacitors

The stimulator has capacitors in series with its outputs to protect electrodes from DC current. If the stimulation current waveform is not charge-balanced, there will be charge left on these series coupling capacitors at the end of the stimulus. This charge will decay through a loop consisting of the two series capacitors, the electrodes, and the output impedance of the current source (see Section B.6.2). The dynamics of the charge decay are potentially quite slow, and the discharging current functions like additional stimulation current. Might this charge decay account for the slowly decaying artifact?

Generally speaking, no, since charge-balanced pulses were almost always used. In a few cases a more direct test was performed wherein the capacitors were short circuited. The change had no effect on the stimulus artifact. Occasionally monophasic pulses were applied, and artifacts were usually larger for these than for charge-balanced biphasic pulses. The series coupling capacitors may played a significant role under these conditions. On the other hand, the capacitance of the stimulating electrodes themselves must also be reckoned with.

C.5 Electrode capacitance

C.5.1 Stimulating electrodes

Because stimulating electrodes have capacitive as well as resistive properties (Kovacs, 1994) they too can accumulate charge during stimulation. If any charge is left on the electrode capacitance following stimulation, it will decay away slowly across the electrode resistance.

The simple circuit model in Figure C.8 illustrates this idea. With the stimulator in turned on (Figure C.8a) current passes through the electrode and charges the electrode capacitance C_e. Even when (in fact, *particularly* when) a charge-balanced stimulation waveform is used there will be net charge on C_e at the end of stimulation, due to leakage through the electrode resistance R_e. This net charge then decays through the electrode resistance after the stimulator has been turned off, as shown in Figure C.8b.

This decaying charge can be observed by closing a switch across the electrodes immediately following stimulation, as in Figure C.8c. If the measuring resistance R_m is smaller than the electrode resistance R_e, closing the switch provides an effective shunt path for discharging of the electrode capacitance. Figure C.8 shows the results of making such an observation.

The decaying charge creates electric fields in the fluid (or in parasitic pathways between stimulator and amplifier) which may be picked up as artifact. This this contribution to the artifact might be reduced by shorting the stimulating electrodes to each other following stimulation, as in Figure C.8 (though care should be taken

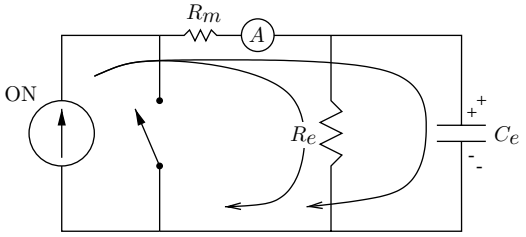

(a) Leaky charging of the electrode during stimulation.

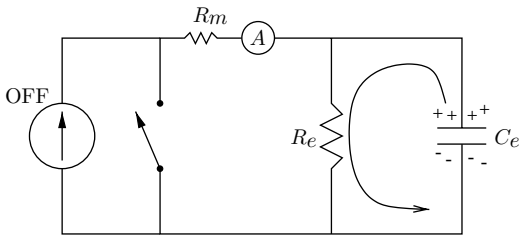

(b) Discharging through electrode resistance after stimulator has turned off.

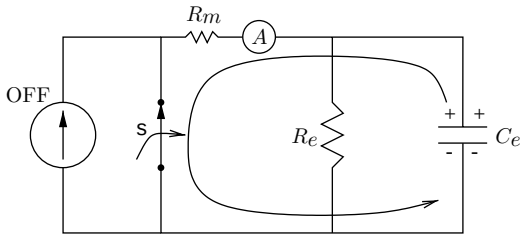

(c) Discharging through measuring resistance after switch closes.

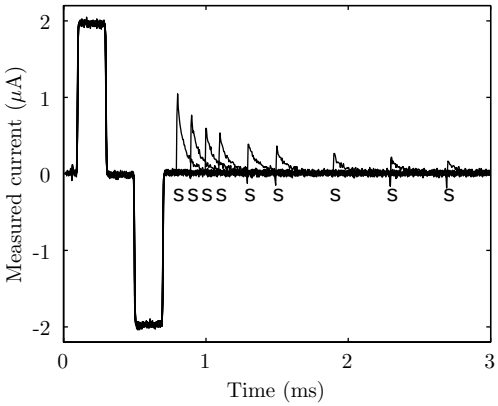

(d) Overlay of measurements with switch closed at several different times (each marked by an s). Decaying electrode charge shows up as deflections in the current coincident with the switch closings.

Figure C.8: Circuit model for and measurements demonstrating decay transients on stimulating electrodes.

not to discharge the electrodes through the stimulator's series coupling capacitors). Stimulators which do this have been reported previously (e.g. Del Pozo and Delgado (1978))), though the motivation was usually to preserve the electrodes from corrosion rather than to reduce stimulus artifacts. A related approach would be to short stimulator outputs to ground following stimulation.

In a small number of measurements these two approaches were found to lead to larger rather than smaller artifacts. It may be that DC potentials on stimulating electrodes (due to electrochemical batteries at the electrode-electrolyte interfaces) may have compounded the problem, or that other sources—that these techniques would not remedy—dominated the artifacts.

C.5.2 Recording electrodes

Recording electrodes also have capacitance and hence can also accumulate charge. Some attempts were made to use electronic switches to briefly short recording electrodes to ground following stimulation, to relieve them of any lingering charge. If decaying charge on the recording electrode was the primary source of stimulus artifacts, this technique might allow one to record undistorted nerve responses.

While simple in principle, implementation of this technique proved quite challenging and ultimately did not solve the problem. For example, the problem of switch feedthrough had to be addressed. To try and null out the channel charge, the switch was implemented with two MOSFETS—a p-channel device and an n-channel device. By design, opening or closing the switch required that the two devices be driven with opposite polarity steps, providing some cancellation of channel charge. Furthermore, the amplitude of control step on one of the devices could be manually adjusted to optimize artifact rejection. Trimpots were provided for adjustment of both the gate-to-source and gate-to-substrate voltages on this device.

Upon deployment of the switches, stimulus artifacts became time-variant. A stimulus applied at 1Hz would produce artifacts of different sizes upon each presentation. Adjusting the trimpots provided only momentary reduction of stimulus artifacts.

Then again, shorting to *ground* may not have been the best idea to begin with, since electrode-electrolyte interfaces generate a nonzero battery potential (100mV in one measurement) which can be drift-prone. Perhaps this was the source of time-varying nature of the artifact in the previously described set of measurements. A further effort was undertaken to sample the battery potential prior to stimulation and then lock the amplifier input node to this potential during stimulus application. This circuit was not successful either—artifacts still varied with time and could not be effectively nulled out.

C.6 Reducing stimulus artifacts: an overview

Though the investigations described in this appendix made possible a variety of useful measurements (see Chapters 2 and 3), they by no means solved the problem completely. For future reference, this section provides a general overview of many causes of and approaches to the problem of reducing stimulus artifacts.

C.6.1 What to look for

Two basic factors give rise to stimulus artifacts like the one in Figure C.1. First, a coupling pathway between the stimulator and recording amplifier is necessary. This might be an obvious pathway such as the tissue under study, or it might be a more subtle pathway involving power supplies or parasitic impedances between the stimulator and amplifier. Or it might be a combination of these. This first factor accounts for the part of the artifact which occurs while the stimulus is active. A second factor is required for the artifact to outlast the stimulus: the existence of one or more slowly discharging capacitances. Such capacitors might be present in the stimulator, the amplifier, or at electrode-electrolyte interfaces. Slowly unsaturating op-amps also fit into this category. The capacitors might also be part of a parasitic coupling pathway between the stimulator and amplifier.

C.6.2 What to do

1. **Minimize coupling between the stimulator and amplifier.** This can be achieved by using separate supplies and grounds for the stimulator and amplifier, keeping the amplifier input impedance as large as possible, and keeping the leads for stimulating and recording electrodes as far from one another as possible and shielded if possible. With regard to the shielding, recording electrodes should be surrounded by conductors connected to the recording ground and stimulating electrodes should be surrounded by driven shields at the same potentials.

2. **Use "subtractive" methods** There are several related approaches wherein an estimate of the artifact signal is subtracted from the response signal prior to amplification. For example, if a reasonable prediction of the stimulating field distribution can be made and/or if the experimenter has flexibility in placing recording electrodes, artifacts can sometimes be eliminated by recording differentially and placing the + and - recording electrodes at different points on an isopotential surface (McGill et al., 1982; Ranck, 1981). Another approach utilized a single electrode for stimulation and recording. To estimate the potential due to charge decay on this electrode, a second identical electrode (at a remote location in the bathing medium) was stimulated with an identical stimulus (Hentall, 1991). A third approach would be to use a computer and signal

processing to estimate the artifact, perhaps based on an average or subthreshold measurement. If the artifacts saturate the amplifier under suprathreshold conditions, it will be necessary to re-inject and subtract out a scaled version of the estimate prior to high gain amplification. If amplifiers are not saturated, all manipulations can be done directly on the amplifier output. Critical to all of these methods is to generate an estimate which is reliable and free of response components.

3. **Identify and minimize slowly discharging capacitors.** These may take the form of parasitics between stimulating and recording electrodes or be present in high-pass filters, at op-amp inputs, or at electrode-electrolyte interfaces. The parasitics can sometimes be reduced by keeping stimulating and recording leads far apart and by shielding, as described above. Op-amp input capacitances and electrode interface capacitances can sometimes be reduced through the technique of negative capacitance compensation (Crapper and Noell, 1963; Greenberg, 1998a).

4. **Prevent capacitors from acquiring charge in the first place.** Electronic switches can sometimes be used to prevent capacitors from acquiring charge during stimulation. For example, high pass filter capacitors can be protected using a sample and hold circuit, as discussed in Section C.2.2.

5. **Actively discharge capacitors.** In principle, if slowly discharging capacitors can be identified, one should be able to quickly discharge them using electronic switches. In practice, getting such circuits to work may prove challenging, especially if these capacitors reside at the input of a high gain amplifier (see Section C.5.2).

Bibliography

Ames III, A. and Masland, R. H. (1976). Responses to acetylcholine of ganglion cells in an isolated mammalian retina. *Journal of Neurophysiology*, 39(6):1220–1235.

Ames III, A. and Nesbett, F. B. (1981). In vitro retina as an experimental model of the central nervous system. *Journal of Neurochemistry*, 37(4):867–877.

Ames III, A. and Pollen, D. A. (1969). Neurotransmission in central nervous tissue: a study of isolated rabbit retina. *Journal of Neurophysiology*, 32:424–442.

Amthor, F. R., Oyster, C. W., and Takahashi, E. S. (1983). Quantitative morphology of rabbit retinal ganglion cells. *Proc. R. Soc. Lond. B*, 217:341–355.

Berson, E. L. (1993). Retinitis pigmentosa. *Investigative Ophthalmology and Visual Science*, 34(5):1659–1676.

Brindley, G. S. (1955). The site of electrical excitation of the human eye. *Journal of Physiology*, 127:189–200.

Caldwell, J. H. and Daw, N. W. (1978). New properties of rabbit retinal ganglion cells. *Journal of Physiology*, 276:257–276.

Chow, A. Y. and Chow, V. Y. (1997). Subretinal electrical stimulation of the rabbit retina. *Neuroscience Letters*, 225:13–16.

Crapper, D. R. and Noell, W. K. (1963). Retinal excitation and inhibition from direct electrical stimulation. *Journal of Neurophysiology*, 26:924–946.

Dawson, W. W. and Radtke, N. D. (1977). The electrical stimulation of the retina by indwelling electrodes. *Investigative Ophthalmology and Visual Science*, 16(3):249–252.

Doty, R. W. and Grimm, F. R. (1962). Cortical responses to local electrical stimulation of retina. *Experimental Neurology*, 5:319–334.

Eckmiller, R. (1997). Learning retina implants with epiretinal contacts. *Ophthalmic Research*, 29(5):281–9.

Freeman, J. A. (1971). An electronic stimulus artifact suppressor. *Electroencephalography and Clinical Neurophysiology*, 31:170–172.

Gernandt, B. and Granit, R. (1947). Single fibre analysis of inhibition and the polarity of the retinal elements. *Journal of Neurophysiology*, 10:295–302.

Granit, R. (1946). The distribution of excitation and inhibition in single-fibre responses from a polarized cat retina. *Journal of Physiology*, 105:45–53.

Granit, R. (1948). Neural organization of the retinal elements, as revealed by polarization. *Journal of Neurophysiology*, 11:239–251.

Greenberg, R. J. (1998a). *Analysis of Electrical Stimulation of the Vertebrate Retina – Work Towards a Retinal Prosthesis*. PhD thesis, Johns Hopkins University. Chapter 3: The target of trans-retinal electrical stimulation in frog retina—a quantitative analysis of ganglion cell response latencies.

Greenberg, R. J. (1998b). *Analysis of Electrical Stimulation of the Vertebrate Retina – Work Towards a Retinal Prosthesis*. PhD thesis, Johns Hopkins University. Chapter 4: Stimulation pulse width determines retinal element excited by electrical stimulation.

Greenberg, R. J. (1998c). *Analysis of Electrical Stimulation of the Vertebrate Retina – Work Towards a Retinal Prosthesis*. PhD thesis, Johns Hopkins University. Chapter 5: Electrode geometry design for a retinal prosthesis.

Greenberg, R. J., Velte, T. J., Humayun, M. S., Scarlatis, G. N., and Eugene de Juan, J. (1999). A computational model of electrical stimulation of the retinal ganglion cell. *IEEE Transactions on Biomedical Engineering*, 46(5):505–514.

Grumet, A. E. (1994). Extracellular electrical stimulation of retinal ganglion cells. Master's thesis, Massachusetts Institute of Technology.

Grumet, A. E., Wyatt, J. L., and Rizzo, J. F. (1998). Multi-electrode recording and stimulation of the salamander retina in vitro. *Investigative Ophthalmology and Visual Science*, 39(4):S565. (Abstract).

Hambrecht, F. T. (1990). The history of neural stimulation and its relevance to future neural prostheses. In Agnew, W. F. and McCreery, D. B., editors, *Neural Prostheses: Fundamental Studies*. Prentice Hall.

Hentall, I. D. (1991). Coincident recording and stimulation of single and multiple neuronal activity with one extracellular microelectrode. *Journal of Neuroscience Methods*, 40:181–191.

Horowitz, P. and Hill, W. (1989). *The Art of Electronics, 2nd Ed.* Cambridge University Press.

Howarth, C. I. (1954). Strength duration curves for electrical stimulation of the human eye. *The Quarterly Journal of Experimental Psychology*, 6:47–61.

Humayun, M. S., Eugene de Juan, J., Dagnelie, G., Greenberg, R. J., Propst, R. H., and Phillips, D. H. (1996). Visual perception elicited by electrical stimulation of retina in blind humans. *Archives of Ophthalmology*, 114:40–46.

Humayun, M. S., Eugene de Juan, J., Weiland, J. D., Dagnelie, G., Katona, S., Greenberg, R. J., and Suzuki, S. (1999). Pattern electrical stimulation of the human retina. *Vision Research*, 39:2569–2576.

Humayun, M. S., Propst, R., Eugene de Juan, J., McCormick, K., and Hickingbotham, D. (1994). Bipolar surface electrical stimulation of the vertebrate retina. *Archives of Ophthalmology*, 112:110–116.

Jensen, R. J., Rizzo, J. F., Grumet, A. E., Edell, D. J., and Wyatt, J. L. (1996). Single unit recording following extracellular electrical stimulation of rabbit retinal ganglion bodies. Technical Report 600, MIT Research Laboratory of Electronics.

Knighton, R. W. (1975). An electrically evoked slow potential of the frog's retina. I. properties of response. *Journal of Neurophysiology*, 38:185–197.

Kovacs, G. T. A. (1994). Introduction to the theory, design, and modeling of thin-flim microelectrodes for neural interfaces. In Stenger, D. A. and McKenna, T. N., editors, *Enabling Technologies for Cultured Neural Networks*. Academic Press.

Kuffler, S. W. (1953). Discharge patterns and functional organization of mammalian retina. *Journal of Neurophysiology*, 16:37–68.

Kuras, A. and Gutmanienė, N. (1997). Multi-channel metallic electrode for threshold stimulation of frog's retina. *Journal of Neuroscience Methods*, 75:99–102.

Loizou, P. C. (1999). Introduction to cochlear implants. *IEEE Engineering in Medicine and Biology Magazine*, 18(1):32–42.

McGill, K. C., Cummins, K. L., Dorfman, L. J., Berlizot, B. B., Luetkemeyer, K., Nishimura, D. G., and Widrow, B. (1982). On the nature and elimination of stimulus artifact in nerve signals evoked and recorded using surface electrodes. *IEEE Transactions on Biomedical Engineering*, 29(2):129–137.

McNeal, D. R. (1976). Analysis of a model for excitation of myelinated nerve. *IEEE Transactions on Biomedical Engineering*, BME-23:329–337.

Meister, M., Pine, J., and Baylor, D. A. (1994). Multi-neuronal signals from the retina: acquisition and analysis. *Journal of Neuroscience Methods*, 51:95–106.

Minzly, J., Mizrahi, J., Hakim, N., and Liberson, A. (1993). Stimulus artefact suppressor for EMG recording during FES by a constant-current stimulator. *Medical and Biological Engineering and Computing*, 31:72–75.

Mittman, S., Taylor, W. R., and Copenhagen, D. R. (1990). Concomitant activation of two types of glutamate receptor mediates excitation of salamander retinal ganglion cells. *Journal of Physiology*, 428:175–197.

Miyachi, E., Takahashi, K., and Murakami, M. (1984). Electrically evoked calcium responses in rods of the frog retina. *Japanese Journal of Physiology*, 34:307–318.

Molotchnikoff, S. (1976). Transient responses of rabbit retinal ganglion cells to photic and electrical stimuli. *The Canadian Journal of Neurological Sciences*, 3(1):73–79.

Molotchnikoff, S. and Lachapelle, P. (1978). Lateral geniculate cell responses to electrical stimulation of the retina. *Brain Research*, 152:81–95.

Morrison, R. (1986). *Grounding and Shielding Techniques in Instrumentation, 3rd Ed.* John Wiley & Sons, Inc.

Murakami, M., Shimoda, Y., Nakatani, K., Miyachi, E., and Watanabe, S. (1982). Gaba-mediated negative feedback from horizontal cells to cones in carp retina. *Japanese Journal of Physiology*, 32:911–926.

Normann, R. A., Maynard, E. M., Rousche, P. J., and Warren, D. J. (1999). A neural interface for a cortical vision prosthesis. *Vision Research*, 39(15):2577–2587.

Ogden, T. E. and Brown, K. T. (1964). Intraretinal responses of the cynamolgus monkey to electrical stimulation of the optic nerve and retina. *Journal of Neurophysiology*, 27:682–705.

Ogden, T. E. and Ito, H. (1971). Avian retina. II. an evaluation of retinal electrical anisotropy. *Journal of Neurophysiology*, 34:367–373.

Peichl, L., Buhl, E. H., and Boycott, B. B. (1987). Alpha ganglion cells in the rabbit retina. *Journal of Comparative Neurology*, 263:25–41.

Pickard, R. S. (1979). A review of printed circuit microelectrodes and their production. *Journal of Neuroscience Methods*, 1:301–318.

Plonsey, R. (1969). *Bioelectric Phenomena*. McGraw Hill, Inc.

Plonsey, R. and Altman, K. W. (1988). Electrical stimulation of excitable cells – a model approach. *Proceedings of the IEEE*, 76(9):1122–1128.

Potts, A. M. and Inoue, J. (1970). The electrically evoked response of the visual system (eer). III. further contribution to the origin of the eer. *Investigative Ophthalmology and Visual Science*, 9(10):814–819.

Pozo, F. D. and Delgado, J. M. R. (1978). Hybrid stimulator for chronic experiments. *IEEE Transactions on Biomedical Engineering*, 25(1):92–94.

Ranck, Jr., J. B. (1975). Which elements are excited in electrical stimulation of mammalian central nervous system: a review. *Brain Research*, 98:417–440.

Ranck, Jr., J. B. (1981). Extracellular stimulation. In Patterson, M. M. and Kesner, R. P., editors, *Electrical Stimulation Research Techniques*. Academic Press.

Ranjan, R. and Thakor, N. V. (1995). Electrical stimulation of cardiac myocytes. *Annals of Biomedical Engineering*, 23:812–821.

Rattay, F. (1986). Analysis of models for external stimulation of axons. *IEEE Transactions on Biomedical Engineering*, BME-33(10):974–977.

Regehr, W. G., Pine, J., Cohan, C. S., Mischke, M. D., and Tank, D. W. (1989). Sealing cultured invertebrate neurons to embedded dish electrodes facilitates long-term stimulation and recording. *Journal of Neuroscience Methods*, 30:91–106.

Rizzo, J. F., Grumet, A. E., Edell, D. J., Wyatt, J. L., and Jensen, R. J. (1997). Single-unit recordings following extracellular stimulation of retinal ganglion cell axons in rabbits. *Investigative Ophthalmology and Visual Science*, 38(4):S40. (Abstract) Poster may be viewed online at `http://rleweb.mit.edu/retina/poster9.html`.

Rizzo, J. F. and Wyatt, J. L. (1997). Prospects for a visual prosthesis. *The Neuroscientist*, 3(4):251–262.

Robblee, L. S. and Rose, T. L. (1990). Electrochemical guidelines for selection of protocols and electrode materials for neural stimulation. In Agnew, W. F. and McCreery, D. B., editors, *Neural Prostheses: Fundamental Studies*. Prentice Hall.

Roby, R. J. and Lettich, E. (1975). A simplified circuit for stimulus artifact suppression. *Electroencephalography and Clinical Neurophysiology*, 39:85–87.

Rodieck, R. W. (1973). *The vertebrate retina: principles of structure and function*. W.H. Freeman and Company.

Rubinstein, J. T. and Spelman, F. A. (1988). Analytical theory for extracellular electrical stimulation of nerve with focal electrodes. I. passive unmyelinated axon. *Biophysical Journal*, 54:975–981.

Rushton, W. A. H. (1927). The effect upon the threshold for nervous excitation of the length of nerve exposed, and the angle between current and nerve. *Journal of Physiology*, 63:357–377.

Santos, A., Humayun, M. S., Eugene de Juan, J., Greenberg, R. J., Marsh, M. J., Klock, I. B., and Milam, A. H. (1997). Preservation of the inner retina in retinitis pigmentosa. *Archives of Ophthalmology*, 115:511–515.

Sherman-Gold, R., editor (1993). *The Axon Guide for Electrophysiology and Biophysics Laboratory Techniques*. Axon Instruments, Inc.

Stanford, L. R. (1987). Conduction velocity variations minimize conduction time differences among retinal ganglion cell axons. *Science*, 238:358–360.

Stone, J. L., Barlow, W. E., Humayun, M. S., Eugene de Juan, J., and Milam, A. H. (1992). Morphometric analysis of macular photoreceptors and ganglion cells in retinas with retinitis pigmentosa. *Archives of Ophthalmology*, 110:1634–1639.

Tehovnik, E. J. (1996). Electrical stimulation of neural tissue to evoke behavioral responses. *Journal of Neuroscience Methods*, 65:1–17.

Toyoda, J. and Fujimoto, M. (1984). Application of transretinal current stimulation for the study of bipolar-amacrine transmission. *Journal of General Physiology*, 84:915–925.

Trifonov, Y. A. and Byzov, A. L. (1977). The interaction in photoreceptor synapses revealed in experiments with polarization of horizontal cells. In Barlow, H. and Fatt, P., editors, *Vertebrate Photoreception*. Academic Press.

Tung, L., Sliz, N., and Mulligan, M. R. (1991). Influence of electrical axis of stimulation on excitation of cardiac muscle cells. *Circulation Research*, 69(3):722–730.

Vaney, D. I. (1980). A quantitative comparison between the ganglion cell populations and axonal outflows of the visual streak and periphery of the rabbit retina. *Journal of Comparative Neurology*, 189:215–233.

Velte, T. J. and Masland, R. H. (1999). Action potentials in the dendrites of retinal ganglion cells. *Journal of Neurophysiology*, 81:1412–1417.

Warman, E. N., Grill, W. M., and Durand, D. (1992). Modeling the effects of electric fields on nerve fibers: determination of excitation thresholds. *IEEE Transactions on Biomedical Engineering*, 39(12):1244–1254.

Weiss, T. F. (1996). *Cellular Biophysics, Volume 2: Electrical Properties*. The MIT Press.

Woodbury, J. W. (1960). Potentials in a volume conductor. In Ruch, T. and Fulton, J., editors, *Medical physiology and biophysics, 18th ed.* WB Saunders Company.

Wyatt, J. L. and Rizzo, J. F. (1996). Ocular implants for the blind. *IEEE Spectrum*, 33:47–53.

Zrenner, E., Stett, A., Weiss, S., Aramant, R. B., Guenther, E., Kohler, K., Miliczek, K. D., Zeiler, M., and Haemmerle, H. (1999). Can subretinal microphotodiodes successfully replace degenerated photoreceptors? *Vision Research*, 39(15):2555–2567.